The Mechanics of and Robotic Design for Quadrupedal Galloping

DISSERTATION

Presented in Partial Fulfillment of the Requirements for

the Degree Doctor of Philosophy in the

Graduate School of The Ohio State University

By

James Patrick Schmiedeler, B.S., M.S.

* * * * *

The Ohio State University

2001

Dissertation Committee:

Kenneth J. Waldron, Adviser

David E. Orin

Gary L. Kinzel

Approved by

_____

Adviser

Department of Mechanical Engineering

ABSTRACT

To make galloping available as a high-speed gait of quadrupedal robots, this dissertation addresses the mechanics of galloping and the design of legged robots for rapid locomotion. A simple method of measuring an animal's geometric and inertial properties is used to develop reasonable model parameters for the animal. An impulsive model of galloping is extended to all dynamic quadrupedal gaits to show that with equal stride frequencies, galloping requires smaller vertical oscillations of the mass center than trotting does at high speeds. In contrast, spring-mass models of both gaits indicate that trotting is accomplished with smaller vertical oscillations and/or lower stride frequencies at lower speeds. In conjunction, these two results suggest that animals transition from a trot to a gallop in order to minimize their stride frequencies without experiencing large vertical displacements.

For a quadruped robot to gallop in an energy-efficient manner, it must be designed to exhibit this same behavior at high speeds. The generalized inertia ellipsoid is presented as visualization tool for comparing leg designs in terms of impact losses and energy required for leg return. Kinetostatic analysis of effective stiffness is introduced as a means of establishing leg geometry in order to match the leg stiffness of animals. This method is implemented in the design of an articulated, prototype leg which stores elastic energy in mechanical extension springs during its return phase and releases that energy as thrust during stance. Experimental results with this leg indicate that it has the performance capabilities to be used in a quadruped galloping machine.

The Mechanics of and Robotic Design for Quadrupedal Galloping

By

James Patrick Schmiedeler, Ph.D.

The Ohio State University, 2001

Kenneth J. Waldron, Adviser

To make galloping available as a high-speed gait of quadrupedal robots, this dissertation addresses the mechanics of galloping and the design of legged robots for rapid locomotion. A simple method of measuring an animal's geometric and inertial properties is used to develop reasonable model parameters for the animal. An impulsive model of galloping is extended to all dynamic quadrupedal gaits to show that with equal stride frequencies, galloping requires smaller vertical oscillations of the mass center than trotting does at high speeds. In contrast, spring-mass models of both gaits indicate that trotting is accomplished with smaller vertical oscillations and/or lower stride frequencies at lower speeds. In conjunction, these two results suggest that animals transition from a trot to a gallop in order to minimize their stride frequencies without experiencing large vertical displacements.

For a quadruped robot to gallop in an energy-efficient manner, it must be designed to exhibit this same behavior at high speeds. The generalized inertia ellipsoid is presented

as visualization tool for comparing leg designs in terms of impact losses and energy required for leg return. Kinetostatic analysis of effective stiffness is introduced as a means of establishing leg geometry in order to match the leg stiffness of animals. This method is implemented in the design of an articulated, prototype leg which stores elastic energy in mechanical extension springs during its return phase and releases that energy as thrust during stance. Experimental results with this leg indicate that it has the performance capabilities to be used in a quadruped galloping machine.

To the first engineer I ever met

ACKNOWLEDGMENTS

The completion of this work was possible only through the efforts of many people to whom I offer my sincerest gratitude. First and foremost, I would like to thank my advisor, Professor Ken Waldron, for his guidance and support throughout my graduate work. His insights in so many areas have been invaluable to me. Secondly, I would like to thank Professor David Orin for serving as a de facto second advisor to me. His perspective on the problems addressed within this work helped established the direction of the project. Additionally, I would like to thank Professors Gary Kinzel and Robert Wing for their helpful discussions with me as members of my dissertation committee. I am particularly grateful to Professor Kinzel for his ceaseless help to me in all aspects of my graduate career. I would also like to thank Professor Necip Berme for his suggestions as a member of my candidacy exam committee.

Duane Marhefka and Luther Palmer are the two electrical engineering graduate students with whom I have worked most closely. I am greatly indebted to Duane for his simulation work with all of the preliminary leg designs and for his helpful suggestions for design improvements. I am similarly indebted to Luther for his work on the control system for the prototype leg, without which there would be no experimental results. Darren Krasny has also helped me through our discussions of quadrupedal locomotion. I am extremely grateful to Chris Hubert for being a good friend throughout my graduate work, for his help in the design of the leg, for the use of his dog Molly, and for his speed and patience in

answering my questions on a wide variety of topics. I would also like to thank Rob Siston for working with me on modeling Molly's locomotion.

For the construction of the prototype leg, I am deeply indebted to Gary Gardner and Keith Rogers. Both patiently answered my many questions at the design phase and offered excellent suggestions for improvements. Gary then worked with my sometimes problematic drawings to masterfully make the parts. His craftsmanship clearly led to the success of the experiments. Both of these men also provided support and advice once assembly was complete and experiments were underway. I would also like to thank Alan Bonifas for his design advice and gracious tool sharing. Professor Blaine Lilly and Vince Vohnout have been of great help to me throughout this work through my various discussions with them. I am particularly grateful to Professor Lilly for his advice on many issues. Further thanks are due to Fred Griesemer, Bruce Isler, Jerry Kingzett, and Joe West for their assistance in the early experiments with the leg.

The following people listed alphabetically have also helped me in one way or another. I apologize to those whom I have undoubtedly left out: Lisa Abrams, Brent Albertson, Brian Boyer, Brad Glenn, Dr. Ambarish Goswami, Professor Bernie Hamrock, Dr. Becky Hoffman, Daria Kotys, Ben Krupp, Pete Mayhan, Paul Mayhan, Professor C. H. Menq, Percy Monteiro, Jim Piper, Francisco Saavedra, Professor S. V. Sreenivasan, Professor Cheena Srinivasan, Sriram Sundararajan, Dr. Devesh Upadhyay, Professor Greg Washington, Eric Wilson, Dr. Jeff Woollard, and Dr. Po-Hua Yang.

I would like to particularly thank my friend and long-time mentor Professor Michael Stanisic for first suggesting that I pursue a graduate degree and encouraging me throughout my work. Additional thanks go out to all of my friends not listed here who have offered

their encouragement. Ultimately, and most importantly, I would like to thank my family for their love and support that have made this work meaningful to me.

I would like to acknowledge the financial support I received from the National Science Foundation through the Graduate Research Fellowship and grant no. IIS-9907121. Financial support was also provided by The Ohio State University through the Presidential Fellowship.

VITA

March 7, 1974	Born - South Bend, IN, USA
May - August 1995	Engineering Intern, AlliedSignal Corporation, South Bend, IN
May 1996	B.S. Mechanical Engineering, University of Notre Dame, Notre Dame, IN
May - August 1996	Engineering Intern, AlliedSignal Corporation, South Bend, IN
September 1996 - August 1997	University Fellow, The Ohio State University
September 1997 - August 2000	National Science Foundation Graduate Research Fellow, The Ohio State University
March 1998	M.S. Mechanical Engineering, The Ohio State University
September 1998 - June 1999	Graduate Teaching Assistant, The Ohio State University
September 2000 - August 2001	Presidential Fellow, The Ohio State University
September - December 2001	Graduate Research Assistant, The Ohio State University

PUBLICATIONS

"A study of quadruped gallops," In *NSF Design, Service and Manufacturing Grantees and Research Conference*, Tampa, FL, 2001 (with D. W. Marhefka, D. E. Orin, and K. J. Waldron).

"Impact analysis as a design tool for the legs of mobile robots", In J. Lenarcic and M. M. Stanisic, editors, *Advances in Robot Kinematics*, pp. 129-136, 2000, Kluwer Academic Publishers (with K. J. Waldron).

"Mechanical design of a quadrupedal galloping machine", In *Proceedings of the Tenth World Congress on the Theory of Machines and Mechanisms*, Oulu, pp. 1985-1990, 1999 (with K. J. Waldron).

"Design of compliant articulated limbs for a quadrupedal galloping machine", In *Proceedings of the Sixth Applied Mechanisms and Robotics Conference*, Cincinnati, OH, pp. 006:1-8, 1999 (with K. J. Waldron, D. W. Marhefka, and D. E. Orin).

"The mechanics of quadrupedal galloping and the future of legged vehicles", *International Journal of Robotics Research*, vol. 18, pp. 1224-1234, 1999 (with K. J. Waldron).

"Design of galloping machines", In *Proceedings of the Twelfth CISM-IFToMM Symposium on Theory and Practice of Robots and Manipulators*, Paris, pp. 353-360, 1998 (with K. J. Waldron).

"The Effect of Drag on Footfall Phasing in Quadruped Galloping", Master's Thesis, The Ohio State University, 1998.

"A more flexible robotic wrist", *Mechanical Engineering Magazine*, vol. 119, no. 7, pp. 78-80, 1997 (with J. M. Wiitala and B. J. Rister).

"Design of a new singularity-free robotic wrist", ASME 96-WA/DE-2, *International Mechanical Engineering Congress & Exhibition, The Winter Annual Meeting of the ASME*, 1996 (with J. M. Wiitala and B. J. Rister).

FIELDS OF STUDY

Major Field: Mechanical Engineering

Studies in:

Robotics	Professors K. J. Waldron and D. E. Orin
Design	Professors K. J. Waldron, B. W. Lilly, Jr. and S. C. Lee
Dynamic Systems	Professors R. Singh, K. Srinivasan E. O. Doeblin, and A. Keyhani
Mathematics	Professors U. H. Gerlach and M. R. Foster

TABLE OF CONTENTS

Page

LIST OF TABLES

Table **Page**

LIST OF FIGURES

CHAPTER 1

INTRODUCTION

1.1 Motivation

The investigation of legged locomotion in the biological world pursues a comprehensive understanding of animal movements and body structures. It provides insight into how animals move, how those motions are controlled neurologically, and what factors predispose an animal to a certain type of locomotion under different environmental circumstances. It also leads to an appreciation for the wide range of legged solutions to the locomotion problem. Various animals employ from as few as two legs, like humans, to as many as several hundred, like the millipede, to travel from one location to another.

An understanding of biological legged locomotion can also aid in the design and control of legged machines. To date, biological systems certainly outperform mechanical systems in all areas of legged locomotion. While mechanical systems are constructed with very different materials and likely have very different objectives than do animals, it is still reasonable to look to the biological world for design inspiration, at least as a starting point [40]. Howell [66] warned about the limitations of this approach, suggesting that evolution represents a series of compromises resulting not in an optimal solution, but in a satisfactory one. Nonetheless, understanding legged locomotion in the biological world is an important step toward developing more advanced legged machines.

The construction of legged vehicles is of interest because they have the potential to traverse rough terrain with greater speed, efficiency, and mobility than can conventional wheeled and tracked vehicles. With its discrete footfalls, a legged machine requires only a few secure footholds in contrast to the continuous paths required by wheeled and tracked vehicles. By prudently selecting its footholds, a legged vehicle should be able to avoid small obstacles without significant change in path direction or speed. More dramatically, periods of ballistic flight can accomplish the same task when facing larger obstacles. Lateral manuevering to avoid obstacles of any size can greatly reduce the average forward speed of wheeled and tracked vehicles.

From a different perspective, the small, discrete footholds of a legged machine will likely have a less significant impact on the environment than the continuous paths formed by wheeled and tracked machines. This means that the environment will also exert less drag on the legged machine. The legs can be raised out of soft soil in a direction normal to the terrain to minimize the energy losses associated with plowing of the soil, thereby improving efficiency. The legs can also function as an active suspension system to provide a smoother ride over uneven terrain than would be experienced in a wheeled or tracked vehicle.

A number of engineering applications could benefit from the advantages legged machines offer in traversing rough terrain. Industrial uses include forestry [121] and hazardous waste inspection and disposal, while research applications include the exploration of inaccessible or dangerous locations such as volcanos [15] and the surfaces of other planets [120]. Surveillance, reconnaissance, and land mine detection and removal [64] are just a few examples of the many military uses for legged machines.

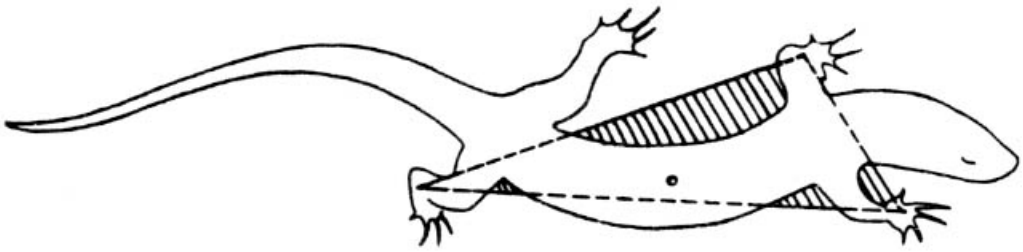

Figure 1.1: Support triangle of a lizard, from Gambaryan [46].

Quadrupedal machines are of unique interest for a number of reasons. First, quadrupeds are a natural choice for basic walking machines because four legs is the minimum number required to maintain static stability if the area of foot contact is neglected. In Figure 1.1, the three feet contacting the ground form a support triangle. If the speed is relatively slow, the lizard is statically stable provided the projection of its mass center falls within the triangle. Secondly, quadrupedal structure appears to have great flexibility in the biological world. In terms of size, existing quadrupeds range from tiny mice to massive elephants, while no genuinely large animals have more than four legs. In terms of limb configuration, quadruped leg postures range from sprawling to upright. The lizard in Figure 1.1 has sprawling leg posture characterized by lateral foot placement, whereas the elephant in Figure 1.2 has upright leg posture characterized by foot placement underneath the body.

In the biological world, various quadrupeds also display the greatest aptitude for different aspects of locomotion. The cheetah is the fastest land animal, and the ass is thought to be capable of the greatest endurance running [46]. Manueverability, defined as the capacity for rapid and controlled change of speed and direction [60], is epitomized by antelope evading their significantly faster predator, the cheetah. Mountain goats display tremendous jumping ability in leaping from one small ledge to another [46]. If biological quadrupeds

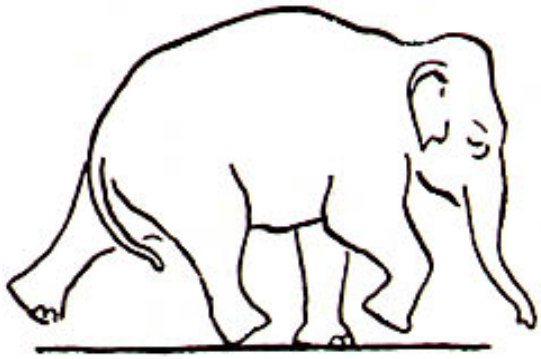

Figure 1.2: Running elephant, from Gambaryan [46].

can achieve these levels of performance, mechanical quadrupeds may excel in speed, endurance, manueverability, and jumping as well.

Focusing on speed, galloping is the fastest means of legged locomotion in the biological world. Mid-sized, four-legged mammals almost universally use the gallop when running at high speeds. This is true of both sprinters like the cheetah and endurance runners like the ass. Hoyt and Taylor [67] determined that the gallop requires less energy than the trot for horses traveling at high speeds, and this result would seem to apply equally well to most other quadrupeds that gallop. As such, galloping is the most logical gait for energy-efficient, high-speed locomotion of quadrupedal machines.

1.2 Description of Quadrupedal Gaits

A gait is a regularly repeated sequence and manner of moving the legs [60]. If the footfalls of the two feet of a leg-pair are evenly spaced in time, the gait is said to be symmetrical [57]. The trot and pace are both symmetrical gaits. If the footfalls of a leg-pair are unevenly spaced in time, the gait is asymmetrical [59]. Asymmetrical gaits include the bound, half-bound, crutch-walk, pronk, and gallop. Gambaryan [46] and Sukhanov [122]

characterized the canter as a symmetrical gait, but the convention of Howell [66] and Hildebrand [57] is more accurate in considering it an asymmetrical gait.

It is convenient to divide gaits into the categories of walking and running. Any gait in which each foot is on the ground for at least half the stride cycle is a walking gait. In running gaits, each leg is on the ground less than half the stride cycle, so periods of flight can be present [60]. It is possible in an asymmetrical gait that only some of the feet would be on the ground for at least half the stride cycle, while the others would be on the ground for less than half the stride cycle. Such an unconventional gait with the characteristics of both walking and running would involve the dominant use of some of the legs.

Alternative distinctions between walking and running may apply for locomotion in tight circles, in enhanced gravity, or on very compliant surfaces [84]. The general definitions, though, are adequate for the present work since the primary interest is rapid, straight-line motion over hard ground. The sequence of leg movements can be the same in walking and running gaits, and both symmetrical and asymmetrical gaits are found in each category. Walking gaits, however, are most commonly symmetrical. Since dynamic locomotion is the focus of this work, only quadrupedal running gaits are described in detail in the following sections.

1.2.1 Trot

The trot is the most common intermediate speed gait of biological quadrupeds. When animals transition from walking to running to increase speed, trotting is typically the first gait they employ. The legs operate in diagonal pairs, as shown for a horse in Figure 1.3. The trot is generally a very stable dynamic gait because when each pair of legs is on the ground, the line of support between the feet passes diagonally underneath the body. For

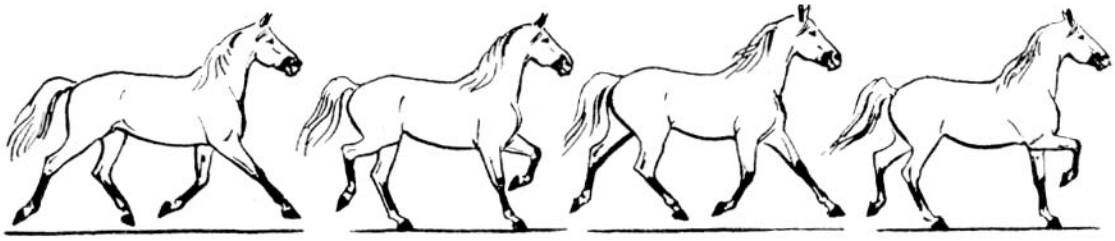

Figure 1.3: Horse in a trot, from Gambaryan [46].

some reptiles and amphibians, the trot is actually the highest speed gait. This may be because these animals simply do not have the neurological capability to control the less stable asymmetrical gaits [122].

1.2.2 Pace

The pace, sometimes called the rack, is also an intermediate speed gait, but it differs from the trot in that the legs operate in lateral rather than diagonal pairs. This is shown again for a horse in Figure 1.4. The pace is less common than the trot probably because it is less stable. Since the legs provide support in pairs on alternating sides of the body, significant roll motion of the trunk is typical with this gait. Pacing does, however, offer an advantage for long-legged animals. With the legs on either side of the body moving in

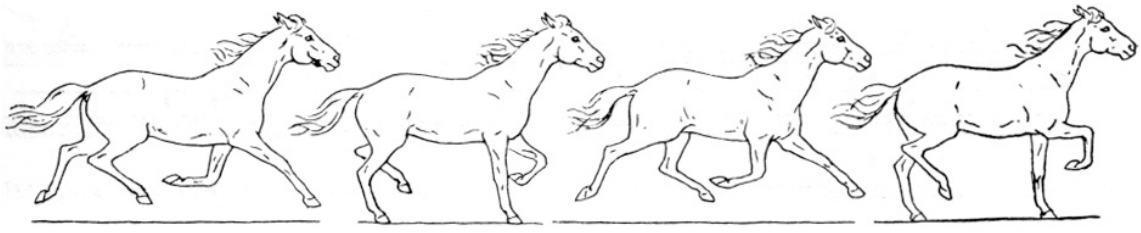

Figure 1.4: Horse in a pace, from Gambaryan [46].

Figure 1.5: Souslik in a bound, from Gambaryan [46].

unison, there is less problem with front-hind leg interference than in trotting. This explains why camels, giraffes, and some long-legged dogs pace rather than trot [29].

1.2.3 Bound

The bound is a gait in which the legs operate in front and hind pairs, as shown for a rodent in Figure 1.5. Bounding is most commonly found in small animals as they move rapidly over terrain that is rough in relation to their body size [60]. It has also been observed in larger animals moving through soft, deep snow [66] or shallow water and climbing hills [30]. These behaviors reflect that the bound constitutes a series of leaps off each pair of legs with the body experiencing significant pitch during the flight phases. The bound is a high-speed gait, but larger animals typically prefer to gallop when moving over relatively flat, hard terrain.

1.2.4 Half-bound

The half-bound is similar to the bound except that the two front legs operate somewhat out of phase. This is the typical high-speed gait of rabbits, like the one shown in Figure 1.6, probably because the mass center is located closer to the hind legs [66]. Most members of

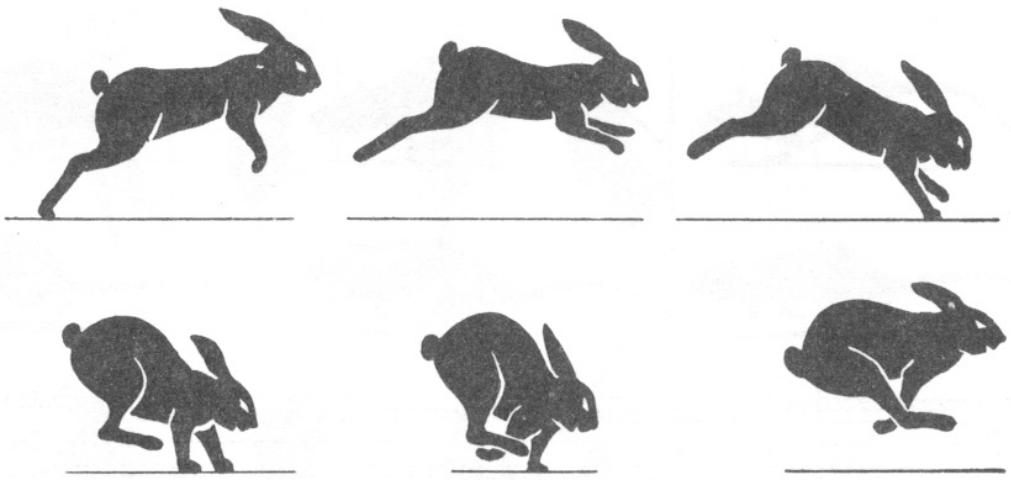

Figure 1.6: Hare in a half-bound, from Gambaryan [46].

the feline family, though, also employ the half-bound at high-speeds [46]. The pitching of the body is very similar to that observed in the bound.

1.2.5 Crutch-walk

The crutch-walk can be considered the opposite gait of the half-bound as the front legs operate together and the hind legs operate out of phase. The crutch-walk is very rarely used by biological quadrupeds. In fact, it is common only in apes using both their arms and legs for locomotion [59].

1.2.6 Pronk

The pronk is a gait in which all four legs operate in phase. Even more so than the bound, the pronk consists of a sequence of large leaps. Unlike the bound, though, the body does not pitch because the legs all thrust together. The pronk is rarely observed in biological quadrupeds, but mule-deer do pronk in climbing hills and some antelope periodically take pronk-like steps during rapid locomotion [66].

1.2.7 Gallop

The gallop is the most common high-speed gait of relatively large biological quadrupeds. It is characterized by the two front footfalls occurring sequentially, followed by the two hind footfalls. In general, no two feet touch down at the same time, and the phase difference between the two front legs is typically larger than that between the two hind legs [58]. After the front feet lift off the ground, the flight phase is referred to as "gathered" because the legs are gathered together under the body. If a flight phase occurs after the hind feet lift off, it is referred to as "extended" because the legs are extended out from the body. The gathered flight phase is almost always present in the gallop and is generally longer than the extended flight phase which appears primarily at high speeds [46]. Both flight phases may also be found in the bound and half-bound.

Transverse Gallop

If the legs on the same side of the body are the first to touch down in both the front and hind leg-pairs, the gait is a transverse gallop. It is also called a diagonal gallop because the second footfall of each pair is followed by the footfall of the diagonal leg. The body undergoes two roll angular velocity oscillations per stride because the footfalls alternate from one side of the body to the other. Figure 1.7 shows a horse in a transverse gallop.

The literature contains some conflicting claims about which animals typically use the transverse gallop. A review of these claims, with particular credence given to the work of Muybridge [90], Howell [66], Gambaryan [46], and Hildebrand [59], indicates that animals falling into the following groups favor the transverse gallop: horse, cattle, buffalo, rhinoceros, camel, and camelid. Sheep and goats display no consistent preference for either the transverse gallop or the rotary gallop.

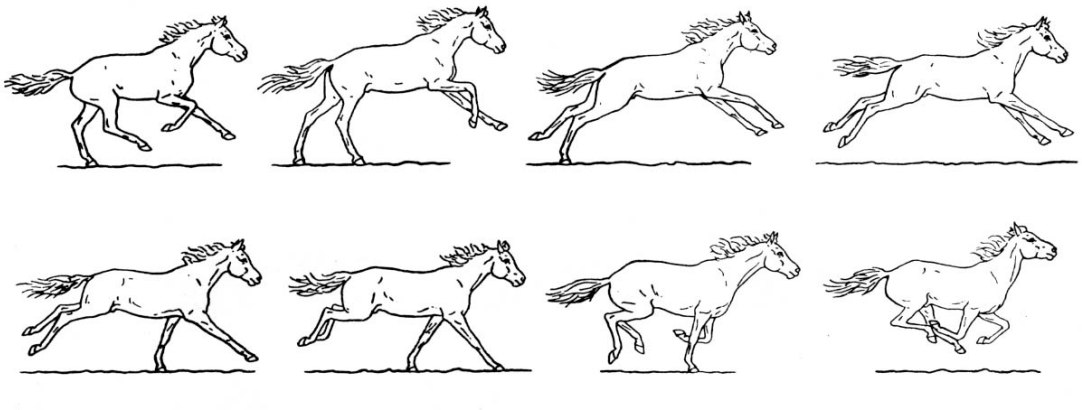

Figure 1.7: Horse in a transverse gallop, from Gambaryan [46].

Rotary Gallop

If the legs on opposite sides of the body are the first to touch down in the front and hind leg-pairs, the gait is a rotary (or rotatory) gallop. It is also called a lateral gallop because the second footfall of each pair is followed by the footfall of the lateral leg. As such, the body undergoes only one roll angular velocity oscillation and one roll angle oscillation per stride because the footfalls rotate around the body. Review of the literature indicates that the animals falling into the following groups favor the rotary gallop: deer, antelope, giraffe, tapir, dog, cat, bear, and carnivores in general. Figure 1.8 shows a cheetah in a rotary gallop.

Muybridge [90], De La Croix [28], and a number of other researchers suggest that the transverse gallop is preferred by more animals than the rotary gallop. They offer little evidence to support this claim, and the lists presented here suggest that the rotary gallop is actually preferred by more animals, as Gambaryan [46] argued. The error might be explained by research familiarity with the locomotion of horses, animals that do favor the transverse gallop.

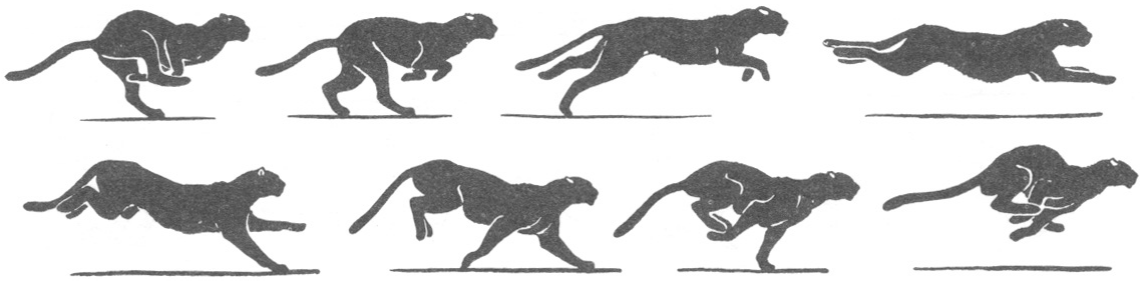

Figure 1.8: Cheetah in a rotary gallop, from Gambaryan [46].

Comparison of Gallops

The literature also contains a number of claims about the relative advantages of the transverse and rotary gallops. Theories from multiple sources suggest that the transverse gallop is better for locomotion over flat terrain, for endurance running at slower speeds such that there is only one flight phase, and for running with little flexion in the back. Conversely, the rotary gallop would be better for locomotion over rough terrain, for sprint galloping with two flight phases, and for running with a flexible back. These theories appear to be based more upon the behavior of specific animals that prefer each gait than upon actual mechanics.

The gait mechanics do indicate, though, that the transverse gallop is probably more stable than the rotary gallop. If there is no extended flight phase, the transverse gallop has a period of diagonal support while the rotary gallop has a period of lateral support. If three feet are on the ground at the same time, the support triangle is larger in the transverse gallop [60]. This would explain why heavy animals like cattle, buffalo, and rhinoceroses prefer the transverse gallop. The tapir is the primary exception to this generalization regarding the stability of heavy animals. It is not clear whether or not maneuverability, normally in

opposition to stability, is inherently better in the rotary gallop. If it is, however, that would explain the preference for the rotary gallop among other animals.

Leg interference is also less likely with the transverse gallop [58]. The sequential footfalls on opposite sides of the body allow for greater clearance between the front and hind legs. The leg phasing of the rotary gallop is somewhat similar to pacing, but because the lateral pairs operate out of phase, interference is more likely. Superior leg clearance would explain why camels and camelids favor the transverse gallop. Giraffes are a long-legged exception, but they abduct/adduct their legs to prevent interference [46].

1.2.8 Canter

The canter is a transitional gait between trotting and galloping that bears some resemblance to both. One diagonal pair of legs operates in phase while the other two legs operate individually. Following the support of the diagonal pair, the individual front foot touches down, and a period of flight may occur after this foot lifts off. The individual hind foot next touches down, and there is normally no flight phase before the next support of the diagonal pair. A horse's slow canter without any flight phases is shown in Figure 1.9.

1.3 Background

The following two sections provide a brief overview of the historical literature pertaining to legged locomotion in both biological and mechanical systems. The overview is relatively general because each subsequent chapter also includes a background section that reviews the significant literature pertaining specifically to the topics addressed within.

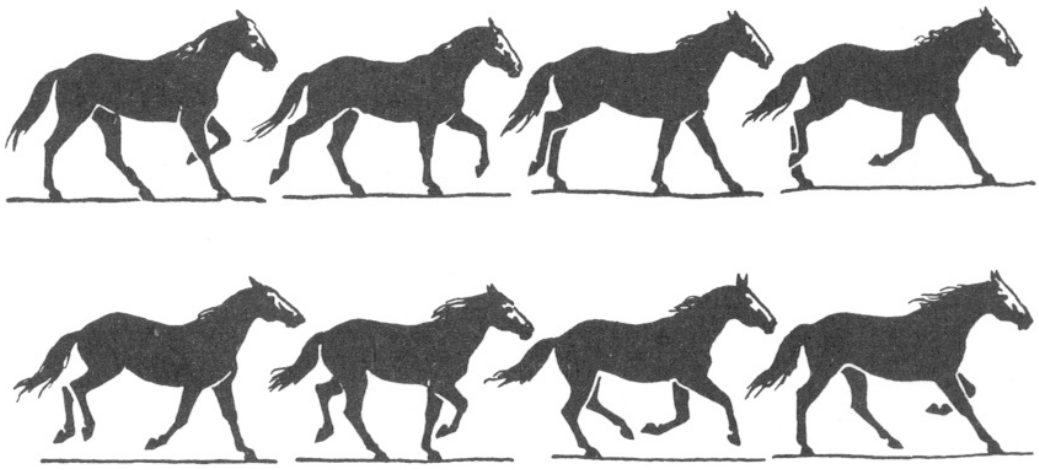

Figure 1.9: Horse in a slow canter, from Gambaryan [46].

1.3.1 Biological Systems

Human beings have been studying the legged locomotion of animals in one way or another since drawing the first pictures of them on cave walls. In 1879, though, Marey [77] was the first to invent an apparatus capable of measuring the sequence of footfalls and the duration of support in animal locomotion. At about the same time, Muybridge [90] developed a technique for taking a series of still photographs in rapid succession to record the movements of a great number of different animals as they moved with various gaits. His collection of photographs is so extensive that it remains in use among researchers today. In the late 1930's, Manter [76] and Elftman [33] introduced force plates for recording the ground reaction forces of walking animals and humans. Barclay [14] later combined the use of force plates with simultaneous photography to calculate the activities of the major muscle groups.

Muybridge [90] provided an early discussion of quadrupedal gaits that was later developed in greater detail. Howell [66] introduced a more in-depth analysis of gaits and

applied it to a wide range of animals. Sukhanov [122] developed a thorough means of characterizing symmetrical gaits and studied the locomotion of lower tetrapods in more detail than any previous work. Hildebrand's [57] work with symmetrical gaits paralleled that of Sukhanov, but he also developed a similar, yet more complex characterization for asymmetrical gaits [59]. Hildebrand's work with quadruped gait selection [58] was also a significant step toward explaining gait transitions. Gray's [49] work with quadrupedal locomotion addressed how body structure affects gait.

Gambaryan [46] wrote probably the most complete text of its time dealing specifically with quadrupedal locomotion. It provides an exhaustive survey of mammalian gaits, discusses some evolutionary theories for gait development, and analyzes some of the mechanics of quadrupedal locomotion. McMahon [83] later combined knowledge of biological and physiological processes with locomotion analysis to develop a more complete view.

The concept of preferred speeds within each gait was first introduced by Pennycuick [97] after observing wildebeast migration. Alexander and his colleagues have extensively investigated legged locomotion, most notably what role is played by elastic mechanisms [4] and how gait transitions can be predicted [10]. Heglund and Taylor's [52] subsequent investigation of preferred speeds and gait transitions in animals across many species successfully related various locomotion parameters to body mass.

1.3.2 Mechanical Systems

The first legged robot to walk autonomously under full computer control was the "Phoney Pony" built by Frank [38] and McGhee [81] in 1966. This quadruped's legs were actuated by electric motors, and it moved with a statically-stable walking gait. A couple of years later, Liston [75] and his colleagues at General Electric built a much larger quadruped

walking truck. This machine was hydraulically powered and carried a human operator to coordinate the control of its statically stable motion. In the early 1980's, Hirose built a series of quadrupeds using a pantograph leg mechanism design. With sensors on the feet, the PV-II machine was able to climb stairs and negotiate obstacles using its own control system [63].

In parallel with this pioneering work to build statically-stable quadrupedal machines, a number of hexapod robots were also constructed. In the late 1970's, the OSU Hexapod was built by McGhee [82] and his colleagues. This electrically-powered machine was capable of walking with several different gaits and negotiating simple obstacles using computer control. At about the same time, Okhotsimski [93] and his colleagues built a similar machine with nearly equivalent capabilities that used a hybrid computer for control. In 1983, Sutherland [123] built the first self-contained walking machine with an on-board microcomputer for control. This hexapod could carry an operator and was hydraulically actuated. At about the same time, Odetics Inc. built the ODEX I, a self-contained, battery-powered hexapod with advanced motion capabilities and a large lifting capacity [108].

None of these statically-stable machines, though, was capable of true terrain adaptability. The Adaptive Suspension Vehicle [118], constructed at The Ohio State University in the mid-1980's, was a self-contained, hexapod walking machine and the first legged robot to be fully terrain-adaptive. The hydraulically actuated ASV was capable of carrying a human operator, and at higher speeds, its motion was quasi-statically stable. A number of other four- and six-legged machines operating primarily with static stability have been constructed since this landmark work. In addition, legged machines capable of dynamic locomotion, the focus of the present work, have also been built.

Matsuoka [80] built the first legged robot to move with dynamic stability. His electrically actuated monopod hopped in place and moved slowly forward in reduced gravity with its motion confined to an inclined table. Raibert's research group extended this idea with their hydraulically actuated monopods that hopped in standard gravity in two and three dimensions [103]. Their one-leg control algorithms were later applied to a planar biped of similar design which ran at much higher speeds than did the monopods. Prior to Raibert's biped, Kato and his colleagues [70] built a hydraulically actuated biped that walked with a quasi-dynamic gait. At about the same time, Miura and Shimoyama's [89] stilt-like biped became the first to actively balance itself.

As for the biped, Raibert's group extended their one-leg algorithms to achieve the first ever dynamic locomotion with a quadruped robot [106]. Exploiting the symmetry in quadrupedal locomotion [104], this hydraulically actuated machine was able to trot, pace and bound [102]. Subsequent work has produced only four other quadruped machines capable of full dynamic motion with flight phases. Lilly [74] proved that high-level control is not required for symmetrical, dynamic locomotion with his quadruped trotting machine that used a series of cams for passive coordination. Furusho and his colleagues [45] achieved a bounding gait with their Scamper2 quadruped, as did Kimura's group [73] with their planar Patrush robot. Both of these machines were electrically actuated. Buehler's group [95] introduced a significant advancement with their battery powered Scout II, the first self-contained quadruped capable of dynamic locomotion. Like the other machines, it ran with a bounding gait. No machine capable of true galloping has yet been built.

The uniqueness of Scout II emphasizes that power consumption continues to be an important problem in developing legged machines for dynamic locomotion. With the one exception, no quadruped has carried an on-board power source while running. The fact

	Mass (kg)	**Robot Maximum Bounding Speed** (m/s)	**Animal Minimum Galloping Speed** (m/s)
Raibert quadruped	30.8	2.9	3.2
Scout II	30.0	1.2	3.2
Scamper2	20.0	< 1.0	2.9
Patrush	4.8	< 1.0	2.1

Table 1.1: Maximum bounding speeds of four quadruped robots and the predicted trot-to-gallop transition speeds of animals having the same mass as each robot.

that these quadrupeds have employed bounding gaits at relatively low speeds where the very gait itself is inefficient may be one factor contributing to the difficulty. Table 1.1 lists the maximum speed of each of the four bounding robots and the predicted minimum galloping speed of an animal having the same mass. The bound is a gait similar to the gallop, and Heglund and Taylor [52] have shown that few animals of the corresponding mass gallop at speeds lower than the predicted values in the table.

Raibert's quadruped is the only one of the four listed in Table 1.1 that bounded at a speed close to the minimum galloping speed of an animal having the same mass. While quadruped robots and animals of the same size will have vastly different designs and goals, qualitative similarity in their dynamic locomotion may correspond to qualitative similarity in their energy efficiency. If so, previous quadrupeds have attempted to use the bound at speeds generally below those at which it becomes an energy-efficient gait.

1.4 Objectives

Based on the evaluation of biological data and previous mechanical quadrupeds, this work theorizes that for a quadruped robot to travel at high speeds in an energy efficient

manner, it must be capable of galloping. Conversely, galloping is not a useful gait for a slow moving quadruped robot because it is inefficient at lower speeds. In order to make the gallop available as a high-speed gait in mechanical systems, two questions are to be answered. Why is galloping energetically advantageous at high speeds, and how does one design a quadruped robot in order to capture those advantages?

1.5 Organization

Chapter 2 reviews a simple, non-invasive method of determining with reasonable accuracy the geometric and inertial properties of a quadruped animal. This method was employed to develop the biological models used in the subsequent chapters. Chapter 2 also investigates the effect of leg mass on the dynamics of trotting, pacing, bounding, and galloping to determine if models that neglect leg mass can accurately capture the dynamics of these gaits.

Chapter 3 extends Schmiedeler's [109] impulsive model of galloping to all dynamic gaits typically employed by biological quadrupeds. The vertical oscillations of the mass center are compared for locomotion at three different stride frequencies in each gait. The chapter introduces the theory that large vertical oscillations result in reduced energy efficiency and examines the trot-to-gallop transition from this perspective.

Chapter 4 develops spring-mass models of trotting and galloping that more closely approximate lower speed locomotion than do the impulsive models. It also introduces the theory that animals change from a trot to a gallop in order to minimize stride frequency. The model parameters for both trotting and galloping that result in motion with equal stride frequencies and vertical oscillations are compared to investigate the trot-to-gallop transition.

In combination, Chapters 3 and 4 address the question of why galloping is energetically advantageous at high speeds compared to trotting.

Chapter 5 mathematically formalizes the argument that large vertical oscillations of the mass center result in large energy losses. The kinetic energy loss of any system that collides plasticly with a stationary environment is applied specifically to the legs of a mobile robot, and the generalized inertia ellipsoid is introduced as a visualization tool for comparing the impact losses of different leg designs.

Chapter 6 uses biological data to develop an equation for selecting the stiffness of a quadruped robot's legs. A simple, kinetostatic analysis of the effective stiffness of articulated legs is introduced to aid in the geometric layout of a leg design.

Chapter 7 describes the detail design of a prototype articulated leg and the apparatus for testing the leg's performance. It explains how the goal to build a quadrupedal machine capable of galloping affected the design and why some early design concepts were eventually altered. In combination, Chapters 5, 6, and 7 address the question of how to design a legged robot to capture the advantages of galloping.

Chapter 8 examines the experimental results from the prototype leg's performance tests with a focus on verification of the mechanical design. Chapter 9 summarizes the contributions of this work and proposes topics for future research.

CHAPTER 2

BIOLOGICAL MODEL AND LEG MASS

2.1 Introduction

Analyzing and modeling the locomotion of a biological quadruped requires knowledge of the animal's geometric and inertial properties. Often times, this data is gathered by sacrificing the animal after the experiments are complete or else assuming similarity of body structure with an animal that has already been sacrificed [94] [126]. When sacrificing an animal is not possible due to expense or inconvenience, some other method of determining the geometric and inertial properties is needed. The first part of this chapter reviews one such method that was developed to arrive at reasonable parameters for the biological models employed in Chapters 3 and 4 [116].

The second part of this chapter investigates the validity of the common assumption that leg mass can be neglected in modeling quadrupedal locomotion. A model having massless legs is much simpler and requires much less computation time. The effect of leg mass on the dynamics of gait, though, has not been systematically studied from a mathematical perspective. The second part of this chapter uses simple principles of dynamics to examine the significance of leg mass in modeling several gaits.

2.2 Background

Dynamic simulation has become an important tool in the design and control of legged robots, especially robots capable of moving at high speeds with running gaits. Raibert [102] [103] and his colleagues used simulation extensively in developing their monopod, biped, and quadruped robots. More recently, both Furusho et al. [45] and Papadopoulous and Buehler [95] used simulation to evaluate the control of their bounding quadrupedal robots. Marhefka's [79] simulations were critical to the design of the prototype leg described in Chapter 7.

In parallel with robot simulation, mathematical modeling of running animals has improved the understanding of how dynamic locomotion is achieved in the biological world. Herr and McMahon's [54] [55] investigations of trotting and galloping and Wong and Orin's [131] [132] studies of jumping are recent examples. In modeling any type of legged locomotion, though, it is an ongoing challenge to capture the significant mechanics of gait while maintaining simplicity in the model. Freeman and Orin [39] formulated an efficient simulation approach specifically for quadrupeds to reduce computational requirements. One common modeling assumption to further reduce computation is that the legs of a quadruped are massless. This has been employed to develop simple spring-mass models of trotting [20] [34] [85] and different models for other gaits [16] [84] [91] [92] [113]. The simplification has been validated through several investigations.

Taylor et al. [126] studied cheetahs, gazelles, and goats with combined leg masses equal to 40%, 31%, and 19% of their total masses, respectively. The results indicated that the three animals, all having nearly the same total mass, expended roughly the same amount of energy in moving their legs relative to their bodies despite the differences in leg mass. The conclusion was that moving the legs relative to the body accounts for only a small part of

the energy expenditure or that elastic energy storage compensates for moving heavier legs. Pandy et al. [94] also studied the locomotion of goats, measuring each front leg to be 2.2% of the total mass and each hind leg to be 4.7% of the total mass. Their results indicated that the kinetic energy associated with moving the legs relative to the body is small compared to the total translational kinetic energy of the system. Alexander et al. [11] developed a two-dimensional model of quadrupedal running and estimated that the power required to return massive legs accounts for only about 16% of the total power at high speeds.

Apart from energy considerations, the relative motion of the legs can have a significant effect on the motion of the body. Alexander and Vernon [12] were able to predict the pitching motion of a kangaroo's body that resulted from the paired swinging of the legs during rapid hopping. To minimize this same body pitch, Raibert's [103] monopod was designed such that the body's moment of inertia was fourteen times that of the leg. In most forms of rapid bipedal locomotion, including human running where the legs have relatively large inertia, the leg movements do not cause significant body pitch because the two legs operate out of phase. The changes in angular momentum associated with the individual legs essentially cancel each other out. The same can be said for most quadrupedal running gaits. In the trot, pace, and bound, the legs operate in pairs that move nearly out of phase with one another. In the gallop, the legs operate individually, but rarely, if ever in a stride do three or four legs move in the same direction relative to the body at the same time.

System inertia appears to be critical to the stability of quadrupedal running gaits. In Raibert et al. [105], Murphy's planar simulations suggested that the bound is passively stable only if a dimensionless body inertia is less than unity. Highlighting the value of

neglecting leg mass for some analysis, Berkemeier [16] reached the same conclusion mathematically by constructing approximate return maps with a simplified model having massless, springy legs. Additionally, Nanua and Waldron [91] found that the pitch motion of their planar galloping model was chaotic when the pitch angle initial condition was too large. Since the pitch moment of inertia largely determines the body's pitching motion, this result also highlights the important relationship between inertia and stability in quadrupedal running.

2.3 Biological Model

This section reviews Siston's [116] work in developing a reasonably accurate biological quadruped model using a black labrador dog named Molly as the basic platform. This choice was convenient for a number of reasons, not the least of which were that she belonged to a colleague and was cooperative during data collection. A visual inspection revealed that Molly's legs were relatively heavier than those of a goat, yet relatively lighter than those of a cheetah. Thus, her leg mass proportions appeared to fall somewhere in the middle range of other quadrupeds. It was also observed that Molly ran with limited flexion in her back, allowing for a simpler model. Finally, Molly's size and structure were similar to those of previously photographed dogs from which leg angle data was taken for the various gaits.

2.3.1 Measuring Biological Parameters

All measurements involving Molly were designed to be simple and non-invasive. Her height, width, girth, and girdle were measured at various points of her body. Figure 2.1 is a profile view of one height measurement. The lengths of her leg segments, the thicknesses of those segments at several locations, the longitudinal distance between her shoulders and

Figure 2.1: Molly's profile during height measurement.

hips, and the lateral distance between both her two shoulders and two hips were all measured. Molly's mass of 33 kg was computed by simultaneously placing each of her four feet on an individual scale that had been calibrated, adding the four weight readings together, and dividing by the acceleration of gravity. These weight readings and the measured distances between the feet in the lateral and longitudinal directions were recorded for each of three trials. Variation among the trials was minimal, but the results were averaged. The data confirmed that Molly's mass distribution is essentially symmetric in the lateral direction and that her center of mass is closer to her shoulders than to her hips. Her front legs supported 65% of her body weight, which is consistent with previously published data. Jayes and Alexander [68] observed that dogs of various breeds support 61% of their body weight with their front legs, while Brown [21] cited a value of 60%.

An effort was made to at least approximately measure some of Molly's inertial properties. The moment of inertia, I, of any body can be calculated by measuring the period of oscillation of that body as a compound pendulum.

$$I = ml^2 \left[\left(\frac{T}{2\pi} \right)^2 \left(\frac{g}{l} \right) - 1 \right], \tag{2.1}$$

where m is the mass, l is the length of the pendulum, T is the period of oscillation, and g is the acceleration of gravity. A denim sling with four leg holes was constructed to hold Molly in a standing posture while she was swung as a compound pendulum. The sling was mounted to a rectangular aluminum frame that was in turn mounted to two bent aluminum rods. The rods were looped over a steel pipe to serve as the revolute joint for the compound pendulum. Two sets of rods having different lengths were used to swing Molly about an axis parallel to her pitch axis, and two additional sets were used to swing her about an axis parallel to her roll axis. Molly was given a light push, and the time required for five complete oscillations was recorded. Three separate trials were completed for each of two different pendulum lengths. Figure 2.2 is a photograph from one of the pitch experiments.

During the trials to calculate the roll moment of inertia, Molly moved around a great deal in the sling causing the rods to slip on the pipe. Therefore, the roll data was discarded because it did not represent an accurate measurement of the oscillation period. The three times for each pendulum length in the pitch experiments were averaged, and the corresponding pitch moment of inertia was calculated. For a pendulum length of .86 m, the pitch moment of inertia was calculated to be 2.87 $kg \cdot m^2$, and for a length of 1.01 m, it

Figure 2.2: Molly in a denim sling for calculation of her pitch moment of inertia.

was calculated to be 4.12 $kg \cdot m^2$. The variation between these two values may be a result of Molly moving around in the sling. The shorter pendulum experiments were performed first, when Molly was most docile.

2.3.2 Developing the Biological Model

Following all of the measurements, Molly's body structure was approximated with a combination of solid geometric primitives having uniform density. The head was modeled with a single sphere fixed to the torso, so neck motion was neglected. Twenty elliptical cylinders were used to model a rigid torso because the measurements indicated that Molly's body was more elliptical than circular. Each leg consisted of two circular cylinders connected by a revolute knee joint. No ankle joints were included, so the feet were lumped in with their corresponding shanks. Each leg was connected to the torso with a single revolute shoulder/hip joint, so the abduction/adduction motion of the legs was neglected. Figure 2.3 shows a profile view of the model's geometric primitives superimposed on an outline of Molly that was drawn from a photograph.

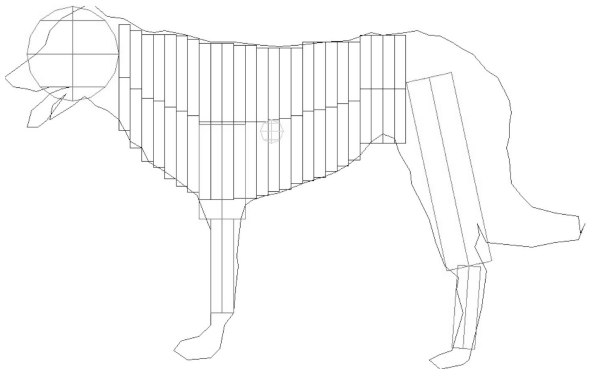

Figure 2.3: Outline of Molly's body with the geometric primitives of the model superimposed. The tail, which was not modeled, comprises most of the open section at the rear of the dog outline.

With this model, each front leg accounts for 5.1% and each hind leg for 9.1% of the total mass. The actual masses of Molly's legs could not be measured for comparison, but again, these values are consistent with previously published data. Fedak et al. [36] measured a dog of unspecified breed to carry 4.3% of its body weight in each of its front legs and 6.5% in each of its hind legs. Grand [47] measured those percentages to be 4.7% and 10.1% for a greyhound. The model's torso dimensions were fine-tuned such that the longitudinal position of the mass center matched that calculated from weighing the animal. The model's composite rigid body pitch moment of inertia for standing posture was calculated to be 2.80 $kg \cdot m^2$, which agrees well with the results of the shorter pendulum experiments.

2.4 Significance of Leg Mass

To investigate the effect of leg mass on the dynamics of various gaits, it is convenient to work with a simpler model having single degree-of-freedom legs. To this end, a model of Raibert's quadruped [103] is presented in the following section, and the subsequent mathematical analysis is developed directly for it. The results are then applied to the more complex biological model.

2.4.1 Robot Model

The robot model is shown in Figure 2.4 and consists of a rectangular parallelpiped body with four cylindrical legs attached to the body by four revolute joints. This configuration allows each leg to swing in the sagittal plane with a single degree of freedom, but neglects the abduction/adduction motion. Furthermore, the legs have a fixed length, so the telescoping motion is not modeled. The dimensions of the legs and body were selected to approximate the geometry of Raibert's quadruped, but greater priority was given to matching the inertial properties with simple, uniform density geometric primitives. The density of the legs is not

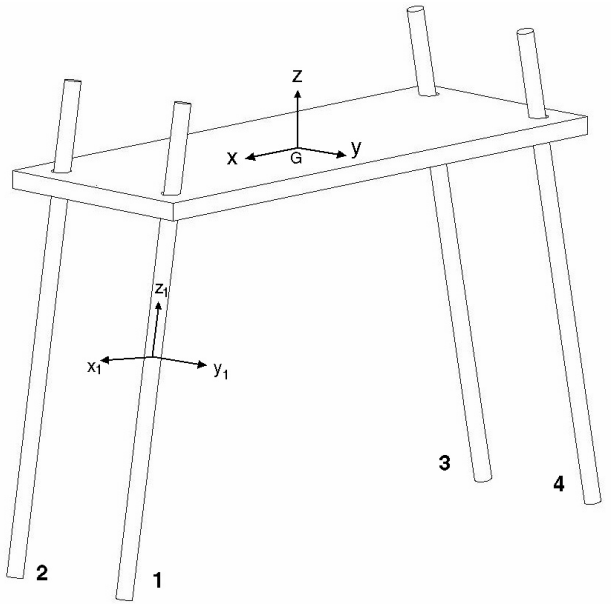

Figure 2.4: Quadruped robot model similar in structure to Raibert's quadruped.

the same as that of the body. Table 2.1 offers a comparison of the model's and the actual robot's geometric and inertial properties.

To generate the leg motions for the three gaits of Raibert's quadruped, the trot, pace, and bound, a couple of assumptions were made. First, the legs were assumed to move synchronously in pairs, with the two pairs moving precisely out of phase with each other. In this way, a positive rotation of one pair is mirrored by a negative rotation of the other. As discussed in Chapter 1, the legs are employed in diagonal pairs in the trot, lateral pairs in the pace, and front/hind pairs in the bound. Secondly, the range of motion of the legs was assumed to be the maximum allowed by the robot design, +/-33^o. The legs of a quadruped sweep through larger angles as speed increases [34], so this motion would be representative of the maximum speed of the robot. Furthermore, the subsequent analysis was carried out for the entire range of motion, so this simply provides a logical upper limit.

	Raibert quadruped	**Robot model**
Body mass (kg)	25.2	25.2
Body length (m)	1.05	0.874
Body width (m)	0.35	0.35
Body height (m)	-	0.027
Body moment of inertia, x-direction ($kg \cdot m^2$)	0.257	0.258
Body moment of inertia, y-direction ($kg \cdot m^2$)	1.60	1.60
Body moment of inertia, z-direction ($kg \cdot m^2$)	1.86	1.86
Hip spacing, x-direction (m)	0.776	0.776
Hip spacing, y-direction (m)	0.239	0.239
Leg mass (kg)	1.4	1.4
Leg length (m)	0.95	0.762
Leg diameter (m)	-	0.013
Hip height (m)	0.668 (max)	0.610
Leg stroke, spring (m)	0.102	-
Leg moment of inertia about hip ($kg \cdot m^2$)	0.14	0.14

Table 2.1: Geometric and inertial properties of Raibert's quadruped compared to the robot model.

2.4.2 Angular Momentum

Neglecting viscous air drag, no external moments act about a quadruped's mass center during a flight phase, so the angular momentum, $\mathbf{H}_G$, about the mass center is conserved. Rotation of the legs relative to the body can change the body's angular velocity, $\mathbf{\Omega}$, but the angular momentum of the system remains constant. The system angular momentum can be expressed in terms of separate contributions of the body and the four legs,

$$\mathbf{H_G} = \mathbf{H}_{G,body} + \sum_{i=1}^{4} \mathbf{H}_{G,leg_i}. \tag{2.2}$$

Expanding terms,

$$\mathbf{H}_{G,body} = I_{G,body}\mathbf{\Omega}, \tag{2.3}$$

and,

$$\mathbf{H}_{G,leg_i} = I_{G,leg_i}\mathbf{\Omega} + I_{G,leg_i}\omega_i, \tag{2.4}$$

where $I_{G,body}$ is the inertia matrix of the body, I_{G,leg_i} is the inertia matrix of leg i, and ω_i is the angular velocity of leg i relative to the body. All of these quantities are expressed relative to the coordinate system fixed in the body at the mass center of the entire system. The angular momentum can be rewritten in terms of the composite rigid body inertia matrix, $I_{G,CRB}$, of the system.

$$\mathbf{H}_G = I_{G,CRB}\mathbf{\Omega} + \sum_{i=1}^{4} I_{G,leg_i}\omega_i. \tag{2.5}$$

The leg inertia in Equation 2.5 can be expanded in the form,

$$I_{G,leg_i} = R_i^T \bar{I} R_i + m(\mathbf{s}_i^T \mathbf{s}_i[1] - \mathbf{s}_i \mathbf{s}_i^T), \tag{2.6}$$

where $\bar{I}$ is the inertia matrix of each leg expressed relative to its own coordinate system, R_i is the rotation matrix between the body-fixed coordinate system and the coordinate system of leg i, m is the leg mass, $\mathbf{s}_i = \{\, s_{ix} \quad s_{iy} \quad s_{iz} \,\}^T$ is the position vector from the body-fixed coordinate system to the coordinate system of leg i, and $[1]$ is the 3 x 3 identity matrix. Since each leg is a circular cylinder, $\bar{I}$ is a diagonal matrix. If θ_i is the joint angle of leg i, then,

$$R_i = \begin{bmatrix} \cos(\theta_i) & 0 & -\sin(\theta_i) \\ 0 & 1 & 0 \\ \sin(\theta_i) & 0 & \cos(\theta_i) \end{bmatrix}. \tag{2.7}$$

Substituting Equation 2.6 into Equation 2.5,

$$\mathbf{H}_G = I_{G,CRB}\mathbf{\Omega} + \sum_{i=1}^{4} R_i^T \bar{I} R_i \omega_i + \sum_{i=1}^{4} m(\mathbf{s}_i^T \mathbf{s}_i[1] - \mathbf{s}_i \mathbf{s}_i^T)\omega_i. \tag{2.8}$$

Noting that $\omega_i = \{\, 0 \quad \omega_i \quad 0 \,\}^T$ because each leg has a single degree of freedom, that all of the ω_i's are equal in magnitude, and that two of the ω_i's are opposite in sign to the other two because the legs move in pairs out of phase, the first summation goes to zero regardless

	s_{ix}	s_{iy}	s_{iz}	ω_i
Trotting				
1	s_{1x}	s_{1y}	s_{1z}	ω_1
2	s_{2x}	$-s_{1y}$	s_{1z}	$-\omega_1$
3	$-s_{2x}$	$-s_{1y}$	s_{1z}	ω_1
4	$-s_{1x}$	s_{1y}	s_{1z}	$-\omega_1$
Pacing				
1	s_{1x}	s_{1y}	s_{1z}	ω_1
2	s_{2x}	$-s_{1y}$	s_{1z}	$-\omega_1$
3	$-s_{1x}$	$-s_{1y}$	s_{1z}	$-\omega_1$
4	$-s_{2x}$	s_{1y}	s_{1z}	ω_1
Bounding				
1	s_{1x}	s_{1y}	s_{1z}	ω_1
2	s_{1x}	$-s_{1y}$	s_{1z}	ω_1
3	$-s_{1x}$	$-s_{1y}$	s_{1z}	$-\omega_1$
4	$-s_{1x}$	s_{1y}	s_{1z}	$-\omega_1$

Table 2.2: Parameter simplifications for trotting, pacing, and bounding.

of the joint angles. This leaves only the second summation to vary among the three gaits. Table 2.2 lists the parameter simplifications to be substituted into this summation for each gait.

2.4.3 Trotting

Making the trotting substitutions from Table 2.2 in Equation 2.8, the angular momentum of the robot model is given by,

$$\mathbf{H}_G = I_{G,CRB}\boldsymbol{\Omega} + \begin{Bmatrix} -2ms_{1y}(s_{1x} + s_{2x})\omega_1 \\ 0 \\ 0 \end{Bmatrix}. \tag{2.9}$$

The second term results from the legs operating in diagonal pairs. At maximum leg rotation, the legs on one side are extended outward from the body, while the legs on the other side

are gathered together underneath the body. For all but the special case of $s_{1x} = -s_{2x}$ when all four legs are in the vertical position, the changes in angular momentum of moving the legs in this manner do not cancel.

Since support is provided at opposite ends of the body in trotting, $\mathbf{\Omega}$ is typically negligible as the body moves forward and up and down without significant rotation. The second term in Equation 2.9 suggests, however, that the changes in the angular velocity of the legs relative to the body may cause body rotation in the roll direction to maintain constant angular momentum. Small pitch and yaw rotation would normally be expected also, except that the composite rigid body products of inertia in $I_{G,CRB}$ are uniformly zero for trotting. Examining how the magnitude of the coefficient $2ms_{1y}(s_{1x} + s_{2x})$ compares with the magnitude of the composite rigid body roll moment of inertia gives an indication of how the changes in the angular velocity of the legs will affect the roll angular velocity of the body. These results are presented in Section 2.5.1.

2.4.4 Pacing

Making the pacing substitutions from Table 2.2 in Equation 2.8, the angular momentum of the robot is simply,

$$H_G = I_{G,CRB}\mathbf{\Omega}. \tag{2.10}$$

The changes in angular momentum associated with the legs cancel. Since support is provided on opposite sides of the body in pacing, $\mathbf{\Omega}$ typically has the form $\{\,\Omega \quad 0 \quad 0\,\}^T$, such that the dominant rotation of the body is in the roll direction. Therefore, the dominant term in the angular momentum calculation is the product of the roll angular velocity and the composite rigid body roll moment of inertia. The composite rigid body products of inertia are less than one eighth of the roll moment for all pacing motions. Examining how the

movement of the legs relative to the body affects the composite rigid body roll moment of inertia indicates how significantly the body's roll motion will be affected. These results are presented in Section 2.5.2.

2.4.5 Bounding

Making the bounding substitutions from Table 2.2 in Equation 2.8, the angular momentum of the robot is again given by,

$$H_G = I_{G,CRB}\boldsymbol{\Omega}. \tag{2.11}$$

As in pacing, the changes in angular momentum associated with the legs cancel. For bounding, however, $\boldsymbol{\Omega}$ typically has the form $\{\, 0 \quad \Omega \quad 0 \,\}^T$, such that the dominant rotation of the body is in the pitch direction. The composite rigid body products of inertia are uniformly zero for bounding, so the effect of the leg motion on the composite rigid body pitch moment of inertia indicates the corresponding effect on the body's pitch motion. The results are presented in Section 2.5.3.

2.4.6 Extension to the Biological Model

The preceding mathematical formulation does not apply equally well to the biological model developed in Section 2.3.2. First, the legs of an animal do not move perfectly out of phase with each other. Rather, the leg motions of the biological model were determined by analyzing photographs taken of dogs having similar size and structure as they moved with various gaits. Line segments were drawn on each photograph to represent the positions of the thigh and shank. The angles of these line segments were then measured, and the model leg segments were set to match them for each photograph in the sequence. The pace angles came from four photographs and the gallop angles from seven photographs taken by

Muybridge [90]. In each case, the chosen number of frames represented the full range of leg motions for nearly one stride.

A second important difference is that the legs of the biological model have two degrees of freedom rather than one. Because of the knee flexion, the inertia matrices of these legs are not necessarily diagonal, as they are for the robot model. Still, the structure and movements of the dog model bear enough similarities to those of the robot model to justify some simple extrapolations. It is reasonable to assume that the products of the composite rigid body moments of inertia and the corresponding body angular velocities will be the dominant terms in the angular momentum calculations. Therefore, it is still reasonable to look at the changes in the composite rigid body moments of inertia with leg movement as indications of the need for including leg mass in a model to accurately capture the dynamics.

2.5 Results

The results for the robot and biological models are presented for each gait in the following sections.

2.5.1 Trotting

For all trotting motions of the robot model, the coefficient $2ms_{1y}(s_{1x}+s_{2x})$ in Equation 2.9 is between 30% and 40% of the composite rigid body roll moment of inertia. A corresponding value for the biological model is non-sensical because the legs have two degrees of freedom. This suggests that the change in the body's angular velocity would be between 30% and 40% of the legs' change in angular velocity during a flight phase. The net result is that the movement of the legs relative to the body has significant effect on the dynamic motion of the body in trotting. Granted, during a flight phase, the angular velocity of the legs may increase in one direction as the legs are moved forward and then return to near

its initial value prior to the next touchdown. Still, the significance of the second term in Equation 2.9 relative to the composite rigid body roll moment of inertia indicates that leg mass should be included to accurately model the roll motion of the body in trotting.

2.5.2 Pacing

Figure 2.5 plots the roll moment of inertia for the robot model over the full range of leg motions. For comparison, the roll moment of inertia is also plotted for two simplified models: one that lumps the mass of each leg at a single point at the shoulder/hip joint and another that neglects leg mass entirely by equally distributing it within the torso. Figure 2.6 plots the same quantities for the biological model. Both plots clearly indicate that the

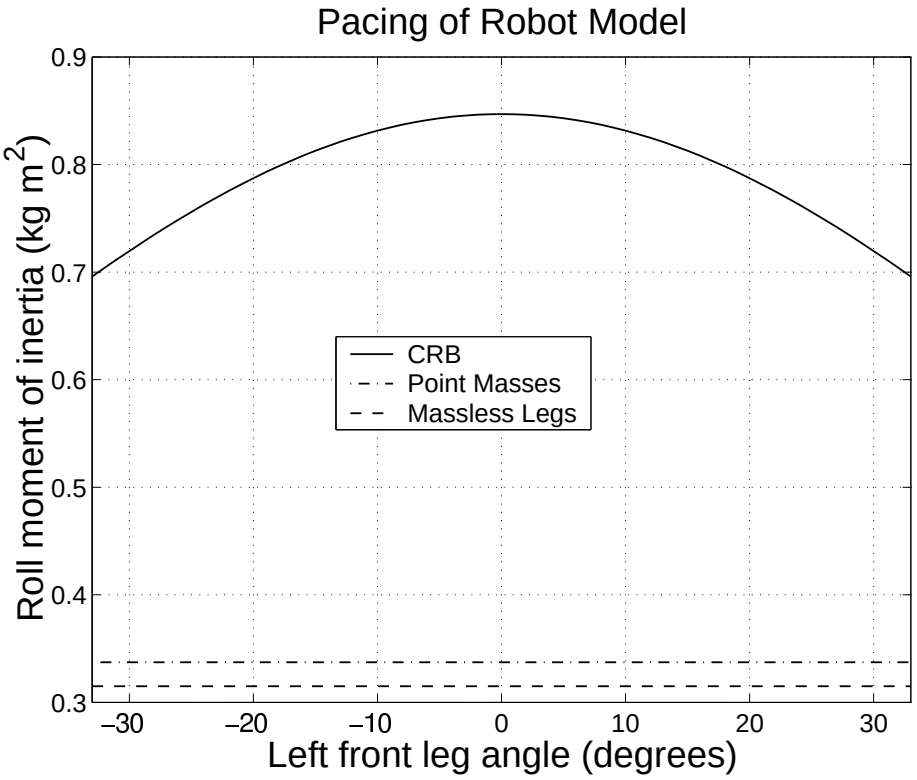

Figure 2.5: Roll moment of inertia for pacing of the robot model

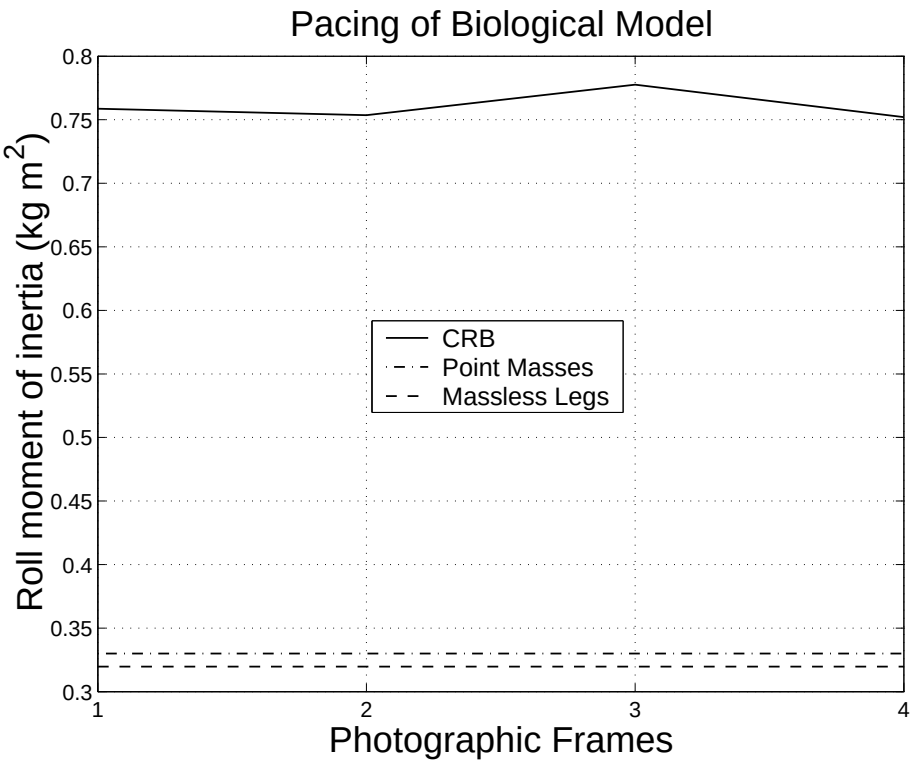

Figure 2.6: Roll moment of inertia for pacing of the biological model

simplified models drastically underestimate the roll moments of inertia. In a simulation, this disparity would yield much larger motion in the roll direction than would be seen in the real system. In the case of the biological model, however, the roll moment of inertia does not change significantly with the motion of the legs. Therefore, leg mass could be neglected without loss of accuracy provided that the roll moment of inertia for the body is computed with the inclusion of the massive legs. In the robot model, the roll moment of inertia changes by as much as 18% with the motion of the legs. To accurately capture the roll motion in this case, leg mass would need to be included in the simulation.

2.5.3 Bounding

Figure 2.7 plots the pitch moment of inertia for the robot model and the simplified models over the full range of leg motions. As with pacing, the simplified models again underestimate the critical moment of inertia. For bounding, however, the pitch moment of inertia changes even more significantly as the legs move. From a mean value when the legs are in the vertical position, it fluctuates by as much as 18% in either direction. This indicates that including leg mass in a model is even more important for accurately capturing the dynamics of the bound than it is for the pace.

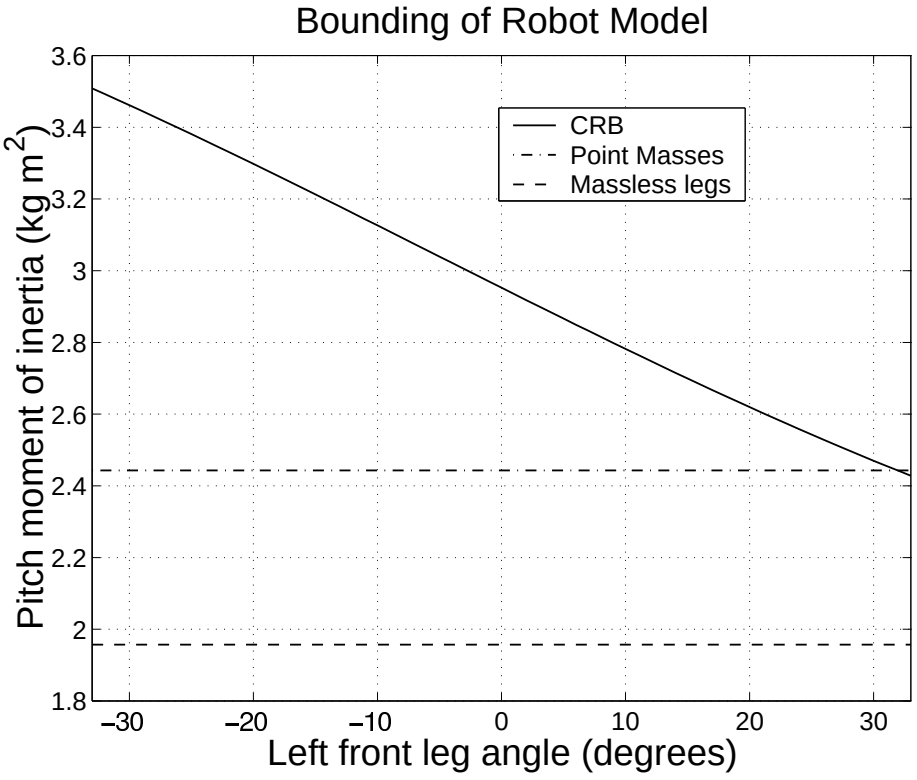

Figure 2.7: Pitch moment of inertia for bounding of the robot model

No data are presented for the biological model because no photos of dogs bounding were available. Bounding is a relatively rare gait for dogs to use on hard, level terrain, as they typically gallop instead. Bounding is more commonly observed when a dog is running in shallow water, through relatively deep snow, or up an incline [66].

2.5.4 Galloping

Figure 2.8 plots all three moments of inertia for galloping of the biological model. Similar to bounding, the pitching motion of the body dominates in galloping. Unlike the bound, however, the feet touchdown individually, so some roll and yaw motion are also expected. No data are presented for the robot model because like all other quadrupeds built

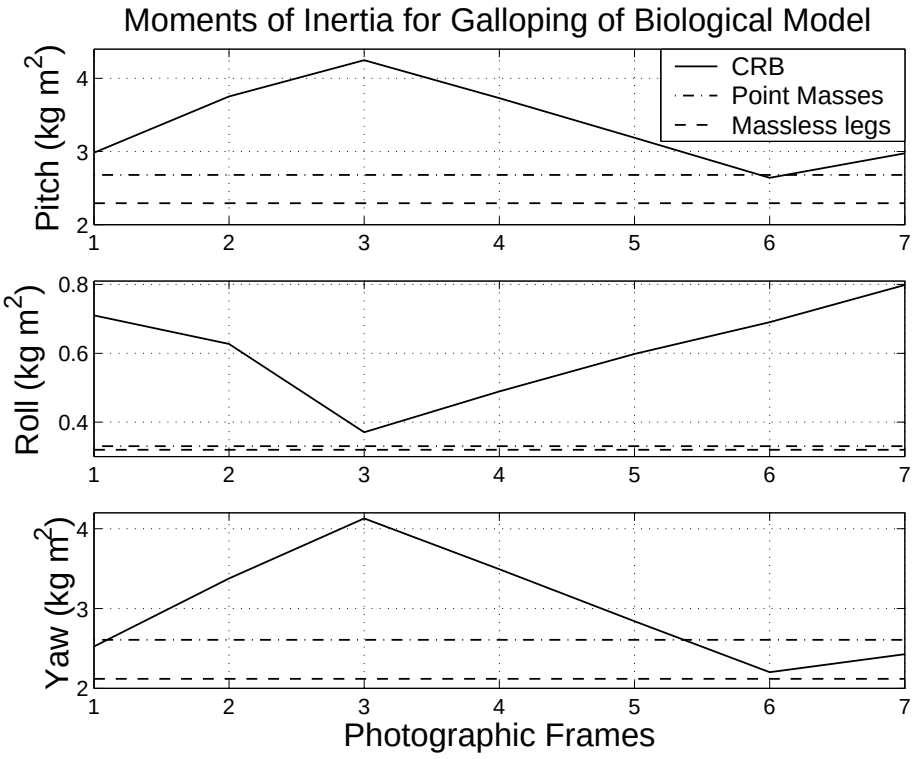

Figure 2.8: Moments of inertia for galloping of the biological model

to date, Raibert's quadruped was not capable of galloping. No formulation for the angular momentum of a galloping model is given in Section 2.4 either, primarily because the legs do not move synchronously in the gallop. This leads to a complex expression for the angular momentum that does not provide the same insights as the expressions for trotting, pacing, and bounding. Still, the variations in the moments of inertia give a general indication of how the motion of the legs affect the overall motion of the body.

As for the other gaits, the simplified models underestimate the moments of inertia in galloping. Also, comparing the plots in Figure 2.8 to the preceding plots for the other gaits, it is clear that all of the moments of inertia changes more significantly with the leg motions in galloping. From their mean values, the pitch moment of inertia varies positively and negatively by more than 20%, the roll moment by more than 30%, and the yaw moment by more than 25%. Therefore, including leg mass in a galloping model is even more important to capture the dynamics of the motion than it is for the other gaits.

2.6 Summary

Some simple, non-invasive measurement techniques can be employed to develop a reasonably accurate model of a biological quadruped when sacrificing the animal is not a viable option. Analyzing the changes in system angular momentum during a flight phase gives an indication of how significantly the movement of massive legs relative to the body affects the body's motion. To accurately model trotting, leg mass should be included in order to account for the roll motion of the body caused by the leg rotation. At slow speeds, though, this effect will be less significant, and the dynamics may still be accurately modeled with massless legs. For pacing, leg mass should be included at the very least in computing the roll moment of inertia of the system. In this work, that roll moment was found not

to change much for the biological model, but to change significantly for the robot model. In modeling bounding, leg mass should be included because the extension of the legs out from the body and their gathering underneath the body have a dramatic effect on the pitch moment of inertia. Of all the gaits, leg mass is most critical in capturing the dynamics of galloping. Pitch, roll, and yaw motion are all found in galloping, and the movements of the legs have significant effect on the system moments of inertia. Since the gallop is the highest speed gait among biological quadrupeds and involves complex body motions, stability is an important issue. Useful stability analysis cannot be achieved without an accurate dynamic model, which is one that includes leg mass.

The results presented in this chapter do not suggest that models with massless legs are without value. On the contrary, they can be very useful in explaining general phenomena and investigating many behaviors, as they are in the following chapters. In simulating a robotic system or developing a highly detailed account of animal locomotion, however, these models may be inadequate.

CHAPTER 3

IMPULSIVE MODEL

3.1 Introduction

Unlike wheeled and tracked vehicles, locomotion with legs fundamentally involves fluctuations in gravitational potential energy. In two- [25], four- [24], and even eight-legged [19] walking, the mass center rises to its maximum elevation when the horizontal velocity reaches its minimum value and then falls to its minimum elevation as the horizontal velocity increases to its maximum value. In this way, the exchange of gravitational potential energy with horizontal kinetic energy reduces the energetic cost of locomotion. It is typically referred to as the "rolling egg" or "inverted pendulum" mechanism of energy exchange. Six-legged walkers likely also display this behavior, but work to date has been unable to record data for steady-state walking of cockroaches [43] [44].

In bipedal running [26] [37], quadrupedal trotting [24], and similar bouncing gaits of six- [43] [44] and eight-legged [19] animals, the fluctuations in gravitational potential energy and horizontal kinetic energy are very nearly in phase, so little or no exchange is possible. Instead, gravitational potential energy is exchanged with elastic energy stored in the muscles and tendons [4]. This is typically referred to as the "bouncing ball" mechanism of energy exchange.

In asymmetrical gaits like quadrupedal galloping [24] and bipedal skipping [87], the energy exchange involves both mechanisms. In slow galloping, the body falls forward and the horizontal velocity increases while the hind legs are in the support phase. During the initial support phase of the front legs, the body rises as the horizontal velocity decreases. The rolling egg mechanism is employed in these portions of the stride. To initiate the gathered flight phase, the front legs thrust such that the horizontal velocity increases as the mass center rises. Then, at the end of the gathered flight phase, the horizontal velocity briefly decreases along with the elevation of the mass center as the hind legs begin their support phase. These portions of the stride feature the bouncing ball mechanism. As speed increases and an extended flight phase appears, this mechanism dominates because the energy fluctuations become almost entirely out of phase. In skipping, like galloping, the rolling egg mechanism appears in the middle of the support phase, and the bouncing ball mechanism is found immediately prior to and immediately following the flight phase.

While some oscillation of the mass center in the vertical direction is necessary in legged locomotion, particularly large oscillations are undesirable because they yield large energy losses when the feet impact the ground. This argument is formalized mathematically in Chapter 5. Alexander [6] offered a different perspective on the same idea by quantifying how "troublesome" excessive vertical oscillations are with the dimensionless quantity $\frac{g}{f^2 H}$, where g is the acceleration of gravity, f is the stride frequency, and H is the hip height.

Since walking involves no flight phases, the foot impacts are generally not severe. Top speed in walking, however, is limited in part by the maximum achievable fluctuation in potential energy. Thus, longer strides are taken as walking speed increases in order to generate larger vertical oscillations of the mass center [27]. In running gaits, impact losses limit the amount of gravitational potential energy that can be converted to elastic energy, thus

reducing the efficiency of moving with large vertical displacements. As speed increases, the storage of elastic energy becomes more important, and the vertical oscillations tend to become smaller [24].

This chapter extends a mathematical model initially developed for galloping to all dynamic gaits typically employed by biological quadrupeds. It compares the vertical oscillations of the mass center in all of the gaits at three different stride frequencies. The focus is to compare trotting and galloping in order to better understand the preference for galloping at high speeds.

3.2 Background

Hoyt and Taylor [67] measured that small horses consume more oxygen per unit distance traveled when trotting rather than galloping at speeds above their natural trot-to-gallop transition speed. They concluded that animals naturally select gaits in order to minimize their energy consumption. Minetti et al. [88] achieved similar results with much larger horses. Muybridge [90] observed that some quadrupeds, like the cheetah shown in Figure 3.1, flex their backs in the sagittal plane when traveling with an asymmetrical gait such as

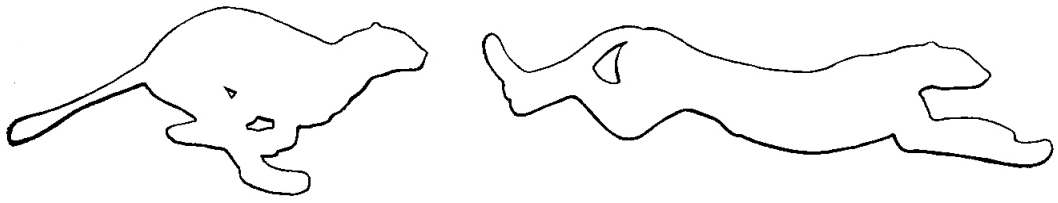

Figure 3.1: Cheetah flexing its back in a rotary gallop, from Hildebrand [56].

the rotary gallop. No such flexion can occur in symmetrical gaits like the trot, and this fact is commonly used to account for the energetic advantage of galloping at higher speeds.

Hildebrand [56] suggested that flexing the back increases the attainable stride length and allows a quadruped to increase its speed. Taylor [124] viewed the muscles and tendons in the bending trunk as compliant elements capable of storing more elastic energy than could the legs by themselves. Alexander's subsequent work supported this theory with experimental data [9] and extended it by arguing that the elastic energy stored is employed to help return the legs during flight phases [5].

Some of Taylor's [126] earlier work both supported Alexander's theory and highlighted the limitations of attributing the advantages of galloping exclusively to back flexion. This work determined that a cheetah, a gazelle, and a goat, all having roughly the same mass, expended about the same amount of energy to move their legs relative to their bodies during rapid locomotion. This result is significant because the cheetah had much heavier legs and moved with much greater back flexion. Elastic energy storage in the cheetah's back could account for the equivalence in energy expended despite its heavier legs. Galloping, however, is still the high speed gait of choice for goats and most other quadrupeds with relatively rigid backs. Nanua and Waldron [92] used a simple model to show that galloping does in fact require less energy than trotting at high speeds even if the back is rigid.

Back flexion likely does reduce the energetic cost of galloping at high speeds, but it does not appear to be the only advantage of galloping. One alternative explanation is that galloping requires smaller vertical oscillations of the mass center at high speeds. Gambaryan [46] suggested that smaller vertical oscillations promote higher endurance and noted that most open space dwelling animals experience smaller vertical oscillations in galloping than in trotting. He observed that this is particularly true of ungulates. Cavagna, Heglund, and

Taylor [24] made the same observation with dogs, and mathematical models developed by both McMahon [84] and Nanua and Waldron [92] displayed this behavior.

Related work also indirectly supports these conclusions. Rubin and Lanyon [107] measured an increase in bone strain at the walk-to-trot transition and a decrease in bone strain at the trot-to-gallop transition in both horses and dogs. Biewener and Taylor [17] made similar bone strain measurements with trotting and galloping goats. Taylor [35] later refined his earlier work with small horses to show that gait transitions are actually triggered by musculoskeletal forces rather than energy consumption, with those forces dropping at the trot-to-gallop transition. These phenomena are at least consistent with an increase in vertical oscillations from walking to trotting and a decrease from trotting to galloping.

Schmiedeler et al. [110] introduced a simple model for why galloping involves smaller vertical oscillations than trotting does. In high speed locomotion, the duty factor of each leg is relatively small, so the ballistic flight phases are dominant in the stride cycle. The variation in height, h, of the mass center during a flight phase is given by,

$$h = \frac{gl^2}{8u_x^2}, \tag{3.1}$$

where g is the acceleration of gravity, l is the horizontal distance traversed, and u_x is the horizontal velocity. Different gaits can be directly compared with this equation assuming that they have equal stride lengths and frequencies and that the support phases comprise a negligible portion of the stride.

In the pronk, all four legs operate in unison, so the length of the ballistic trajectory is equal to the stride length, l_s.

$$h = \frac{gl_s^2}{8u_x^2}. \tag{3.2}$$

In trotting, pacing, and bounding, the legs operate in pairs, so theoretically, l could be equal to $\frac{l_s}{2}$ if the two ballistic trajectories are equal in length, which would yield,

$$h = \frac{g l_s^2}{32 u_x^2}. \tag{3.3}$$

The vertical displacement of the mass center in these gaits is one fourth that in the pronk, as shown by the tracings of the parabolic trajectories in Figure 3.2. While the two flight phases in trotting and pacing are generally equal, they are typically unequal in bounding.

In galloping, the legs operate individually, so, theoretically the vertical displacement could again be reduced by a factor of four if the footfalls are symmetrically spaced in the stride.

$$h = \frac{g l_s^2}{128 u_x^2}. \tag{3.4}$$

This is indicated by the four smallest ballistic trajectories in Figure 3.2. In the biological world, though, no animal has ever been observed to employ a symmetrical gallop [46]. In fact, Schmiedeler [109] showed that the asymmetrical phasing of the legs in galloping results from the legs operating at an optimal working length. This suggests that while it may be advantageous to minimize vertical oscillations of the mass center, the mechanics of the

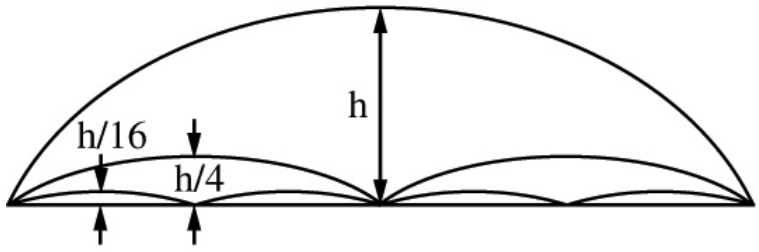

Figure 3.2: The vertical displacement of the mass center in the pronk, shown as h, the trot, pace or bound, shown as $\frac{h}{4}$, and the gallop, shown as $\frac{h}{16}$, assuming symmetrical phasing of the legs and negligible duty factors.

legs must be taken into consideration. The subsequent analysis in this chapter investigates the vertical oscillations of the mass center in various gaits with the legs constrained to operate at their optimal working length. The results indicate how the asymmetrical phasing of the legs and the rotation of the body affect the theoretical vertical displacement calculations in Equations 3.3 and 3.4.

3.3 Model Description

The quadruped model in this work was adapted from the model developed by Schmiedeler and Waldron [111] [113]. A schematic is shown in Figure 3.3, and the model is described briefly to highlight the key assumptions and modifications.

The model has a mammalian structure with a rigid trunk and massless legs that are attached in upright posture. No head or tail is modeled. The legs are drawn in Figure 3.3 without knee or ankle joints for simplicity, but the present application of the model deals with articulated legs. The shoulder joints, hip joints, and center of mass all lie in a plane. The shoulder and hip joints each have one degree of freedom, so the legs move only in the

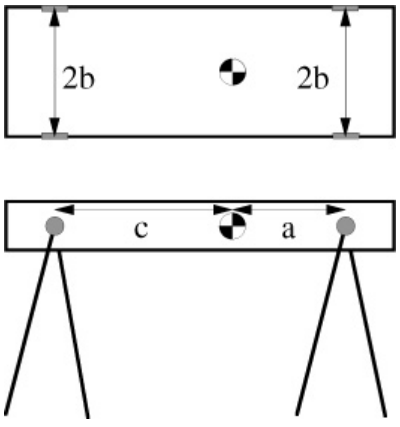

Figure 3.3: Schematic views of the quadruped model from the top and side. Forward motion is left to right.

sagittal plane.

The geometric and inertial parameters for the model were taken from the measurements of the dog detailed in Chapter 2, although the products of inertia were neglected. As such, the body is laterally symmetric, but not longitudinally symmetric because the center of mass is closer to the shoulders than to the hips. Since the model neglects leg mass, each moment of inertia was determined by averaging the calculated values over the course of leg motion for the trot, pace, and gallop and then taking the mean of the three averages. This at least minimally accounts for the effect of leg motion on the system inertia. In Figure 3.3, the trunk is drawn as a rectangular parallelepiped. The geometric parameters listed in Table 3.1, though, are the only pertinent dimensions in the model, and since the inertial parameters in the table were computed from the dog model in Chapter 2, they do not correspond to any single polyhedron of uniform density.

As previously stated, the legs are constrained to operate at an optimal working length, L_o, where the length of a leg is defined to be the distance from the center of the shoulder/hip

Parameter	**Value**	**Units**	**Description**
a	0.17	m	Longitudinal distance, mass center to shoulders
c	0.31	m	Longitudinal distance, mass center to hips
b	0.08	m	Lateral distance, mass center to shoulders/hips
L_o	0.7	m	Optimal working length of legs
m	33	kg	Trunk mass
I_x	0.69	$kg \cdot m^2$	Moment of inertia about roll axis
I_y	3.37	$kg \cdot m^2$	Moment of inertia about pitch axis
I_z	2.94	$kg \cdot m^2$	Moment of inertia about yaw axis

Table 3.1: Geometric and inertial parameters of the quadruped model.

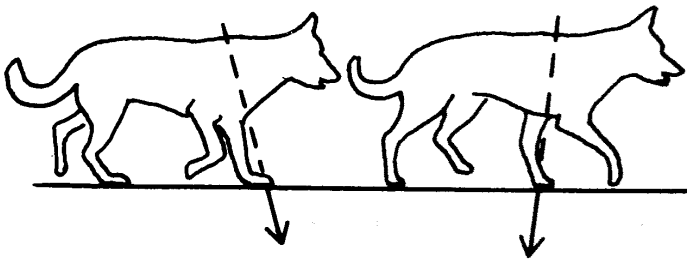

Figure 3.4: Foot force directions for a running dog, from Alexander [3].

joint to the center of the corresponding foot. A thorough justification of this assumption is provided by Schmiedeler and Waldron [113]. The legs are also assumed to act as pure thrust generators, with the line of action of the foot force passing directly through the corresponding shoulder or hip joint. Alexander's [3] and Elftman's [33] analysis of mammals running over force plates, like the dog in Figure 3.4, suggested that this assumption is at least approximately true, and Full, Blickhan, and Ting [41] demonstrated its validity for running arthropods. With this assumption, the configuration of the massless legs need not be considered. Rather, knowledge of the leg thrust line of action and magnitude alone are enough to determine the resulting change in motion of the quadruped's trunk.

The thrust imparted by a leg to the trunk at each footfall is represented by its impulse, shown in component form in Figure 3.5. Agrawal and Waldron [1] proposed that such a model is a valid approximation of high speed galloping when the duty factor of each leg is small. Schmiedeler and Waldron [113], however, offered a detailed argument for the validity of the model at lower speeds and higher duty factors.

The model only addresses straight-line motion, so the lateral components of the impulses are neglected since they are significant only when the quadruped is turning [94]. This eliminates all translation in the lateral direction, resulting in a five degree-of-freedom

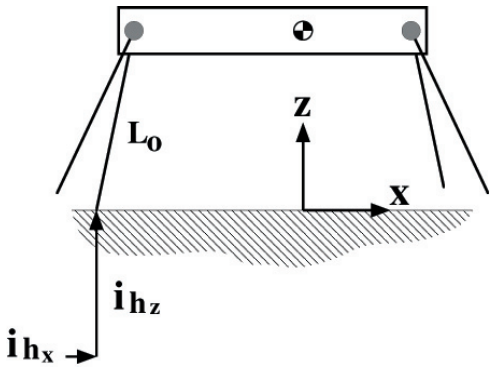

Figure 3.5: Quadruped model with hind leg instantaneously in contact with the ground.

model. The rigid trunk translates vertically and longitudinally and rotates freely about three perpendicular axes. The changes in orientation of the quadruped's trunk relative to the terrain are assumed to be small enough to validate the small angle approximation for the roll, pitch, and yaw angles. This assumption is common to other models of dynamic quadrupedal locomotion [3] [11]. The impulses of the two front legs are assumed to be equal, as are the impulses of the two hind legs. This simplification is based upon the work of Bryant et al. [23] who measured the ground reaction forces of the leading and trailing legs of a pair to be roughly equal.

The behavior of the model for each gait was investigated by solving the constrained equations of steady-state motion over flat, level terrain. This is a modification to the original model proposed by Schmiedeler and Waldron [113]. They studied motion over flat terrain of various inclines in order to determine the effect of drag on footfall phasing, with drag represented by an equivalent gradient, as proposed by Hill [61]. The current model assumes that all energy losses affecting the horizontal motion, including air resistance, soil work, and friction, can be lumped into a single, constant drag force acting through the mass center in the direction opposite forward progression. The primary difference is that the effective

acceleration of gravity perpendicular to the terrain does not change with an increase in drag as it did in the original model. Drag has typically been ignored in other locomotion models, although it has been studied with humans [100] and cockroaches [42].

All of the steady-state motion equations were formulated using two basic principles of rigid body dynamics: conservation of momentum and ballistic motion. The systems of equations were solved numerically with a simple continuation method derived from the work of Wampler et al. [130] and described in detail by Schmiedeler [109]. The solutions for all of the gaits were found at equal stride frequencies. This is also a modification to the original model in which an assumed relationship between the stride length and the level of drag was used to compute the appropriate stride period. Here, the focus is on the vertical oscillations of the mass center, so the gaits are compared at equal velocities and stride frequencies. Vertical oscillations can always be reduced by increasing the stride frequency.

Heglund and Taylor [52] developed a number of allometric equations for the equivalent speeds and the stride frequencies employed at those speeds of a wide range of quadrupeds. In this work, the gait analysis is performed for stride frequencies corresponding to the preferred trotting speed, the trot-to-gallop transition speed, and the preferred galloping speed in order to investigate if the results are dependent upon speed and stride frequency. For the model's mass of 33 kg, these speeds are 2.37, 3.28, and 5.14 $\frac{m}{s}$, respectively. Speeds outside this range were determined to be either too slow or too fast to apply reasonably well to all of the gaits. Since stride period is simply the inverse of the stride frequency and a more convenient quantity in this formulation, the three corresponding stride periods are 0.47, 0.40, and 0.39 s. The stride period changes much more dramatically over the range of trotting speeds than it does over the range of galloping speeds, as is typical of almost all biological quadrupeds [52]. In trotting, speed is increased predominantly by increasing

Parameter	Units	Description
g	$\frac{m}{s^2}$	Gravitational acceleration
D	N	Drag force
T	s	Stride period
u_x	$\frac{m}{s}$	Average horizontal speed
u_{xo}	$\frac{m}{s}$	Initial horizontal speed
t_i	s	Time of footfall i, where $i = 1, 2, 3, 4$
z_i	m	Mass center vertical position at footfall i
u_{zo}	$\frac{m}{s}$	Initial vertical velocity of mass center
d_f	m	Longitudinal distance, mass center to front footfall locations
d_h	m	Longitudinal distance, mass center to hind footfall locations
θ_{x1}	rad	Initial trunk roll angle
θ_{y1}	rad	Initial trunk pitch angle
ω_{xo}	$\frac{rad}{s}$	Initial trunk roll angular velocity
ω_{yo}	$\frac{rad}{s}$	Initial trunk pitch angular velocity
ω_{zo}	$\frac{rad}{s}$	Initial trunk yaw angular velocity
i_{fx}	$N \cdot s$	Longitudinal component of front impulses
i_{fz}	$N \cdot s$	Vertical component of front impulses
i_{hx}	$N \cdot s$	Longitudinal component of hind impulses
i_{hz}	$N \cdot s$	Vertical component of hind impulses

Table 3.2: Parameters common to the constrained steady-state equations for all gaits.

stride frequency, whereas in galloping, speed is increased predominantly by increasing stride length.

Table 3.2 lists the parameters that are found in the constrained steady-state equations corresponding to each gait. θ_{z1}, which would be the initial trunk yaw angle, does not appear as a parameter in Table 3.2. It is taken to be zero in all cases since the model deals with straight-line motion. The trunk does yaw during a stride in some of the gaits, but the yaw angle at the beginning and end of each stride is zero.

The acceleration of gravity was taken to be 9.81 $\frac{m}{s^2}$ for all of the analysis. The drag force was also held constant at a value of 47 N, which is reasonable for rapid locomotion as it is roughly equivalent to traversing an 8^o gradient. This value was the minimum level of drag for which physically meaningful solutions to the trotting equations could be found for all three stride periods. With less drag, the longitudinal components of the impulses were too small, and the pitch moments on the trunk could not be balanced with the legs constrained to operate at their optimal working length. This problem stems in part from the roll motion of the trunk in the trot, which is not typically found in trotting animals. The difference is that animals can compensate for the tendency of their bodies to roll, pitch, and yaw by contracting their muscles to exert moments across their shoulder and hip joints. The current model does not have the ability to exert moments across its shoulders and hips, so the resulting roll motion is larger than that observed in nature. This effect is found in the results for several gaits, and it explains why the drag force must be at least 47 N to satisfy the trotting equations.

3.4 Gaits

All of the gait sequences in this work begin with the left front footfall, although any of the footfalls could be selected as the first without altering the results. Some of the equations would change, but the motion would be identical. Similarly, if the sequences were initiated with the right front footfall and the order of the footfalls reversed, the resulting motion would also be identical. A brief explanation is given for the equations corresponding to the transverse gallop, and then only the constraint equations unique to the other gaits are subsequently addressed. A sample solution, calculated at the trot-to-gallop transition speed and stride frequency, is listed for each gait.

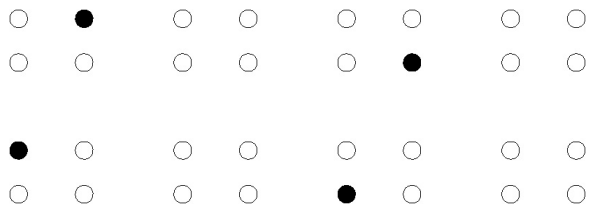

Figure 3.6: Support diagram of the transverse gallop.

3.4.1 Transverse Gallop

The footfall sequence for the transverse gallop is left front, right front, left hind, right hind, and the support diagram is shown in Figure 3.6. Each set of four circles in the figure represents the four legs of the quadruped at a progressive time in a stride. Forward motion is from left to right and is divided into two rows. A solid circle indicates that the leg is in contact with the ground providing support, and an open circle indicates that the leg is in the air returning to the appropriate position for its next period of support. A single stride begins at the instant immediately before the left front footfall (t_1 = 0) and concludes at the instant immediately before the next fall of the same foot. The motion is characterized by a system of fifteen constraint equations, 3.5 through 3.19, in the following variables: t_2, t_3, t_4, z_1, u_{zo}, d_f, d_h, θ_{x1}, θ_{y1}, ω_{xo}, ω_{yo}, i_{fx}, i_{hx}, i_{fz}, i_{hz}. Again, these equations were developed from the conservation of momentum across the instantaneous footfalls and the ballistic motion of the body between footfalls. All yaw of the trunk is assumed to occur between the footfalls of each leg-pair, so ω_{zo} = 0.

Equation 3.5 constrains the height of the mass center to be the same at the beginning and end of the stride cycle.

$$u_{zo}T - \frac{i_{fz}t_2 + i_{hz}t_3 + i_{hz}t_4}{m} + \frac{gT^2}{2} = 0. \tag{3.5}$$

Equations 3.6, 3.7, and 3.8 impose the steady-state motion constraints on the roll, pitch, and yaw angles, respectively.

$$\omega_{xo}T + \frac{bi_{fz}t_2 - bi_{hz}t_3 + bi_{hz}t_4}{I_x} = 0. \tag{3.6}$$

$$\omega_{yo}T + \frac{(z_2 i_{fx} + d_f i_{fz})t_2 + z_3 i_{hx} t_3 + z_4 i_{hx} t_4 - d_h i_{hz}(t_3 + t_4)}{I_y} = 0. \tag{3.7}$$

$$i_{hx}t_3 - i_{fx}t_2 - i_{hx}t_4 = 0. \tag{3.8}$$

Equations 3.9 and 3.10 constrain the longitudinal and vertical velocities, respectively, to be the same at the beginning and end of the stride cycle.

$$2i_{fx} + 2i_{hx} - DT = 0. \tag{3.9}$$

$$2i_{fz} + 2i_{hz} - mgT = 0. \tag{3.10}$$

Equation 3.11 imposes the steady-state motion constraint on the pitch angular velocity. The pairwise symmetry of the front and hind impulses trivially satisfies this same constraint for the roll and yaw angular velocities.

$$2d_h i_{hz} - (z_1 + z_2)i_{fx} - (z_3 + z_4)i_{hx} - 2d_f i_{fz} = 0. \tag{3.11}$$

Equations 3.12 through 3.15 constrain each leg to operate with an optimal working length at its footfall by relating the mass center height, pitch, and roll to the impulse magnitudes through the constraint that the impulse line of action passes through the shoulder/hip joint.

$$z_1 + b\theta_{x1} - a\theta_{y1} - \frac{L_o i_{fz}}{\sqrt{i_{fx}^2 + i_{fz}^2}} = 0. \tag{3.12}$$

$$z_2 - b\left[\theta_{x1} + \omega_{xo}t_2 + \frac{bi_{fz}t_2}{I_x}\right] - \frac{L_o i_{fz}}{\sqrt{i_{fx}^2 + i_{fz}^2}}$$
$$-a\left[\theta_{y1} + \omega_{yo}t_2 - \frac{z_1 i_{fx} t_2 + d_f i_{fz} t_2}{I_y}\right] = 0. \tag{3.13}$$

$$z_3 + b\left[\theta_{x1} + \omega_{xo}t_3 + \frac{bi_{fz}t_2}{I_x}\right] - \frac{L_o i_{hz}}{\sqrt{i_{hx}^2 + i_{hz}^2}}$$

$$+c\left[\theta_{y1} + \omega_{yo}t_3 + \frac{i_{fx}(z_2t_2 - z_1t_3 - z_2t_3) + d_f i_{fz}(t_2 - 2t_3)}{I_y}\right] = 0. \quad (3.14)$$

$$z_4 - b\left[\theta_{x1} + \omega_{xo}t_4 + \frac{bi_{fz}t_2 - bi_{hz}t_3 + bi_{hz}t_4}{I_x}\right] - \frac{L_o i_{hz}}{\sqrt{i_{hx}^2 + i_{hz}^2}} + c\theta_{y1} + c\omega_{yo}t_4$$

$$+c\left[\frac{i_{fx}(z_2t_2 - z_1t_4 - z_2t_4) + d_f i_{fz}(t_2 - 2t_4) + (z_3 i_{hx} - d_h i_{hz})(t_3 - t_4)}{I_y}\right] = 0. \quad (3.15)$$

Equations 3.16 and 3.17 express the longitudinal locations of the footfalls relative to the mass center in terms of the impulses and the working length of the legs. Again, these equations arise from the constraint that each impulse line of action passes through the shoulder/hip joint.

$$a - \frac{L_o i_{fx}}{\sqrt{i_{fx}^2 + i_{fz}^2}} - d_f = 0. \quad (3.16)$$

$$c + \frac{L_o i_{hx}}{\sqrt{i_{hx}^2 + i_{hz}^2}} - d_h = 0. \quad (3.17)$$

Equations 3.18 and 3.19 constrain the roll angles of the trunk to be equal in magnitude, but opposite in sign, at the footfalls of the two front legs and at the footfalls of the two hind legs.

$$2\theta_{x1} + \omega_{xo}t_2 + \frac{bi_{fz}t_2}{I_x} = 0. \quad (3.18)$$

$$2\theta_{x1} + \omega_{xo}t_3 + \omega_{xo}t_4 + \frac{2bi_{fz}t_2 - bi_{hz}t_3 + bi_{hz}t_4}{I_x} = 0. \quad (3.19)$$

The remaining model parameters are given by the following equations.

$$z_2 = z_1 + u_{zo}t_2 + \frac{i_{fz}t_2}{m} - \frac{gt_2^2}{2}. \quad (3.20)$$

$$z_3 = z_1 + u_{zo}t_3 + \frac{2i_{fz}t_3 - i_{fz}t_2}{m} - \frac{gt_3^2}{2}. \quad (3.21)$$

$$z_4 = z_1 + u_{zo}t_4 + \frac{2i_{fz}t_4 - i_{fz}t_2 - i_{hz}t_3 + i_{hz}t_4}{m} - \frac{gt_4^2}{2}. \quad (3.22)$$

$$u_{xo} = u_x + \frac{i_{fx}t_2 + i_{hx}t_3 + i_{hx}t_4}{Tm} - \frac{DT}{2m}. \tag{3.23}$$

Table 3.3 contains the solution to the system of Equations 3.5 through 3.19 at the trot-to-gallop transition speed and stride frequency with all quantities rounded to three decimal places. Figure 3.7 shows the position of the mass center in the vertical direction over the course of a single stride. The position of the mass center in the longitudinal direction at the beginning of the stride is taken to be zero.

The asymmetrical phasing of the legs is clearly seen both in the table and in the figure. As is typical of galloping [60], the separation of the footfalls of the two front legs is greater than that of the two hind legs. In time, the separation of the front footfalls is t_2, and in space,

Parameter	**Value**	**Units**
t_2	0.069	s
t_3	0.228	s
t_4	0.231	s
z_1	0.719	m
u_{zo}	-0.918	$\frac{m}{s}$
d_f	0.181	m
d_h	0.574	m
θ_{x1}	-0.118	rad
θ_{y1}	0.060	rad
ω_{xo}	-0.724	$\frac{rad}{s}$
ω_{yo}	2.015	$\frac{rad}{s}$
i_{fx}	-0.650	$N \cdot s$
i_{fz}	40.024	$N \cdot s$
i_{hx}	10.050	$N \cdot s$
i_{hz}	24.722	$N \cdot s$

Table 3.3: Transverse gallop solution at the trot-to-gallop transition speed, u_x = 3.28 $\frac{m}{s}$, and stride period, T = 0.40 s.

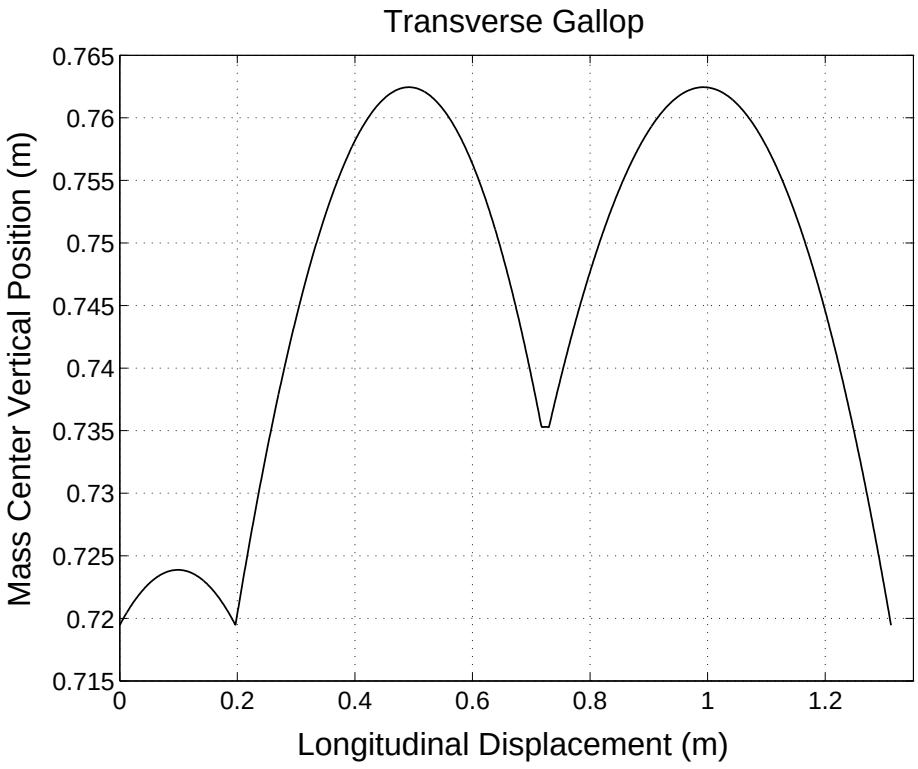

Figure 3.7: Vertical position of the mass center in a transverse gallop at the trot-to-gallop transition speed, u_x = 3.28 $\frac{m}{s}$, and stride period, T = 0.40 s.

the separation is the length of the first small parabolic trajectory in Figure 3.7. Similarly, the separation of the hind footfalls in time is t_4 - t_3 and in space, is the length of the very small parabolic trajectory between the two larger ones. The gathered flight phase, shown as the first large parabolic trajectory in Figure 3.7, has the longest duration, which is t_3 - t_2 = .159 s. The extended flight phase, though, shown as the second large parabolic trajectory, is almost as long. Its duration is T - t_4 = .169 s. Except near the highest speeds in galloping, the gathered flight phase is normally longer than the extended flight phase because the front legs provide more vertical thrust [46].

Table 3.3 shows that the vertical component of the front impulses is indeed larger than that of the hind impulses. This behavior stems from the forward distribution of mass in the model. The longitudinal component of the front impulses is negative, so the front legs counterintuitively act to retard forward motion. This phenomenon, though, is consistent with the force plate measurements of Bryant et al. [23] and Manter [76]. The hind legs normally provide most of the forward thrust while the net effect of the front footfalls can be to retard forward motion.

In terms of angular displacement, the largest occurs in pitch. Throughout one full stride, though, the magnitude of the pitch angle does not exceed 16^o, so the small angle approximation is reasonably valid. In fact, it is the asymmetry of the pitching motion that explains why the elevation of the mass center in Figure 3.7 is higher at the hind footfalls than it is at the front footfalls. Both the asymmetry of the footfalls and the pitching motion of the body contribute to the difference between the vertical displacement of the mass center in Figure 3.7 and that predicted in Figure 3.2.

3.4.2 Rotary Gallop

The footfall sequence for the rotary gallop is left front, right front, right hind, left hind, and the support diagram is shown in Figure 3.8. Again, a single stride begins at the instant immediately before the left front footfall (t_1 = 0) and concludes at the instant immediately

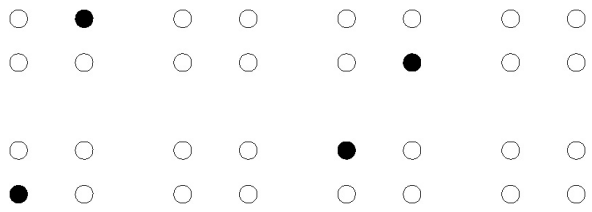

Figure 3.8: Support diagram of the rotary gallop.

before the next fall of the same foot. The motion is characterized by a system of fourteen constraint equations, 3.24 through 3.37, in the following variables: t_2, t_3, t_4, z_1, u_{zo}, d_f, d_h, θ_{x1}, θ_{y1}, ω_{yo}, i_{fx}, i_{hx}, i_{fz}, i_{hz}. All roll of the trunk is assumed to occur between the footfalls of each leg-pair, so ω_{xo} = 0.

$$u_{zo}T - \frac{i_{fz}t_2 + i_{hz}t_3 + i_{hz}t_4}{m} + \frac{gT^2}{2} = 0. \tag{3.24}$$

$$i_{fz}t_2 + i_{hz}t_3 - i_{hz}t_4 = 0. \tag{3.25}$$

$$\omega_{yo}T + \frac{(z_1 i_{fx} + d_f i_{fz})t_2 + (z_3 i_{hx} - d_h i_{hz})(t_3 + t_4)}{I_y} = 0. \tag{3.26}$$

$$2i_{fx} + 2i_{hx} - DT = 0. \tag{3.27}$$

$$2i_{fz} + 2i_{hz} - mgT = 0. \tag{3.28}$$

$$d_h i_{hz} - z_1 i_{fx} - z_3 i_{hx} - d_f i_{fz} = 0. \tag{3.29}$$

$$z_1 + b\theta_{x1} - a\theta_{y1} - \frac{L_o i_{fz}}{\sqrt{i_{fx}^2 + i_{fz}^2}} = 0. \tag{3.30}$$

$$z_1 - b\left[\theta_{x1} + \frac{b i_{fz} t_2}{I_x}\right] - a\left[\theta_{y1} + \omega_{yo}t_2 - \frac{z_1 i_{fx} t_2 + d_f i_{fz} t_2}{I_y}\right] - \frac{L_o i_{fz}}{\sqrt{i_{fx}^2 + i_{fz}^2}} = 0. \tag{3.31}$$

$$\begin{aligned} z_3 - b\left[\theta_{x1} + \frac{b i_{fz} t_2}{I_x}\right] - \frac{L_o i_{hz}}{\sqrt{i_{hx}^2 + i_{hz}^2}} \\ + c\left[\theta_{y1} + \omega_{yo}t_3 + \frac{(z_1 i_{fx} + d_f i_{fz})(t_2 - 2t_3)}{I_y}\right] = 0. \end{aligned} \tag{3.32}$$

$$\begin{aligned} z_3 + b\left[\theta_{x1} + \frac{b i_{fz} t_2 + b i_{hz} t_3 \ - b i_{hz} t_4}{I_x}\right] - \frac{L_o i_{hz}}{\sqrt{i_{hx}^2 + i_{hz}^2}} + c\theta_{y1} + c\omega_{yo}t_4 \\ + c\left[\frac{(z_1 i_{fx} + d_f i_{fz})(t_2 - 2t_4) + (z_3 i_{hx} - d_h i_{hz})(t_3 - t_4)}{I_y}\right] = 0. \end{aligned} \tag{3.33}$$

$$a - \frac{L_o i_{fx}}{\sqrt{i_{fx}^2 + i_{fz}^2}} - d_f = 0. \tag{3.34}$$

$$c + \frac{L_o i_{hx}}{\sqrt{i_{hx}^2 + i_{hz}^2}} - d_h = 0. \tag{3.35}$$

$$u_{zo} + \frac{i_{fz}}{m} - \frac{gt_2}{2} = 0. \tag{3.36}$$

$$u_{zo} + \frac{2i_{fz} + i_{hz}}{m} - \frac{g(t_3 + t_4)}{2} = 0. \tag{3.37}$$

All of these equations correspond directly to those characterizing the transverse gallop except Equations 3.36 and 3.37. Equation 3.36 constrains the mass center to be at the same height at each of the two front footfalls, and Equation 3.37 imposes the same constraint at the two hind footfalls. The parameters z_3 and u_{xo} are given by Equations 3.21 and 3.23, respectively, and,

$$\omega_{zo} = \frac{bi_{fx}t_2 + bi_{hx}t_3 - bi_{hx}t_4}{TI_z} = 0. \tag{3.38}$$

Table 3.4 contains the solution to this system at the trot-to-gallop transition speed and stride frequency with all quantities rounded to three decimal places. Figure 3.9 shows the

Parameter	**Value**	**Units**
t_2	0.041	s
t_3	0.191	s
t_4	0.249	s
z_1	0.689	m
u_{zo}	-0.956	$\frac{m}{s}$
d_f	0.277	m
d_h	0.659	m
θ_{x1}	-0.090	rad
θ_{y1}	0.057	rad
ω_{yo}	1.927	$\frac{rad}{s}$
i_{fx}	-5.919	$N \cdot s$
i_{fz}	38.113	$N \cdot s$
i_{hx}	15.319	$N \cdot s$
i_{hz}	26.633	$N \cdot s$

Table 3.4: Rotary gallop solution for the trot-to-gallop transition speed, u_x = 3.28 $\frac{m}{s}$ and stride period, T = 0.40 s.

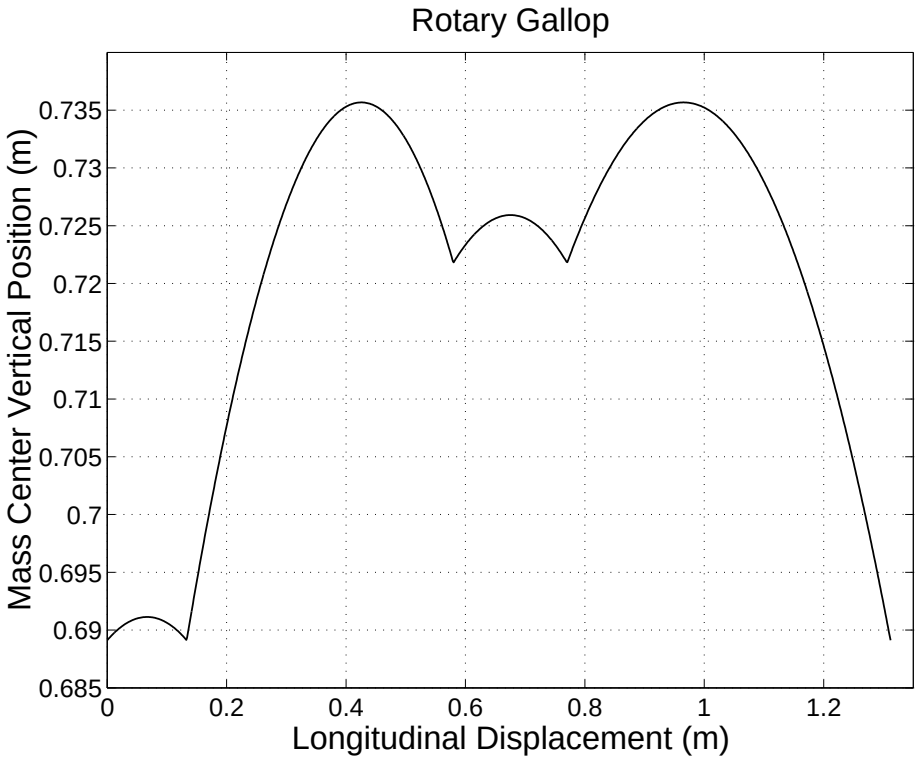

Figure 3.9: Vertical position of the mass center in a rotary gallop at the trot-to-gallop transition speed, u_x = 3.28 $\frac{m}{s}$, and stride period, T = 0.40 s.

position of the mass center in the vertical direction over the course of a single stride.

As expected, the solution for the rotary gallop is generally similar to that for the transverse gallop. The phasing of the legs is again asymmetrical. The vertical component of the front impulses is greater than that of the hind impulses, and the longitudinal component of the front impulses retards forward motion. In Figure 3.9, the elevation of the mass center is greater at the hind footfalls than it is at the front footfalls because the pitch motion is asymmetric.

The rotary gallop solution, though, differs from the transverse gallop solution in some more specific characteristics. The separation of the two front footfalls is slightly less than

Figure 3.10: Support diagram of the pronk.

the separation of the two hind footfalls. Both are smaller than the front footfall separation and greater than the hind footfall separation in the transverse gallop. Also, the gathered and extended flight phases are exactly equal in duration. The retarding effect of the front impulses is much greater than in the transverse gallop, and the maximum pitch angular displacement of 20^o is larger.

Despite the differences, the vertical displacement of the mass center in Figure 3.9 is quite similar to that of the transverse gallop in Figure 3.7 and quite different from that predicted in Figure 3.2.

3.4.3 Pronk

There is no footfall sequence for the pronk because all four footfalls take place at the beginning of the stride. The support diagram is shown in Figure 3.10, although this diagram represents two strides rather than just one. The equations for the pronk can be developed by setting t_2 = t_3 = t_4 = 0 in either the transverse or rotary gallop equations. The result is that the trunk does not rotate at all within a stride, so ω_{xo} = ω_{yo} = ω_{zo} = 0, and θ_{x1} = θ_{y1} = 0. With this simplification, the equations can be solved directly for the remaining model parameters.

$$i_{fx} = \frac{cDT}{2(a+c)}. \tag{3.39}$$

$$i_{hx} = \frac{aDT}{2(a+c)}. \tag{3.40}$$

$$i_{fz} = \frac{cmgT}{2(a+c)}. \tag{3.41}$$

$$i_{hz} = \frac{amgT}{2(a+c)}. \tag{3.42}$$

$$z_1 = \frac{mgL_o}{\sqrt{D^2 + m^2g^2}}. \tag{3.43}$$

$$u_{xo} = u_x - \frac{DT}{2m}. \tag{3.44}$$

$$u_{zo} = \frac{-gT}{2}. \tag{3.45}$$

Table 3.5 contains the values of these parameters at the trot-to-gallop transition speed and stride frequency with all quantities rounded to three decimal places. Figure 3.11 shows the position of the mass center in the vertical direction over the course of a single stride, which is a single ballistic trajectory in this case.

As in the two galloping gaits, the vertical component of the front impulses is greater than that of the hind impulses. While no force plate studies of pronking are available, the fact that the longitudinal component of the front impulses exceeds that of the hind impulses is inconsistent with force measurements for other gaits. This unusual distribution of the

Parameter	**Value**	**Units**
z_1	0.693	m
u_{zo}	-1.962	$\frac{m}{s}$
i_{fx}	6.071	$N \cdot s$
i_{fz}	41.815	$N \cdot s$
i_{hx}	3.329	$N \cdot s$
i_{hz}	22.931	$N \cdot s$

Table 3.5: Pronk solution for the trot-to-gallop transition speed, u_x = 3.28 $\frac{m}{s}$ and stride period, T = 0.40 s.

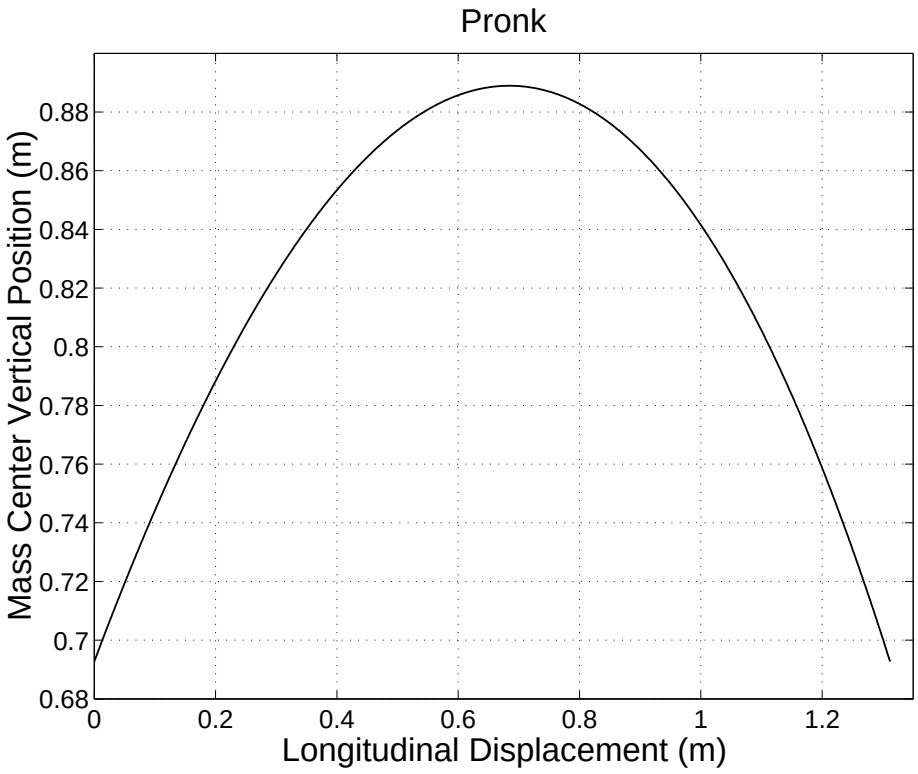

Figure 3.11: Vertical position of the mass center in a pronk at the trot-to-gallop transition speed, u_x = 3.28 $\frac{m}{s}$, and stride period, T = 0.40 s.

forward thrust balances the pitch moments on the body while the legs still operate at their optimal working length. It suggests that pronking animals may exert moments about their shoulders and hips in order to prevent pitch of their bodies. Since the body does not pitch at all in this model, though, the vertical displacement of the mass center in Figure 3.11 is exactly that predicted in Figure 3.2.

3.4.4 Trot

The footfall sequence for the trot is left front and right hind together, right front and left hind together, and the support diagram is shown in Figure 3.12. In order to meet the

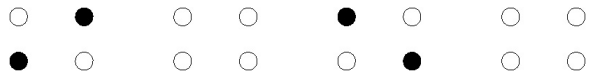

Figure 3.12: Support diagram of the trot.

steady-state motion constraints, the second pair of footfalls must occur out of phase with the first pair, or at time $\frac{T}{2}$. The transverse gallop sequence actually approaches a trot when $t_2 = t_3 = \frac{T}{2}$ and $t_4 = T$, because at time T, the next stride cycle is beginning. The much simpler motion of the trot, though, is characterized by a system of only five constraint equations, 3.46 through 3.50, in the following variables: z_1, i_{fx}, i_{hx}, i_{fz}, i_{hz}. Since the trunk undergoes no pitching motion in the trot, both θ_{y1} and ω_{yo} are assumed to be zero.

$$2i_{fx} + 2i_{hx} - DT = 0. \tag{3.46}$$

$$2i_{fz} + 2i_{hz} - mgT = 0. \tag{3.47}$$

$$ci_{hz} - ai_{fz} + \frac{L_o i_{fx} i_{fz}}{\sqrt{i_{fx}^2 + i_{fz}^2}} + \frac{L_o i_{hx} i_{hz}}{\sqrt{i_{hx}^2 + i_{hz}^2}} - \frac{z_1 DT}{2} = 0. \tag{3.48}$$

$$z_1 + \frac{b^2 T(i_{hz} - i_{fz})}{8I_x} - \frac{L_o i_{fz}}{\sqrt{i_{fx}^2 + i_{fz}^2}} = 0. \tag{3.49}$$

$$z_1 + \frac{b^2 T(i_{fz} - i_{hz})}{8I_x} - \frac{L_o i_{hz}}{\sqrt{i_{hx}^2 + i_{hz}^2}} = 0. \tag{3.50}$$

The remaining model parameters are given by the following equations.

$$u_{xo} = u_x - \frac{DT}{4m}. \tag{3.51}$$

$$u_{zo} = \frac{-gT}{4}. \tag{3.52}$$

$$\omega_{xo} = \frac{b(i_{hz} - i_{fz})}{2I_x}. \tag{3.53}$$

$$\omega_{zo} = \frac{b(i_{fx} - i_{hx})}{2I_z}. \tag{3.54}$$

$$\theta_{x1} = \frac{bT(i_{hz} - i_{fz})}{8I_x}. \tag{3.55}$$

Table 3.6 contains the solution to this system at the trot-to-gallop transition speed and stride frequency with all quantities rounded to three decimal places. Figure 3.13 shows the position of the mass center in the vertical direction over the course of a single stride, which in this case is two equal ballistic trajectories.

As in all three preceding gaits, the vertical component of the front impulses is larger than that of the hind impulses. Even more so than in pronking, though, the front legs provide the forward thrust. Again, this is opposite of the behavior observed in animals, indicating that moments exerted about the shoulders and hips could play an important role in balancing body rotation. The discussion in Section 3.3 about the minimum level of drag for which trotting solutions are found addresses this same issue. It is highlighted here because the body rolls by as much as 6^o in each direction, and very little roll is observed in

Parameter	**Value**	**Units**
z_1	0.691	m
u_{zo}	-0.981	$\frac{m}{s}$
d_f	0.016	m
d_h	0.309	m
θ_{x1}	-0.108	rad
ω_{xo}	-1.075	$\frac{rad}{s}$
i_{fx}	9.407	$N \cdot s$
i_{fz}	41.646	$N \cdot s$
i_{hx}	-.007	$N \cdot s$
i_{hz}	23.100	$N \cdot s$

Table 3.6: Trot solution for the trot-to-gallop transition speed, u_x = 3.28 $\frac{m}{s}$ and stride period, T = 0.40 s.

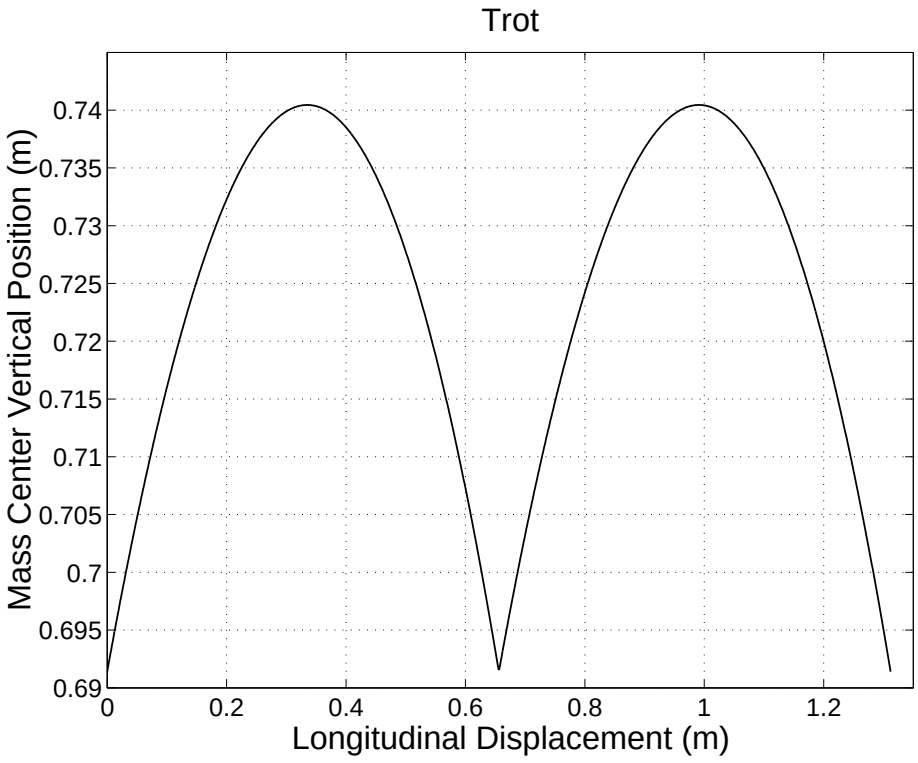

Figure 3.13: Vertical position of the mass center in a trot at the trot-to-gallop transition speed, u_x = 3.28 $\frac{m}{s}$, and stride period, T = 0.40 s.

trotting animals. The body does not pitch at all, though, so the vertical displacement of the mass center in Figure 3.13 is equivalent to that predicted in Figure 3.2.

If the body's mass distribution is symmetric, no difficulty arises in solving the trotting equations for any level of drag. In this case, $a = c$, $i_{fx} = i_{hx} = \frac{DT}{4}$, $i_{fz} = i_{hz} = \frac{mgT}{4}$, and there is no rotation of the body. All of the remaining model parameters can also be found directly. A symmetric mass distribution, though, does not accurately model a biological quadruped.

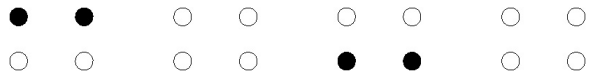

Figure 3.14: Support diagram of the pace.

3.4.5 Pace

The footfall sequence for the pace is left front and left hind together, right front and right hind together, and the support diagram is shown in Figure 3.14. As in the trot, the second pair of footfalls must occur out of phase with the first pair, and the motion is characterized by a system of five constraint equations, 3.56 through 3.60. The variables are again: z_1, i_{fx}, i_{hx}, i_{fz}, i_{hz}, and due to the lack of pitching motion, θ_{y1} and ω_{yo} are again assumed to be zero. Unlike the trot, though, it is the rotary gallop sequence that approaches the pace when $t_2 = t_3 = \frac{T}{2}$ and $t_4 = T$.

$$2i_{fx} + 2i_{hx} - DT = 0. \tag{3.56}$$

$$2i_{fz} + 2i_{hz} - mgT = 0. \tag{3.57}$$

$$ci_{hz} - ai_{fz} + \frac{L_o i_{fx} i_{fz}}{\sqrt{i_{fx}^2 + i_{fz}^2}} + \frac{L_o i_{hx} i_{hz}}{\sqrt{i_{hx}^2 + i_{hz}^2}} - \frac{z_1 DT}{2} = 0. \tag{3.58}$$

$$z_1 - \frac{b^2 mgT^2}{16 I_x} - \frac{L_o i_{fz}}{\sqrt{i_{fx}^2 + i_{fz}^2}} = 0. \tag{3.59}$$

$$i_{fx}^2 i_{hz}^2 - i_{hx}^2 i_{fz}^2 = 0. \tag{3.60}$$

The remaining model parameters are given by the following equations.

$$u_{xo} = u_x - \frac{DT}{4m}. \tag{3.61}$$

$$u_{zo} = \frac{-gT}{4}. \tag{3.62}$$

$$\omega_{xo} = \frac{-bmgT}{4I_x}. \tag{3.63}$$

$$\omega_{zo} = \frac{bDT}{4I_z}. \tag{3.64}$$

$$\theta_{x1} = \frac{-bmgT^2}{16I_x}. \tag{3.65}$$

Table 3.7 contains the solution to this system at the trot-to-gallop transition speed and stride frequency with all quantities rounded to three decimal places. Figure 3.15 shows the position of the mass center in the vertical direction over the course of a single stride, which as in the trot, is two equal ballistic trajectories.

The vertical components of the impulses are similar to those in the other gaits, and the longitudinal components are at least more consistent with behavior of animals than those in trotting. The front legs produce more of the forward thrust, but the hind legs do contribute a significant portion. Because the legs operate in lateral pairs, the roll motion of the body is much greater than that observed in the other gaits. In fact, the maximum roll angle is 21.5^o,

Parameter	**Value**	**Units**
z_1	0.723	m
u_{zo}	-0.981	$\frac{m}{s}$
d_f	0.069	m
d_h	0.411	m
θ_{x1}	-0.375	rad
ω_{xo}	-3.753	$\frac{rad}{s}$
i_{fx}	5.985	$N \cdot s$
i_{fz}	41.227	$N \cdot s$
i_{hx}	3.415	$N \cdot s$
i_{hz}	23.519	$N \cdot s$

Table 3.7: Pace solution for the trot-to-gallop transition speed, u_x = 3.28 $\frac{m}{s}$ and stride period, T = 0.40 s.

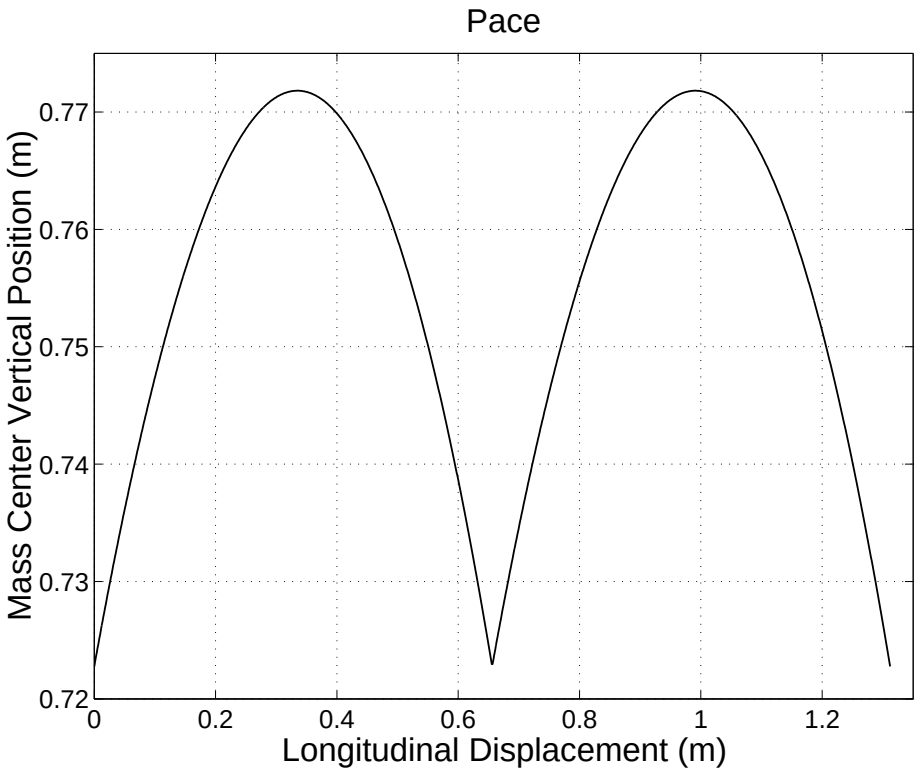

Figure 3.15: Vertical position of the mass center in a pace at the trot-to-gallop transition speed, u_x = 3.28 $\frac{m}{s}$, and stride period, T = 0.40 s.

so the small angle approximation is less valid. Pacing animals typically do not experience such large roll motions, so again, they may be using shoulder and hip torque to reduce their body rotation. The vertical displacement of the mass center in pacing, though, is exactly the same as that in trotting.

3.4.6 Bound

The footfall sequence for the bound is left front and right front together, left hind and right hind together, and the support diagram is shown in Figure 3.16. Unlike the trot and pace, the footfalls are not necessarily equally spaced within the stride. Thus, the bounding

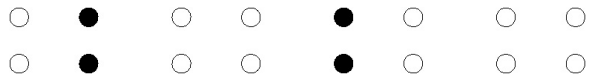

Figure 3.16: Support diagram of the bound.

equations result from setting t_2 = 0 and $t_3 = t_4$ in either the transverse or rotary gallop equations. This yields a planar gait in which the trunk does not yaw or roll, so θ_{x1} = 0, and $\omega_{xo} = \omega_{zo}$ = 0. In this case, the simplified motion creates some difficulty because too few non-trivial equations remain to solve for all of the system parameters. The motion is characterized by only nine equations, 3.66 through 3.74, in the following eleven variables: z_1, θ_{y1}, u_{zo}, ω_{yo}, i_{fx}, i_{hx}, i_{fz}, i_{hz}, t_2, d_f, d_h.

$$u_{zo}T - \frac{2i_{hz}t_2}{m} + \frac{gT^2}{2} = 0. \tag{3.66}$$

$$\omega_{yo}T + \frac{2z_1 i_{hx}t_2}{I_y} + \frac{2u_{zo}i_{hx}t_2^2}{I_y} + \frac{4i_{hx}i_{fz}t_2^2}{mI_y} - \frac{gi_{hx}t_2^3}{I_y} - \frac{2d_h i_{hz}t_2}{I_y} = 0. \tag{3.67}$$

$$2i_{fx} + 2i_{hx} - DT = 0. \tag{3.68}$$

$$2i_{fz} + 2i_{hz} - mgT = 0. \tag{3.69}$$

$$d_h i_{hz} - z_1 i_{fx} - z_1 i_{hx} - u_{zo}t_2 i_{hx} - \frac{2i_{hx}i_{fz}t_2}{m} + \frac{gi_{hx}t_2^2}{2} - d_f i_{fz} = 0. \tag{3.70}$$

$$z_1 - a\theta_{y1} - \frac{L_o i_{fz}}{\sqrt{i_{fx}^2 + i_{fz}^2}} = 0. \tag{3.71}$$

$$z_1 + u_{zo}t_2 + \frac{2i_{fz}t_2}{m} - \frac{gt_2^2}{2} + c\left[\theta_{y1} + \omega_{yo}t_2 - \frac{2z_1 i_{fx}t_2 + 2d_f i_{fz}t_2}{I_y}\right] - \frac{L_o i_{hz}}{\sqrt{i_{hx}^2 + i_{hz}^2}} = 0. \tag{3.72}$$

$$a - \frac{L_o i_{fx}}{\sqrt{i_{fx}^2 + i_{fz}^2}} - d_f = 0. \tag{3.73}$$

$$c + \frac{L_o i_{hx}}{\sqrt{i_{hx}^2 + i_{hz}^2}} - d_h = 0. \tag{3.74}$$

The initial longitudinal velocity is given by,

$$u_{xo} = u_x + \frac{2i_{hx}t_2}{Tm} - \frac{DT}{2m}. \tag{3.75}$$

In order to generate solutions for bounding, the magnitudes of the front impulses are simply assumed to have values similar to those found in the transverse and rotary gallops for the same stride period. Specifying the magnitudes of i_{fx} and i_{fz} reduces the number of variables to nine, rendering the system solvable. Since there is some flexibility in selecting these values, an effort was made to find the values that yield the smallest vertical oscillations of the mass center. These values correspond to a gait with two ballistic trajectories of equal duration.

Table 3.8 contains the solution to this system at the trot-to-gallop transition speed and stride frequency with all quantities rounded to three decimal places. Figure 3.17 shows the

Parameter	**Value**	**Units**
t_2	0.200	s
z_1	0.718	m
u_{zo}	-1.225	$\frac{m}{s}$
d_f	0.122	m
d_h	0.493	m
θ_{y1}	0.116	rad
ω_{yo}	2.057	$\frac{rad}{s}$
i_{fx}	2.803	$N \cdot s$
i_{fz}	40.443	$N \cdot s$
i_{hx}	6.597	$N \cdot s$
i_{hz}	24.303	$N \cdot s$

Table 3.8: Bound solution for the trot-to-gallop transition speed, u_x = 3.28 $\frac{m}{s}$ and stride period, T = 0.40 s.

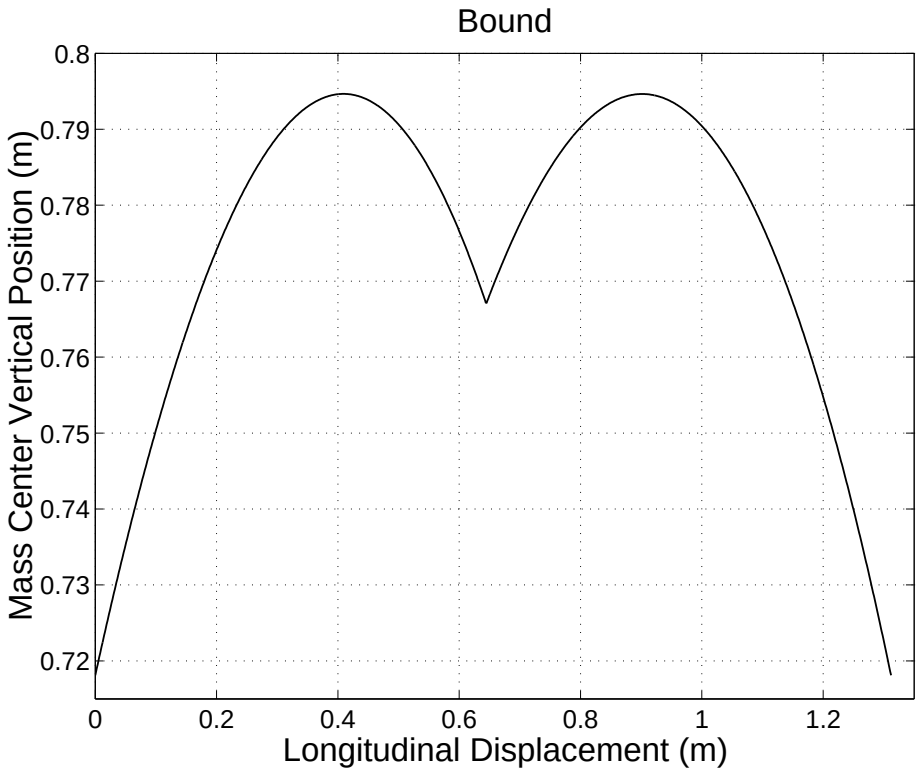

Figure 3.17: Vertical position of the mass center in a bound at the trot-to-gallop transition speed, u_x = 3.28 $\frac{m}{s}$, and stride period, T = 0.40 s.

position of the mass center in the vertical direction over the course of a single stride.

This symmetrical bound has equal gathered and extended flight phases because of the selected values for i_{fx} and i_{fz}. The solution, though, matches the behavior of animals in that the hind legs provide more of the forward thrust than do the front legs. The body's pitch angle is also reasonable, as it does not exceed 17^o. Like the two galloping solutions, the elevation of the mass center in Figure 3.17 is greater at the hind footfalls than it is at the front footfalls due to the asymmetrical pitch motion. Since the footfalls are symmetric, it is the asymmetry in pitch alone that causes the vertical displacement in Figure 3.17 to differ from that predicted in Figure 3.2.

Figure 3.18: Support diagram of the half-bound.

3.4.7 Half-Bound

The half-bound footfall sequence is left front, right front, left hind and right hind together, and the support diagram is shown in Figure 3.18. The half-bound equations result from setting t_3 = t_4 in either the transverse or rotary gallop equations. Unlike the bound, the half-bound is not planar because the phase difference between the front legs causes the trunk to roll. As in the transverse gallop, though, ω_{zo} is assumed to be zero, and as a result, i_{fx} = 0 and i_{hx} = $\frac{DT}{2}$. The motion is characterized by a system of nine constraint equations, 3.76 through 3.84, in the following variables: t_2, t_3, z_1, u_{zo}, d_h, θ_{y1}, ω_{yo}, i_{fz}, i_{hz}.

$$u_{zo}T - \frac{i_{fz}t_2 + 2i_{hz}t_3}{m} + \frac{gT^2}{2} = 0. \tag{3.76}$$

$$\omega_{yo}T + \frac{z_1 DTt_3}{I_y} + \frac{u_{zo}DTt_3^2}{I_y} + \frac{i_{fz}DTt_3(2t_3 - t_2)}{mI_y} - \frac{gDTt_3^3}{2I_y} + \frac{ai_{fz}t_2}{I_y} - \frac{2d_h i_{hz}t_3}{I_y} = 0. \tag{3.77}$$

$$2i_{fz} + 2i_{hz} - mgT = 0. \tag{3.78}$$

$$d_h i_{hz} - \frac{z_1 DT}{2} - \frac{u_{zo}DTt_3}{2} + \frac{i_{fz}DTt_2}{2m} - \frac{i_{fz}DTt_3}{m} + \frac{gDTt_3^2}{4} - ai_{fz} = 0. \tag{3.79}$$

$$z_1 + \frac{b^2 i_{fz}t_2^2 - b^2 i_{fz}t_2t_3}{TI_x} - a\theta_{y1} - L_o = 0. \tag{3.80}$$

$$u_{zo} + \frac{i_{fz}}{m} - \frac{gt_2}{2} - a\omega_{yo} + \frac{a^2 i_{fz}}{I_y} = 0. \tag{3.81}$$

$$z_1 + u_{zo}t_3 + \frac{2i_{fz}t_3 - i_{fz}t_2}{m} - \frac{gt_3^2}{2} - \frac{L_o i_{hz}}{\sqrt{\frac{D^2T^2}{4} + i_{hz}^2}} + c\left[\theta_{y1} + \omega_{yo}t_3 + \frac{ai_{fz}t_2 - 2ai_{fz}t_3}{I_y}\right] = 0. \tag{3.82}$$

$$c + \frac{L_o DT}{\sqrt{D^2T^2 + 4i_{hz}^2}} - d_h = 0. \tag{3.83}$$

$$T + t_2 - 2t_3 = 0. \tag{3.84}$$

The remaining model parameters are given by the following equations.

$$\omega_{xo} = \frac{-bi_{fz}t_2}{TI_x}. \tag{3.85}$$

$$\theta_{x1} = \frac{bi_{fz}t_2^2 - bi_{fz}t_2t_3}{TI_x}. \tag{3.86}$$

$$u_{xo} = u_x + \frac{Dt_3}{m} - \frac{DT}{2m}. \tag{3.87}$$

Table 3.9 contains the solution to this system at the trot-to-gallop transition speed and stride frequency with all quantities rounded to three decimal places. Figure 3.19 shows the position of the mass center in the vertical direction over the course of a single stride.

Parameter	**Value**	**Units**
t_2	0.107	s
t_3	0.254	s
z_1	0.727	m
u_{zo}	-0.699	$\frac{m}{s}$
d_f	0.122	m
d_h	0.493	m
θ_{x1}	-0.184	rad
θ_{y1}	0.070	rad
ω_{xo}	-1.256	$\frac{rad}{s}$
ω_{yo}	2.039	$\frac{rad}{s}$
i_{fz}	40.426	$N \cdot s$
i_{hz}	24.320	$N \cdot s$

Table 3.9: Half-bound solution for the trot-to-gallop transition speed, u_x = 3.28 $\frac{m}{s}$ and stride period, T = 0.40 s.

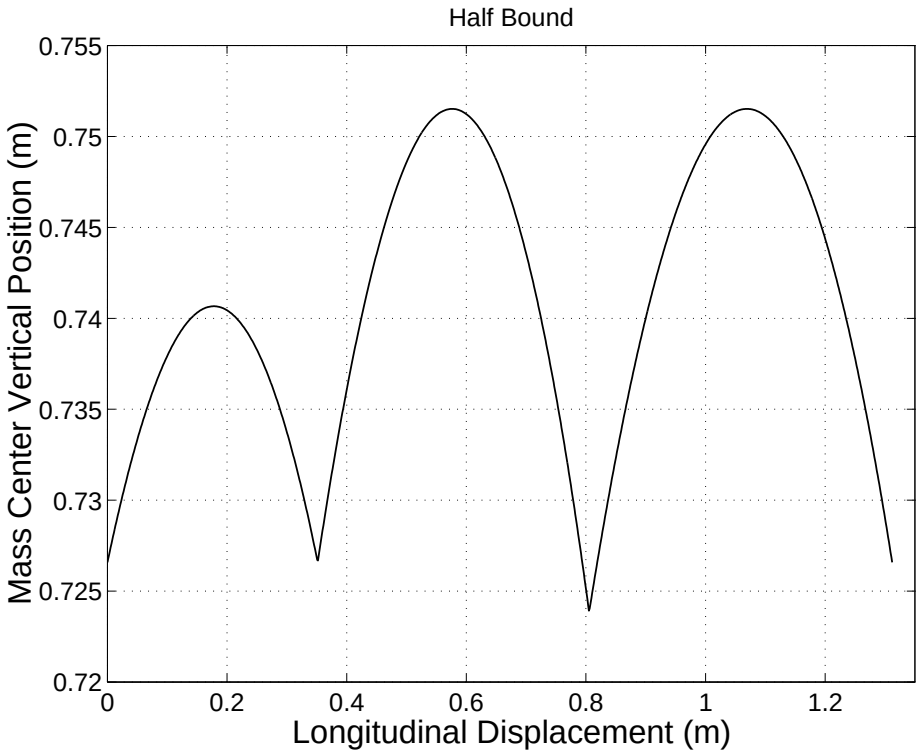

Figure 3.19: Vertical position of the mass center in a half-bound at the trot-to-gallop transition speed, u_x = 3.28 $\frac{m}{s}$, and stride period, T = 0.40 s.

The phasing of the legs in the half-bound is clearly asymmetrical. While the gathered and extended flight phases are equal in duration, the separation of the two front footfalls is smaller than either of them. This separation, however, may be somewhat larger than that typically observed in animals that use the half-bound. Both the longitudinal and the vertical components of the impulses have values consistent with animal behavior, and the pitch angle of the body does not exceed 13^o. Unlike the preceding gaits, the elevation of the mass center is actually lower at the hind footfalls than it is at the front footfalls due to the asymmetrical pitch motion. Three-beat gaits like the half-bound are not addressed in Section 3.2 or in Figure 3.2, but a symmetrical phasing of the legs would yield three equal

Figure 3.20: Support diagram of the canter.

ballistic trajectories. The trajectories in Figure 3.19 are close to this, but the asymmetrical footfall phasing and pitch motion create some differences.

3.4.8 Canter

The footfall sequence for the canter is left front and right hind together, right front, left hind, and the support diagram is shown in Figure 3.20. The transverse gallop sequence approaches a canter when t_4 = T, because at time T, the next stride cycle is beginning. The motion of the canter is characterized by a system of thirteen constraint equations, 3.88 through 3.100, in the following variables: t_2, t_3, z_1, u_{zo}, d_f, d_h, θ_{x1}, ω_{xo}, ω_{yo}, i_{fx}, i_{hx}, i_{fz}, i_{hz}. As in the transverse gallop, ω_{zo} is assumed to be zero, and like the trot, θ_{y1} is assumed to be zero. These assumptions highlight the fact that the canter is typically a transitional gait between the trot and transverse gallop.

$$u_{zo}T - \frac{i_{fz}t_2 + i_{hz}t_3}{m} + \frac{gT^2}{2} = 0. \tag{3.88}$$

$$\omega_{xo}T + \frac{bi_{fz}t_2 - bi_{hz}t_3}{I_x} = 0. \tag{3.89}$$

$$\omega_{yo}T + \frac{z_2 i_{fx}t_2 + z_3 i_{hx}t_3 + d_f i_{fz}t_2 - d_h i_{hz}t_3}{Iy} = 0. \tag{3.90}$$

$$i_{fx}t_2 - i_{hx}t_3 = 0. \tag{3.91}$$

$$2i_{fx} + 2i_{hx} - DT = 0. \tag{3.92}$$

$$2i_{fz} + 2i_{hz} - mgT = 0. \tag{3.93}$$

$$2d_h i_{hz} - (z_1 + z_2)i_{fx} - (z_1 + z_3)i_{hx} - 2d_f i_{fz} = 0. \tag{3.94}$$

$$z_1 + b\theta_{x1} - \frac{L_o i_{fz}}{\sqrt{i_{fx}^2 + i_{fz}^2}} = 0. \tag{3.95}$$

$$z_1 - b\theta_{x1} - \frac{L_o i_{hz}}{\sqrt{i_{hx}^2 + i_{hz}^2}} = 0. \tag{3.96}$$

$$\begin{aligned} z_2 - b\left[\theta_{x1} + \omega_{xo}t_2 + \frac{bi_{fz}t_2 - bi_{hz}t_2}{I_x}\right] - \frac{L_o i_{fz}}{\sqrt{i_{fx}^2 + i_{fz}^2}} \\ -at_2\left[\omega_{yo} + \frac{d_h i_{hz} - z_1 i_{fx} - z_1 i_{hx} - d_f i_{fz}}{I_y}\right] = 0. \end{aligned} \tag{3.97}$$

$$\begin{aligned} z_3 + b\left[\theta_{x1} + \omega_{xo}t_3 + \frac{bi_{fz}t_2 - bi_{hz}t_3}{I_x}\right] - \frac{L_o i_{hz}}{\sqrt{i_{hx}^2 + i_{hz}^2}} \\ +c\left[\omega_{yo}t_3 + \frac{i_{fx}(z_2t_2 - z_1t_3 - z_2t_3) + (d_h i_{hz} - z_1 i_{hx})t_3 + d_f i_{fz}(t_2 - 2t_3)}{I_y}\right] = 0. \end{aligned} \tag{3.98}$$

$$a - \frac{L_o i_{fx}}{\sqrt{i_{fx}^2 + i_{fz}^2}} - d_f = 0. \tag{3.99}$$

$$c + \frac{L_o i_{hx}}{\sqrt{i_{hx}^2 + i_{hz}^2}} - d_h = 0. \tag{3.100}$$

The remaining model parameters are given by the following equations.

$$z_2 = z_1 + u_{zo}t_2 + \frac{i_{fz}t_2 + i_{hz}t_2}{m} - \frac{gt_2^2}{2}. \tag{3.101}$$

$$z_3 = z_1 + u_{zo}t_3 + \frac{2i_{fz}t_3 - i_{fz}t_2 + i_{hz}t_3}{m} - \frac{gt_3^2}{2}. \tag{3.102}$$

$$u_{xo} = u_x + \frac{i_{fx}t_2 + i_{hx}t_3}{Tm} - \frac{DT}{2m}. \tag{3.103}$$

Table 3.10 contains a sample solution to this system for the trot-to-gallop transition speed and stride frequency with all quantities rounded to three decimal places. Figure 3.21 shows the displacement of the mass center in the vertical direction over the course of a single stride.

Like galloping, the phasing of the legs in cantering is asymmetrical. The separation of the two front footfalls is much larger than that of the two hind footfalls. In fact, the two

Parameter	Value	Units
t_2	0.141	s
t_3	0.381	s
z_1	0.693	m
u_{zo}	-0.844	$\frac{m}{s}$
d_f	0.055	m
d_h	0.385	m
θ_{x1}	-0.034	rad
ω_{xo}	0.899	$\frac{rad}{s}$
ω_{yo}	1.265	$\frac{rad}{s}$
i_{fx}	6.861	$N \cdot s$
i_{fz}	41.324	$N \cdot s$
i_{hx}	2.539	$N \cdot s$
i_{hz}	23.422	$N \cdot s$

Table 3.10: Canter solution for the trot-to-gallop transition speed, u_x = 3.28 $\frac{m}{s}$ and stride period, T = 0.40 s.

hind footfalls occur so close together that the extended flight phase is very short. This is typical of cantering animals. In fact, the canter is normally characterized by a single flight phase after the second front foot is lifted. The largest parabolic trajectory in Figure 3.21 shows that the gathered flight phase is indeed the longest in the stride. As in the half-bound, the separation of the two front footfalls may be unnaturally large in this solution.

While the vertical components of the impulses are consistent with animal behavior, the longitudinal components are more similar to those seen in the trot and pronk models. The roll angular displacement of the body is also rather large, as it exceeds 22^o. These results again indicate that shoulder and hip torque are likely important in balancing the body rotation in cantering.

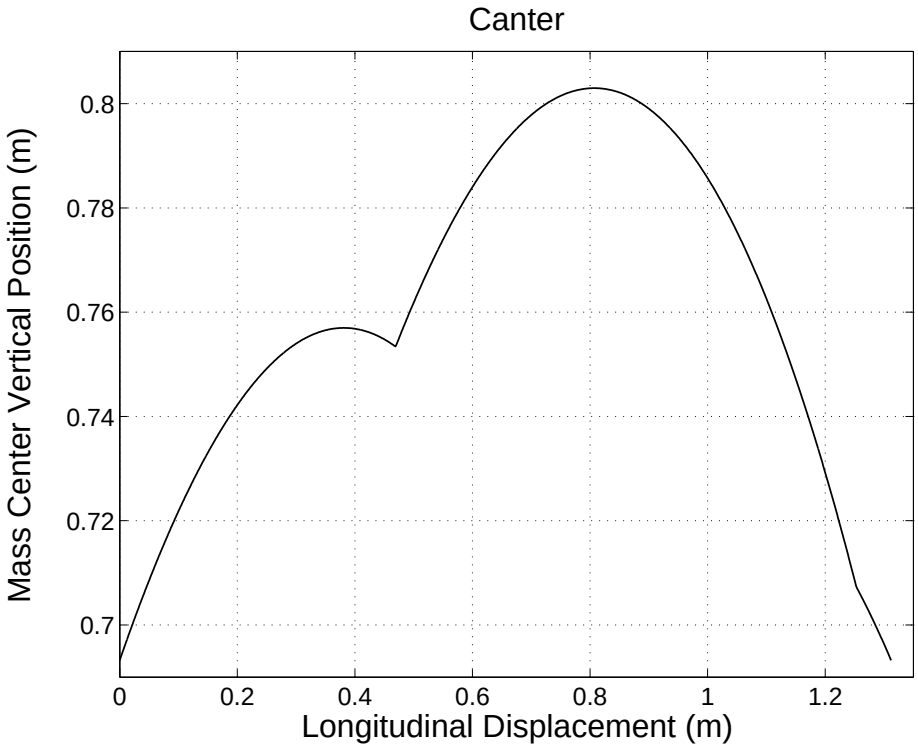

Figure 3.21: Vertical position of the mass center in a canter at the trot-to-gallop transition speed, u_x = 3.28 $\frac{m}{s}$, and stride period, T = 0.40 s.

The vertical displacement of the mass center in Figure 3.21 is much larger than that of the half-bound in Figure 3.19 and that of a symmetrical three-beat gait. This is due to the asymmetrical phasing of the legs and the asymmetrical pitch motion. Unlike most of the other gaits, the elevation of the mass center is much higher at the single front footfall than it is at the single hind footfall.

3.4.9 Other Sequences

The preceding sections address all of the dynamic quadrupedal gaits observed in the biological world that can be reasonably addressed with this model. The model could be

extended to any possible sequence of footfalls, but the results would not be meaningful for comparing the vertical displacements of the mass center in locomotion with other gaits.

In the pronk, all four legs operate in unison. No dynamic gait exists in which three of the legs operate together, alternating with one leg that operates individually, so no such gait is presented. In some slow walking gaits, three legs support the body while a single leg is in the transfer phase, but such gaits do not include the flight phases that characterize this model. The trot, pace, and bound comprise all combinations of the legs operating in pairs. The transverse and rotary gallops represent the only meaningful sequences of the legs operating individually because alternating use of individual front and hind legs can only be found in walking gaits.

The half-bound and the canter are gaits in which two legs operate as a pair while the other two operate individually. The crutch walk is another such gait in which the two front legs are in phase while the two hind legs are slightly out phase with each other. This gait, however, has only been observed in primates when they switch from a bipedal to a quadrupedal gait [59]. Since primate body structure and locomotion are vastly different from those of purely quadrupedal mammals that form the basis of the present model, the crutch-walk was not investigated. Other possible sequences involving a single pair of legs operating together were not considered because they have never been observed in the biological world. One results from a lateral pair of legs operating in phase rather than a diagonal pair as in the canter. Another is characterized by a hind footfall, rather than a front footfall, following the paired support of the legs in a canter-like gait.

3.5 Results

Since the pronk does not involve pitch motion of the body, the vertical displacements of the mass center calculated from the equations in Section 3.4.3 exactly match those predicted by Equation 3.2. Similarly, the vertical displacements in trotting and pacing, calculated from the equations in Sections 3.4.4 and 3.4.5, exactly match those predicted by Equation 3.3. The vertical displacements in the bound are greater than those predicted by Equation 3.3 because the pitch motion of the body is asymmetrical. In all of the other gaits, asymmetrical pitch motion and asymmetrical footfall phasing contribute to differences from the ideal behavior discussed in Section 3.2.

Table 3.11 lists the vertical displacements of the mass center in each gait for three speed and stride period combinations. The table compares the results from the "simple" model in Section 3.2 that assumes symmetrical footfall phasing with the results of the "full" model that solves for the phasing with the constraints that the legs operate at their optimal working length. The gaits are listed top to bottom in order of decreasing vertical displacement of the mass center.

As expected, the vertical displacement is dramatically larger in the pronk than it is in any of the other gaits. This explains, at least in part, why very few animals use the pronk and why no animals use it consistently to cover significant distances at reasonable speeds.

Since the canter is normally a transitional gait between the trot and gallop, its vertical displacements might be expected to fall somewhere between those of these other two gaits. The rather large cantering displacements in Table 3.11, however, are not inconsistent with animal behavior. Minetti et al. [88] measured larger vertical oscillations in horses when they cantered than when they trotted. The magnitude of the displacements for this model

	Preferred Trotting Stride Period .47 s		Trot-to-Gallop Transition Stride Period .40 s		Preferred Galloping Stride Period .39 s	
	simple model displ. (mm)	full model displ. (mm)	simple model displ. (mm)	full model displ. (mm)	simple model displ. (mm)	full model displ. (mm)
Pronk	271	271	196	196	187	187
Canter	30	164	22	110	21	103
Bound	68	105	49	77	47	74
Pace	68	68	49	49	47	47
Trot	68	68	49	49	47	47
Rotary gallop	17	65	12	47	12	44
Transverse gallop	17	59	12	43	12	41
Half-bound	30	41	22	28	21	26

Table 3.11: Vertical displacement of the mass center in millimeters for all modeled gaits. The simple models, discussed in Section 3.2 assume symmetrical phasing of the legs and neglect body rotation. The full models of each gait are characterized by the systems of equations in Sections 3.4.1 - 3.4.8.

may be somewhat larger than would be expected because of the relatively large phase difference between the front legs. Still, the general trend of the results matches the behavior of animals.

Because the body pitches in the bound, its vertical displacements are expected to be larger than those of the trot even if the footfalls are symmetrical. Furthermore, the bound is simply a gallop without a phase shift in the front and hind leg-pairs. Its vertical displacements should be larger than those of the gallop because the separation of the supporting legs smoothes out the motion of the mass center. Since the half-bound is something of a

compromise between a bound and a gallop, its vertical displacements are expected to fall in between those of these two gaits. The surprisingly small half-bounding displacements in Table 3.11 result from the unnaturally large phase difference calculated for the two front legs.

The pace and the trot are very similar gaits, so it is reasonable for their vertical displacements to be identical. The transverse and rotary gallops are also very similar, so little to no difference is expected in the vertical displacements of these two gaits. In Table 3.11, the corresponding values are very close, and the fact that animals normally prefer one or the other precludes drawing any conclusions from the slightly lower values in the transverse gallop.

The most important result presented in Table 3.11 is that galloping requires smaller vertical oscillations of the mass center than trotting does even though the footfall phasing is asymmetrical. For all three stride periods, the vertical displacement in transverse galloping is more than 12% smaller than in trotting. Figure 3.22 shows the trajectory of the mass center in the pronk, trot, and transverse gallop at the trot-to-gallop transition speed and stride frequency. When compared to Figure 3.2, this figure highlights the effect of the asymmetrical footfall phasing on the vertical displacement of the mass center in galloping. It also reveals that while in trotting the footfalls all occur after a fall from the maximum elevation, in galloping, only the touchdown of the first front foot takes place after a fall through the maximum height. If impact losses at the footfalls are of primary concern, this presents a possible advantage of galloping even beyond its smaller vertical displacements. The vertical velocity of the mass center at each footfall is significantly less in galloping than in trotting, which would be one explanation for why bone strain drops at the trot-to-gallop transition.

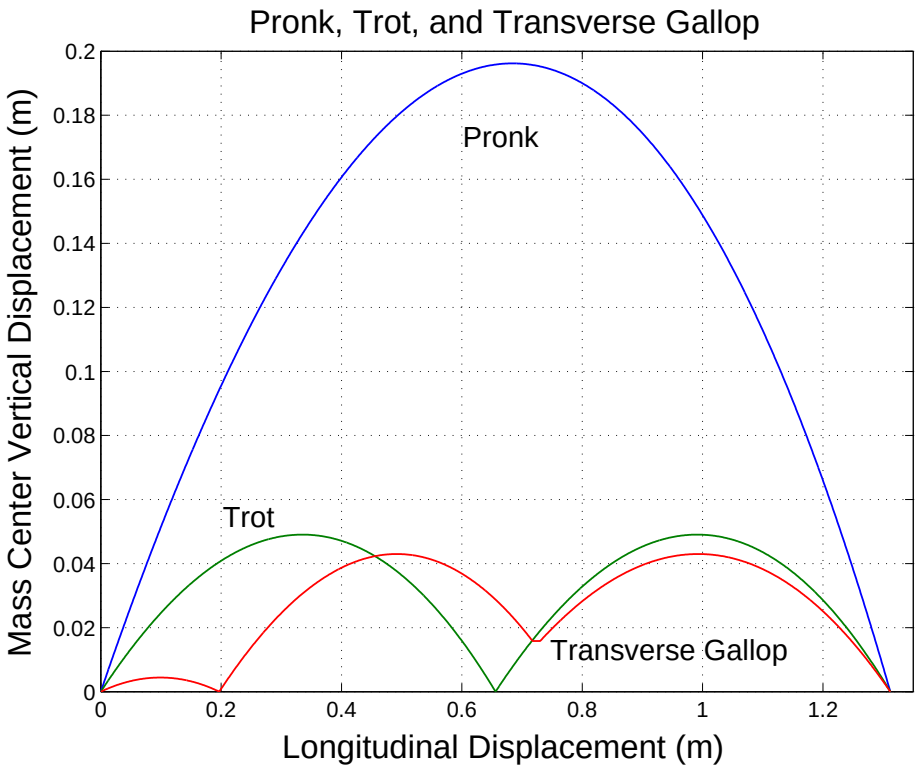

Figure 3.22: Vertical displacement of the mass center in a pronk, trot, and transverse gallop at the trot-to-gallop transition speed, u_x = 3.28 $\frac{m}{s}$, and stride period, T = 0.40 s.

The model presented in this chapter is limited in that it does not explain why trotting is preferable at lower speeds. In Table 3.11, galloping involves smaller vertical displacements at all speeds/stride periods, even the preferred trotting speed/stride period. Experience with the model suggests that altering the level of drag for different speeds does not lead to a clear advantage for trotting at lower speeds. It seems that this model best captures natural behavior at high speeds when the impulsive model more closely approximates the support phases of the legs. Chapter 4 introduces a different model that works better at lower speeds and in conjunction with this model, accounts for the transition from trotting to galloping.

3.6 Summary

A relatively simple model of galloping in which the support phases of the legs are assumed to be infinitesimal is extended to all dynamic gaits employed by mammalian quadrupeds: transverse gallop, rotary gallop, pronk, trot, pace, bound, half-bound, and canter. The vertical displacements of the mass center in each of these gaits are compared at three different speed and stride frequency combinations. The pronk involves the largest vertical oscillations, while the half-bound appears to involve the smallest. The key result, however, is that galloping requires smaller vertical displacements than trotting does even if the phasing of the legs is asymmetrical. This offers one explanation for the almost universal preference for galloping at high speeds among biological quadrupeds.

CHAPTER 4

SPRING-MASS MODEL

4.1 Introduction

As stated in the preceding chapter, the vertical oscillations of the mass center in dynamic locomotion can always be reduced by increasing the stride frequency. Conversely, the stride frequency can always be reduced by increasing the vertical oscillations of the mass center. Biological quadrupeds appear to strike a balance between these two by selecting gaits so as to minimize their stride frequencies without experiencing unnaturally large vertical oscillations.

This chapter introduces spring-mass models of trotting and galloping and investigates the parameters required to achieve motion having equal stride frequencies and vertical oscillations with both. These models more closely approximate motion at low speeds than do the impulsive models of the previous chapter because the compliant legs account for finite stance times.

4.2 Background

Heglund et al. [51] calculated a one-to-one relationship between stride frequency and the energetic cost of locomotion in quadrupeds at the trot-to-gallop transition speed. Heglund and Taylor [52] extended this idea to theorize that the rate of energy consumption per

kilogram of active muscle is directly proportional to the stride frequency at all equivalent speeds. One possible explanation for this direct link between energy and stride frequency is the relationship between stride frequency and leg return frequency.

4.2.1 Leg Return Frequency

As shown in Figure 4.1, a leg in return is fundamentally a compound gravitational pendulum that swings about its shoulder/hip joint. If allowed to return solely under the influence of gravity, it has a constant frequency. Gambaryan [46] and Howell [66] both observed that biological quadrupeds return their legs at frequencies that are nearly constant regardless of speed. Pearson [96] collected data from cats and cockroaches indicating that they display this behavior when walking.

Driving a leg at an oscillation frequency other than its natural frequency requires a significant amount of power from the actuators, as is shown mathematically in Appendix A. The average power, P, needed to drive a leg at frequency ω different from its natural frequency ω_n is,

$$P = \frac{I\Phi^2\omega(\omega_n^2 - \omega^2)}{\pi}, \tag{4.1}$$

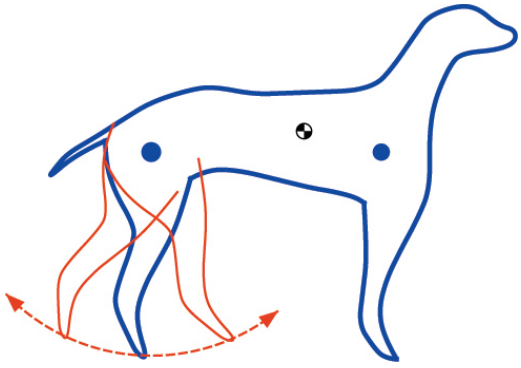

Figure 4.1: Outline of a greyhound showing the pendular motion of a hind leg.

where I is the moment of inertia of the leg about the axis of rotation and Φ is the angle through which the leg is driven.

Hildebrand [60] calculated that for all speeds above slow walking, biological quadrupeds must drive their legs at frequencies higher than their natural frequencies. This is because leg return frequency is directly related to stride frequency. A quadruped cannot complete a single stride cycle until each leg has returned to its initial position relative to the body, and stride frequency must be sufficiently high such that the propulsive action of the legs occurs regularly enough to maintain the desired speed [78]. If Hildebrand's conclusion is correct, minimizing the leg return frequency in dynamic locomotion would minimize the energy an animal expends moving its legs relative to its body. Furthermore, this would be more important as speed increases because the legs are driven through larger angles [34].

It is possible, though, that Hildebrand's calculations underestimated the natural frequencies of animal legs for two reasons. First, animals fold each leg when it is in the return phase, thereby reducing its moment of inertia about the shoulder/hip joint and increasing its natural frequency. At higher speeds, the legs are often folded more. Secondly, elastic energy can be stored in muscles and tendons acting across the shoulder/hip joint such that they behave as springs in parallel with the pendular leg [7]. This would also increase the natural frequency of leg oscillation.

Still, biological data suggests that animals do select gaits so as to minimize their stride frequencies, and correspondingly, their leg return frequencies. Figure 4.2, recreated from Heglund et al. [53], plots stride frequency as a function of speed for several animals. The change in slope of each plot represents the trot-to-gallop transition for the animal such that the segment of the plot at lower speeds corresponds to trotting and the segment at

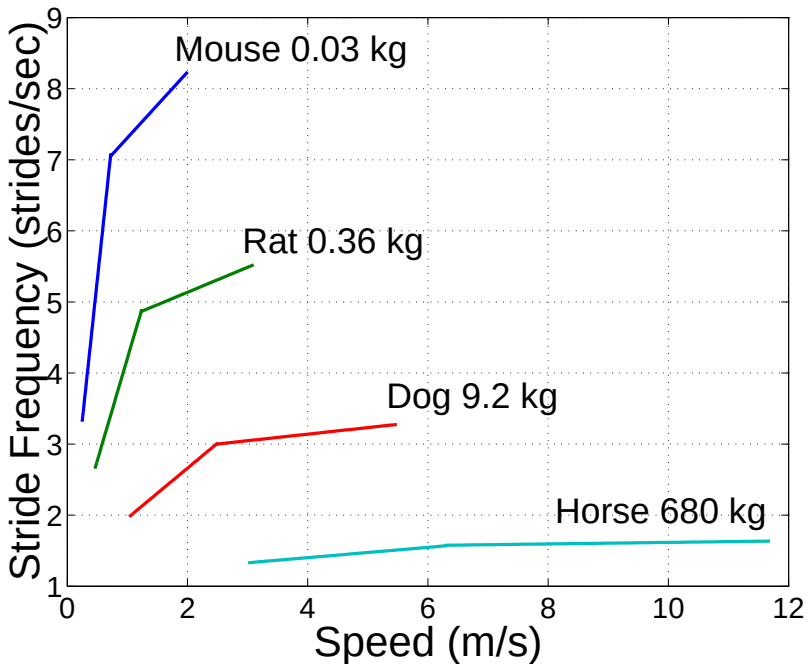

Figure 4.2: Stride frequency vs. speed for trotting and galloping animals, recreated from Heglund et al. [53].

higher speeds corresponds to galloping. For trotting at speeds above the natural trot-to-gallop transition, the predicted stride frequency is found by extending the trotting segment of each plot. Similarly, the predicted galloping stride frequency at lower speeds can be found by extending the galloping segment of each plot in the opposite direction. From this perspective, it is clear that animals change from a trot to a gallop in order to minimize their stride frequencies. Nanua and Waldron [92] observed this same behavior in their spring-mass model of a quadruped.

Heglund et al. [53] collected data only from mammals, but Blickhan and Full [20] observed that ghostcrabs changed from a trot-like gait to a gallop-like gait at about the same speed and stride frequency as a mouse of the same mass. Cockroaches follow similar trends

if the relationships are extended to animals of very small mass [43] [44]. Minimizing stride frequency, then, may be a characteristic of eight-legged arthropod locomotion as well.

4.2.2 Spring-Mass Models

A number of spring-mass models have been proposed as simple, general tools for characterizing terrestrial locomotion with different numbers of legs. Blickhan [18] compared the leg forces, leg compressions, and energy fluctuations of bipedal runners and hoppers with his spring-mass model. Alexander [8] investigated the Froude number at the transition from walking to running with his bipedal model. McMahon [84] introduced a model having arc-shaped feet to compare bipedal running and hopping and quadrupedal trotting, bounding, and galloping. His results indicated that galloping requires lower whole-animal and individual leg stiffness than does trotting, an idea pursued in more detail later in this chapter.

McMahon and Cheng [85] developed a simple model similar to Blickhan's that is applicable to bipedal running and hopping and quadrupedal trotting. The trotting model introduced in this chapter was inspired largely by that of McMahon and Cheng. Farley et al. [34] also used McMahon and Cheng's model in conjunction with biological data to investigate how leg stiffness can be predicted as a function of body mass. Nanua and Waldron compared the energetics of trotting, bounding, and galloping [92] and identified chaotic behavior in galloping [91] with a more complex spring-mass model. Their results indicated that galloping requires less elastic energy storage in the legs at high speeds, while trotting requires less elastic energy storage at low speeds. Berkemeier [16] used a simpler model to compare bounding and pronking in place. The galloping model proposed in this work bears some similarity to Berkemeier's model.

4.3 Trotting Model

Figure 4.3 is a schematic of McMahon and Cheng's [85] spring-mass model as implemented by Farley et al. [34] to study quadrupedal trotting. All out-of-plane motion is neglected, so the model is two-dimensional. The body is modeled as a single point mass, and each diagonal leg-pair is modeled as a single linear, compression spring connecting the point mass to a massless foot. This will be referred to as the virtual leg spring. Since the trot is a symmetrical gait, only half of the stride cycle must be examined, as the other half differs only in that the opposite diagonal pair of legs provides support.

The stiffness of the virtual leg spring, k_{leg}, can be expressed in terms of the maximum vertical ground force, F, and the compression of the leg spring, ΔL, when it is vertically oriented,

$$k_{leg} = \frac{F}{\Delta L}. \tag{4.2}$$

For trotting, the free length of the leg spring, L_o, is defined to be the average of the

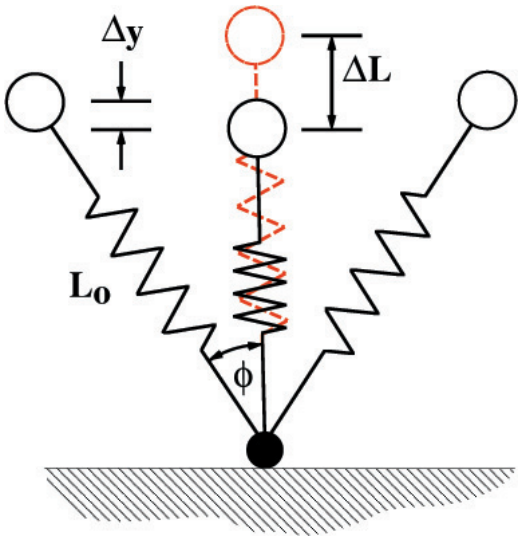

Figure 4.3: Schematic of the trotting spring-mass model, recreated from Farley et al. [34].

front and hind leg lengths at touchdown. The model assumes that L_o has a constant value independent of speed, which parallels the assumption in Chapter 3 that the legs operate at an optimal working length.

The effective vertical stiffness of the virtual leg spring, k_{vert}, is used to describe the vertical motions of the point mass while the foot is in contact with the ground and is given by,

$$k_{vert} = \frac{F}{\Delta y}, \tag{4.3}$$

where Δy is the change in the vertical position of the point mass during the support phase. Referring to Figure 4.3, the change in the virtual leg spring length, ΔL, can be related to Δy and the half angle, ϕ, through which the leg rotates,

$$\Delta L = \Delta y + L_o(1 - \cos\phi). \tag{4.4}$$

This relationship assumes that the rotation of the virtual leg spring is symmetric with respect to the vertical. In reality, the rotation of a leg shifts asymmetrically backward so that thrust can be provided to accelerate the mass center and compensate for drag. The simplification to symmetric leg rotation represents lossless locomotion at a constant speed.

Farley et al. [34] further assume that the horizontal velocity, u, is constant throughout the support phase in order to express ϕ as a function of the duration of contact, t_c,

$$\phi = \sin^{-1}\left(\frac{ut_c}{2L_o}\right). \tag{4.5}$$

While this is only an approximation of the actual behavior during contact, it is at least generally consistent with their data showing that the legs rotate through larger angles as speed increases.

With the introduction of k_{vert}, all of the pertinent motion of the two-degree-of-freedom model shown in Figure 4.3 can be captured with a one-degree-of-freedom model like the

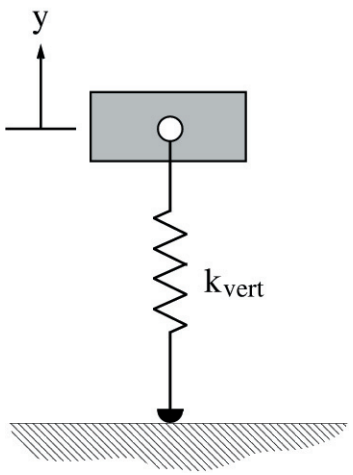

Figure 4.4: One degree-of-freedom spring-mass model.

one shown in Figure 4.4. Here, the point mass is shown as a block since the motion is confined to the vertical direction and no rotation can take place. Assuming that ground contact occurs at time $t = 0$, the equation of motion for the body while the foot is in contact with the ground is given by,

$$\ddot{y} + \frac{k_{vert}}{m} y = -g, \tag{4.6}$$

where y is the vertical position of the mass center, m is the mass, and g is the magnitude of the acceleration of gravity. If v is the magnitude of the body's speed at ground contact, the initial conditions are $\dot{y}(0) = -v$ and $y(0) = 0$. The solution to Equation 4.6 satisfying these conditions is,

$$y = \frac{mg}{k_{vert}} \left[\cos\left(\sqrt{\frac{k_{vert}}{m}} t \right) - 1 \right] - v \sqrt{\frac{m}{k_{vert}}} \sin\left(\sqrt{\frac{k_{vert}}{m}} t \right). \tag{4.7}$$

Since the leg rotation is symmetric, the duration of contact, t_c, is simply twice the time it takes the body to travel from its height at ground contact to its minimum height. This time is found by differentiating Equation 4.7 with respect to time and solving for the value

of t for which $\dot{y} = 0$. The duration of contact, then, is given by,

$$t_c = 2\sqrt{\frac{m}{k_{vert}}}\left[\pi - \tan^{-1}\left(\frac{v}{g}\sqrt{\frac{k_{vert}}{m}}\right)\right]. \tag{4.8}$$

In the flight phase, the motion is ballistic, so the duration of flight between ground contacts is given by,

$$t_f = \frac{2v}{g}. \tag{4.9}$$

The stride period, T, of trotting is twice the sum of the durations of flight and contact for the model since only half of the stride cycle is modeled,

$$T = 4\sqrt{\frac{m}{k_{vert}}}\left[\pi - \tan^{-1}\left(\frac{v}{g}\sqrt{\frac{k_{vert}}{m}}\right)\right] + \frac{4v}{g}. \tag{4.10}$$

Farley et al. [34] compared the ground contact time with one half the resonant period of oscillation of the spring mass system, which assumes that the duration of flight dominates. With this assumption, a 38% error was found in the coefficient of their exponential relationship. Their data actually matches better the assumption that the duration of contact dominates, as this yields only a 22% error in the same coefficient. Still, both of these errors are quite significant. This is why the effects of both the flight and the contact phases are included in Equation 4.10 to calculate the stride period.

The change in vertical position of the mass center, Δy, during contact is simply the magnitude of y evaluated at time $\frac{t_c}{2}$,

$$\Delta y = \frac{mg + \sqrt{m^2g^2 + mk_{vert}v^2}}{k_{vert}}. \tag{4.11}$$

Combining Equations 4.2, 4.3, and 4.4 yields,

$$\frac{k_{vert}}{k_{leg}} = 1 + \frac{L_o(1 - \cos\phi)}{\Delta y}, \tag{4.12}$$

and making substitutions from Equations 4.5, 4.8 and 4.11,

$$\frac{k_{vert}}{k_{leg}} = 1 - \frac{L_o k_{vert} - \sqrt{L_o^2 k_{vert}^2 - m k_{vert} u^2 \left[\pi - \tan^{-1}\left(\frac{v}{g}\sqrt{\frac{k_{vert}}{m}}\right)\right]^2}}{mg + \sqrt{m^2 g^2 + m k_{vert} v^2}}. \tag{4.13}$$

Given the horizontal velocity u, the stride period T, and the parameters that define the model, Equations 4.10 and 4.13 form a system of two nonlinear equations in the two unknowns, k_{vert} and v. They can be solved numerically to fully determine the motion that corresponds to the chosen horizontal velocity and stride period. The required model parameters include m, L_o, and k_{leg}. As stated, L_o can be assumed constant for all speeds just as the legs were assumed to operate at an optimal working length in the previous chapter. Similarly, Farley et al.'s [34] data suggests that k_{leg} is nearly independent of speed. Since ϕ increases with increasing velocity, though, k_{vert} increases with speed.

4.4 Galloping Model

Figure 4.5 is a schematic of the spring-mass model for galloping. Like the trotting model, the galloping model is two-dimensional, so roll, yaw, and lateral translation are neglected. Unlike the trotting model, though, the body has finite dimension because its pitch motion is significant in galloping. It has mass m and pitch moment of inertia I.

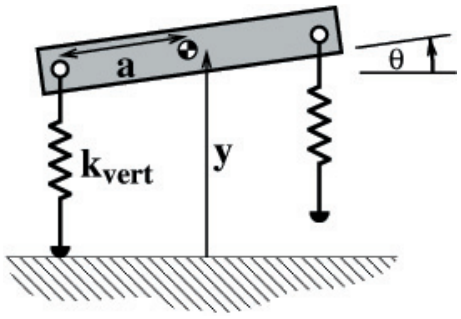

Figure 4.5: Schematic of the galloping spring-mass model.

The body is assumed to be symmetric such that the mass center is equidistant between the shoulders and hips, with that distance denoted as a in Figure 4.5. As is discussed in Chapter 2, most biological quadrupeds have an asymmetrical mass distribution, but this would add significant complexity to the model. It remains a subject for future work with this model.

Each front and hind leg-pair is modeled as a single, linear compression spring of stiffness k_{vert}. In this way, the model addresses only the vertical translation, y, and pitch rotation, θ, of the body. The longitudinal translation contributes only to determining the value of k_{vert}, just as in the trotting model. This reduces what would normally be a three-degree-of-freedom model to two degrees of freedom. Berkemeier [16] developed a similar model that included damping in the legs to investigate pronking and bounding in place.

The k_{vert} employed in the galloping model is not necessarily equivalent to that of the trotting model. Here, it accounts for the effective vertical stiffness of the front or hind leg-pair. The legs within the pair do not generally operate in phase, as that would constitute a bound rather than a gallop. Still, an effective vertical stiffness of the leg-pair could be calculated from the average change in vertical position of the shoulder/hip joints and the maximum vertical force during the time between the touchdown of the first leg and the lift-off of the second in the pair. Since the legs operate somewhat out of phase, the vertical stiffness of a pair in galloping is expected to be slightly less than in trotting even if the legs rotate through the same angles.

The length of each virtual leg spring, L, during the contact phase is related to the vertical position of the mass center and the pitch angle of the body,

$$L = y - a\sin\theta. \tag{4.14}$$

Since only the effective vertical stiffness is modeled, the virtual leg springs do not change orientation when the body rotates; they always remain vertical. With L_o again denoting

the free length of the virtual leg spring and g the acceleration of gravity, the equations of motion for the model during the contact phase are,

$$\ddot{y} = \frac{L_o k_{vert} - mg}{m} - \frac{k_{vert}}{m} y + \frac{a k_{vert}}{m} \sin\theta, \tag{4.15}$$

and,

$$\ddot{\theta} = -\frac{a L_o k_{vert}}{I} \cos\theta + \frac{a k_{vert}}{I} y \cos\theta - \frac{a^2 k_{vert}}{I} \cos\theta \sin\theta. \tag{4.16}$$

If v is again the magnitude of the mass center's vertical velocity at ground contact and ω_o is the pitch angular velocity at the same time, the velocity initial conditions are $\dot{y}(0) = -v$ and $\dot{\theta}(0) = \omega_o$.

As in the trotting model, the motion is assumed to be symmetric, so at the top of the flight phase, $\theta = 0$. Since the pitch angular velocity does not change during the flight phase, the initial condition for the pitch angle is the product of ω_o and one half the duration of the flight phase. The ballistic motion of the galloping model is the same as that of the trotting model, so the duration of flight is again given by Equation 4.9. Therefore, $\theta(0) = \frac{v\omega_o}{g}$. Substituting into Equation 4.14, the other initial condition is $y(0) = L_o + a \sin\left(\frac{v\omega_o}{g}\right)$.

Given all of the parameters in Equations 4.15 and 4.16 and the corresponding initial conditions, the model's motion can be found through dynamic simulation. For the simulation to be meaningful, however, the parameters must be selected such that the resulting motion is symmetric, since this was assumed in developing the initial conditions. If t_{lo} is the time at which the foot lifts off from the ground following the contact phase, motion symmetry is satisfied when $y(t_{lo}) = y(0)$, $\dot{y}(t_{lo}) = -y(0)$, $\theta(t_{lo}) = \theta(0)$, and $\dot{\theta}(t_{lo}) = -\dot{\theta}(0)$. The method of selecting the parameters necessary to satisfy these constraints is discussed in the following section.

As discussed in Chapter 3, galloping motion is generally asymmetrical. The gathered flight phase is typically longer than the extended flight phase, and the front and hind leg-pairs perform different functions. The spring-mass model for galloping was developed to be as simple as possible and yet still capture the most important aspects of vertical translation and pitch rotation. A more complex model that would accommodate more typical asymmetrical motion is again the subject of future work.

4.5 Comparison of the Models

The behavior of the trotting and galloping models was compared to determine if minimizing stride frequency could account for the transition from trotting to galloping.

4.5.1 Model Parameters

Table 4.1 lists the parameters that are the same in both the trotting and the galloping models. As for the impulsive model in Chapter 3, L_o and m were both taken from the biological model developed in Chapter 2. The pitch moment of inertia, I = 3.37 $kg \cdot m^2$,

Parameter	**Value**	**Units**
L_o	0.7	m
m	33.0	kg
g	9.81	$\frac{m}{s^2}$
k_{leg}	9.294	$\frac{kN}{m}$
u	varies	$\frac{m}{s}$
T	varies	s
v	varies	$\frac{m}{s}$

Table 4.1: Parameters common to the trotting and galloping models.

was also the same as that of the impulsive model, but it is used only in the galloping model. Similarly, a = 0.24 m in the galloping model is one half the distance between the shoulders and the hips in the impulsive model.

The trotting and galloping models were compared at five different stride periods corresponding to the following equivalent speeds [98]: minimum trotting speed, preferred trotting speed, trot-to-gallop transition speed, preferred galloping speed, and maximum galloping speed. The values for the five stride periods were calculated with Heglund and Taylor's [52] allometric equations for stride frequency. Since the speed is also needed in the trotting model, the five corresponding speeds were also calculated from their allometric equations.

The value of k_{leg} was chosen to be the minimum value that resulted in an infinitesimal flight phase of the trotting model at the minimum trotting speed and stride period. Smaller values of k_{leg} resulted in motion without a flight phase, which would correspond to what Heglund and Taylor [52] characterize as walking rather than trotting. Farley et al. [34] found k_{leg} to be an exponential function of body mass,

$$k_{leg} = 0.715m^{0.67\pm0.15}. \tag{4.17}$$

The chosen value of k_{leg} in Table 4.1 corresponds to an exponent of 0.73 in Equation 4.17, which is well within the tolerance band. Therefore, the chosen value is in agreement with biological data. k_{leg} does not appear specifically in the galloping model; however, the assumption that it is the same for both models is critical in interpreting the results.

The vertical velocity of the mass center at touchdown, v, is found by solving the equations of the trotting model for each horizontal speed and stride period combination. With the same value used in the galloping model, the vertical excursions of the mass centers during flight phases are equal in the two gaits. This commonality is critical to the comparison

of the two gaits. As stated at the beginning of this chapter, the stride frequency and vertical oscillation of the mass center are highly dependent upon each other.

4.5.2 Method of Solution

The motion of the trotting model was found by solving Equations 4.10 and 4.13 for v and k_{vert} with the Newton-Raphson Method for each of the five horizontal speed and stride period combinations. The motion of the galloping model was found through dynamic simulation of Equations 4.15 and 4.16 with Matlab's Simulink package using a fixed time step of 0.0001 s and fifth-order Dormand-Prince integration. The simulation was stopped at time $t_{lo} = \frac{T}{2} - \frac{2v}{g}$ since this is the instant at which the leg-pair must lift-off from the ground in order for the galloping stride period to be equal to the trotting stride period.

Following each simulation, the four symmetry constraints for the galloping model were evaluated. The values of k_{vert} and ω_o in the simulation were then altered in order to converge to a motion satisfying the four symmetry constraints. The iterative process of simulation and k_{vert} and ω_o selection was repeated until the four constraints were all satisfied with less than 1 % error. In all cases, refining the final solution values of k_{vert} and ω_o with an increasing number of significant figures further reduced the error. The angular position constraint on θ for minimum trotting was a unique case. Because there is no flight phase at the minimum trotting speed, the required value of θ is 0, and a percentage error is non-sensical. Instead, the constraint was considered satisfied once $\theta(t_{lo})$ took on an appropriately small value.

4.5.3 Results

The behavior of the two models was in general agreement with Farley et al.'s [34] observations of animals. As speed increased, the duration of contact decreased along with

the change in vertical position of the mass center during contact. The change in length of the virtual leg spring increased, as did the vertical oscillation of the mass center during flight.

Table 4.2 lists the calculated values of k_{vert} at the corresponding speeds and stride periods for both the trotting and the galloping models. These are the effective vertical leg stiffnesses necessary to achieve the same vertical oscillation of the mass center with the two gaits at the same stride frequency. It is important to note that the leg-pair stiffness, k_{leg} = 9.294 $\frac{kN}{m}$, is assumed to be the same in both models and independent of speed.

In Table 4.2, the values of k_{vert} for the trotting model are all greater than k_{leg}. Recalling Equation 4.12, this behavior is required by the very definition of the model. If the horizontal velocity is zero and the legs do not rotate at all, k_{vert} = k_{leg}. For all increasing horizontal velocities, though, k_{vert} becomes increasingly larger than k_{leg}.

The calculated values of k_{vert} for the galloping model are actually less than k_{leg} at the minimum and preferred trotting speeds. This indicates that at these lower speeds, galloping with the same vertical oscillation of the mass center as is found in trotting requires legs

	Speed (m/s)	**Stride Period** (s)	**Trot** k_{vert} (kN/m)	**Gallop** k_{vert} (kN/m)
Minimum Trot	1.42	0.57	16.14	5.42
Preferred Trot	2.37	0.47	23.83	9.00
Trot-to-Gallop Transition	3.28	0.40	33.18	13.31
Preferred Gallop	5.14	0.39	44.07	21.07
Maximum Gallop	6.86	0.38	56.89	29.12

Table 4.2: Calculated values of k_{vert} for trotting and galloping at five equivalent speeds.

of lower stiffness. As previously stated, though, leg stiffness has been found to be nearly constant. Therefore, the lower values of k_{vert} at the typical trotting speeds indicate that galloping simply cannot be accomplished at those speeds with the same stride frequency and vertical oscillation as trotting. Simulation results showed that if more reasonable values of k_{vert} were used at these lower speeds, either the vertical oscillation or the stride frequency was greater than in trotting.

As stated in Section 4.4, the values of k_{vert} within the two models are not entirely equivalent because the legs are used in pairs in trotting and are used slightly out of phase in galloping. The small separation of the legs in galloping should yield lower effective vertical stiffness, although not values as low as those calculated for the two lowest speeds. In order for these values to be reasonable, the separation of the legs would be unnaturally large, and stable galloping would be unlikely. The results of the impulsive model in Chapter 3 show that the legs of the front and hind pairs must operate nearly together, and observations of biological quadrupeds confirm this.

The comparison of the effective vertical stiffnesses at equivalent speeds within each gait offers an interesting result. The trotting value of k_{vert} at the minimum trotting speed is only slightly larger than the galloping value at the trot-to-gallop transition speed, which would be the minimum galloping speed. The same pattern is found in comparing the values of k_{vert} at the two preferred speeds and the two maximum speeds. This result is consistent with the idea that animals move their legs through the same angles at their equivalent speeds within each gait. As before, the galloping k_{vert} is expected to be smaller because of the phase difference between the legs.

The large values of k_{vert} for trotting at the typical galloping speeds are also consistent with the idea that leg return is an important determinant of gait. To achieve these large

values, the legs must rotate through very large angles, so the required power in Equation 4.1 would also be large.

In general, the results of the two models indicate that trotting requires smaller vertical oscillations of the mass center and/or lower stride frequencies than galloping at speeds below the trot-to-gallop transition. At higher speeds, trotting requires the legs to rotate through very large angles.

4.6 Summary

Biological quadrupeds change gaits in order to minimize their stride frequencies at least in part because this minimizes the power they expend in returning their legs. Simple, spring-mass models of trotting and galloping are introduced for comparing the two gaits. The results indicate that trotting requires smaller vertical oscillations of the mass center and/or lower stride frequencies than galloping at low speeds. At higher speeds, trotting requires the legs to rotate through excessively large angles. The results of the impulsive model in Chapter 3 offer an explanation for why galloping is preferred at higher speeds. The results of the spring-mass models in this chapter offer an explanation for why trotting is preferred at lower speeds. In combination, the two account for the trot-to-gallop transition in biological quadrupeds.

CHAPTER 5

IMPACT LOSSES

5.1 Introduction

Unlike wheeled and tracked systems, the motion of legged systems fundamentally involves a regular sequence of collisions with the environment, one for every touchdown of a foot on the terrain. Obstacles pose the threat of unexpected and potentially damaging collisions for any mobile system, but relatively severe impacts can be a part of basic operation with legs. It is desirable to minimize the kinetic energy lost with each foot impact, particularly since any autonomous legged system must carry its own energy source on board. Less energy loss at impact corresponds to less required weight for the on-board energy source. In statically stable locomotion, the feet can be placed softly on the terrain because the speed of travel is relatively slow. In dynamically stable locomotion, though, more severe collisions of the feet with the terrain result from the ballistic motion of the body in flight phases. As the height of the ballistic trajectory increases, so does the severity of the corresponding collision.

Chapter 3 introduced the argument that large vertical oscillations of the mass center of a legged system are undesirable because they result in large energy losses each time a foot impacts the ground. This chapter formalizes the mathematics upon which the argument is based, providing a means of directly calculating the kinetic energy loss given the geometric

and inertial properties of the leg, the velocity of the foot at touchdown, and the leg position at touchdown. Furthermore, this chapter presents the generalized inertia ellipsoid (GIE) as a visualization tool for comparing the impact losses of different leg designs. While the design of legs for energy-efficient dynamic locomotion motivates this work, the results are completely general in that they could be applied to any system that experiences a plastic collision with a stationary environment [114].

5.2 Background

A schematic of Raibert's [103] planar monopod hopping machine is shown in Figure 5.1(a). It consists of a compliant telescoping leg (a piston-cylinder combination) attached to a rigid body by a revolute joint. Assuming a perfectly plastic collision with no foot slip, Raibert employed conservation of linear momentum to estimate the percentage of the machine's kinetic energy lost each time the foot impacts the terrain.

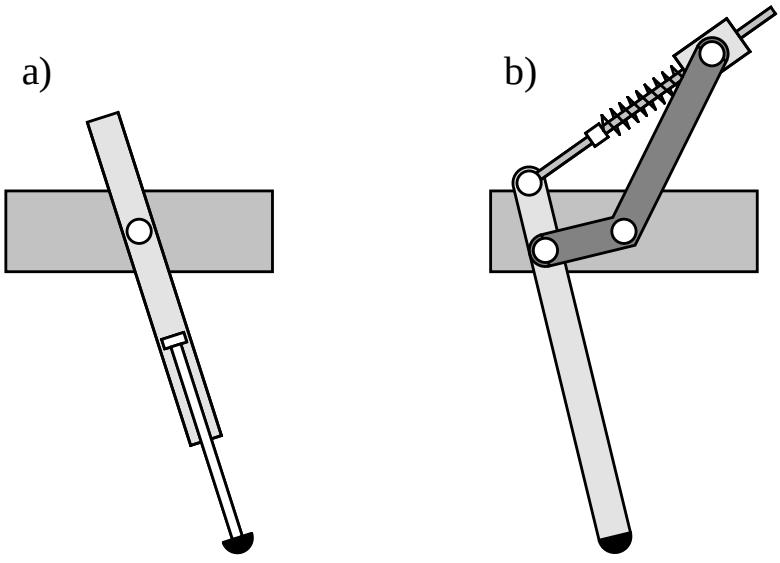

Figure 5.1: Schematics of a) Raibert's planar monopod and b) a planar monopod with an articulated leg.

$$\%KE_{loss} = \frac{m_l}{m_l + m}. \tag{5.1}$$

m_l is the unsprung mass of the leg which consists of the foot and piston assembly of the piston-cylinder. m is the remaining mass of the machine. This suggests that minimizing the unsprung leg mass minimizes the energy loss, and thus, the corresponding design guideline is relatively simple.

Raibert's calculation, however, assumes that the rotational kinetic energy of the leg is negligible both prior to and after the impact. This is a reasonable approximation because Raibert's control scheme moves the leg to its desired position before touchdown, and rotation immediately after touchdown is minimal since the revolute joint lies on the axis of the prismatic joint. Actually, if the leg is held in a fixed position at touchdown, Equation 5.1 overestimates the loss by the amount of rotational kinetic energy in the leg immediately after impact.

For an articulated leg like the one shown in Figure 5.1(b), though, the rotation of the lower leg is significant following an impact regardless of how it is controlled prior to touchdown. Simply minimizing the mass of this part of the leg as if it were the unsprung mass in Equation 5.1 is not a practical means of reducing energy loss. Therefore, a general calculation of kinetic energy loss is needed for legs of more widely varying design. This analysis is presented in the following section.

Calculating energy loss at impact is not terribly useful as a design tool, however, unless it provides some insight as to why one leg design is superior to another. Since the general calculation of energy loss is more complex than Equation 5.1, the comparison of designs is likewise more complex than simply comparing the masses of leg parts. Fortunately, ellipsoids have been used extensively in manipulator design as visualizations that provide

exactly the kind of intuition required for this problem. The generalized inertia ellipsoid is introduced for this purpose later in the chapter.

Asada [13] extended the inertia ellipsoid of a single rigid body to a series of rigid bodies connected by joints with his definition of the generalized inertia ellipsoid (GIE). He used the GIE to represent the inertial characteristics of an entire manipulator with respect to the end effector. The graphical representation helped generate manipulator designs having more isotropic inertial properties and smaller nonlinear effects throughout their workspaces. Hogan [65] subsequently introduced the geometric dual of the GIE as the ellipsoid of gyration and applied it to the modulation of end-point impedance in redundant manipulators. He argued that the ellipsoid of gyration is more fundamental than the GIE for a couple of reasons. First, it can be obtained even when the Jacobian cannot be inverted. Secondly, its principal axes can have zero length, but will never have infinite length.

Yoshikawa defined the manipulability ellipsoid [133] and its geometric dual, the manipulating force ellipsoid [134], as measures of the ability to position and orient an end effector in space. He proposed to use these ellipsoids for analysis, design, and control of manipulators, specifically focusing on determining optimal postures for redundant manipulators. He later extended this work to include dynamic effects with the dynamic manipulability ellipsoid [135].

While some of the previous work alluded to the possibility, Walker [129] formally investigated ellipsoids as impact measures by introducing the dynamic impact ellipsoid, which is the geometric dual of the dynamic manipulability ellipsoid, and by reevaluating the ellipsoid of gyration as what he called the generalized impact ellipsoid. Unfortunately, this work erroneously related the ellipsoid of gyration to the change in kinetic energy following

impact and had to be corrected later [48]. Subsequent analysis in this chapter shows that Walker's claim has validity, but only when the collision is perfectly plastic.

5.3 Impact Model

Zheng and Hemami [137] developed the mathematical model of a robot colliding with its environment that is employed in this work. The model assumes that contact occurs at a single point resulting in no deformation of either the robot or the environment. Furthermore, the environment is assumed to be stationary. Their work showed that the instantaneous change in the joint velocity vector, $\dot{\mathbf{q}}$, can be related to the instantaneous change in the velocity vector of the contact point in the end effector, $\dot{\mathbf{x}}$.

$$\Delta\dot{\mathbf{q}} = D^{-1}J^T(JD^{-1}J^T)^{-1}\Delta\dot{\mathbf{x}}. \tag{5.2}$$

D is the symmetric, positive definite inertia matrix, and J is the Jacobian that relates the velocity of the end effector to the joint velocities. (The notation employed throughout this chapter follows that of Zheng and Hemami [137], which is why, unlike in other chapters, D is used to indicate an inertia matrix.) In the present work, the contact point in the end effector corresponds to the tip of a hemispherical foot, as shown in Figure 5.2. This assumes that the point of impact in the foot is the same regardless of the leg position at touchdown

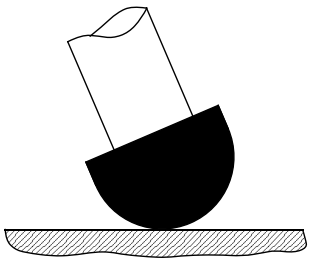

Figure 5.2: Hemispherical foot contacting stationary terrain.

and is reasonably accurate for a small foot.

The matrix $D^{-1}J^T(JD^{-1}J^T)^{-1}$ in Equation 5.2, which will subsequently be denoted as $\bar{J}$, is the dynamically consistent generalized inverse of the Jacobian defined by Khatib [71]. This particular generalized inverse corresponds to the solution that minimizes the instantaneous kinetic energy of a redundant manipulator. Viewed in this manner, a legged robot is treated as a redundant manipulator, with the redundancy coming from the degrees of freedom of the robot's trunk. For example, a legged robot may have a three-degree-of-freedom leg so that it can arbitrarily position the foot relative to the trunk. During a flight phase, the six degrees of freedom of this same robot's trunk must be considered in addition to the three leg degrees of freedom relative to the trunk. The joint velocity vector, $\dot{\mathbf{q}}$, in Equation 5.2 contains the leg joint velocities and the velocity of the robot trunk. For a quadruped standing still on three of its legs and placing its fourth, three-degree-of-freedom leg on the terrain, the trunk degrees of freedom could be ignored, and the dynamically consistent generalized inverse would be the same as the simple inverse of the Jacobian.

Prior to impact, the kinetic energy of the machine is defined as,

$$KE = \frac{1}{2}\dot{\mathbf{q}}^T D\dot{\mathbf{q}}, \tag{5.3}$$

and after the impact, the kinetic energy is given by,

$$KE = \frac{1}{2}\dot{\mathbf{q}}^T D\dot{\mathbf{q}} + \dot{\mathbf{q}}^T D\Delta\dot{\mathbf{q}} + \frac{1}{2}\Delta\dot{\mathbf{q}}^T D\Delta\dot{\mathbf{q}}. \tag{5.4}$$

The first term in Equation 5.4 is equal to the kinetic energy before the impact, so the second and third terms account for the change in kinetic energy. The third term represents the kinetic energy associated with the change in joint velocities and is always non-negative. The second term, then, must be negative or zero, and as will be shown, is related to the third.

From the given definitions, the velocity of the foot prior to impact can be calculated,

$$\dot{\mathbf{x}} = J\dot{\mathbf{q}}. \tag{5.5}$$

Assuming a perfectly plastic collision and no slip, the velocity of the foot immediately after impact is zero. Thus, the change in velocity of the foot for this special case is given by,

$$\Delta\dot{\mathbf{x}} = -J\dot{\mathbf{q}}. \tag{5.6}$$

Note that a perfectly plastic collision is generally the most desirable for dynamic legged locomotion. It is best for the foot to establish a secure foothold immediately upon impact without bouncing or slipping on the terrain. Substituting into Equation 5.2,

$$\Delta\dot{\mathbf{q}} = -\bar{J}J\dot{\mathbf{q}}. \tag{5.7}$$

Recalling Equation 5.4 and substituting from Equation 5.7, the loss of kinetic energy can be written,

$$\Delta KE = \dot{\mathbf{q}}^T D\Delta\dot{\mathbf{q}} + \frac{1}{2}\dot{\mathbf{q}}^T J^T \bar{J}^T D\bar{J}J\dot{\mathbf{q}}. \tag{5.8}$$

Because D is a symmetric matrix, $A^T D = DA$ for any matrix A. Taking A to be $\bar{J}J$, Equation 5.8 can be rewritten,

$$\Delta KE = \dot{\mathbf{q}}^T D\Delta\dot{\mathbf{q}} + \frac{1}{2}\dot{\mathbf{q}}^T D\bar{J}J\bar{J}J\dot{\mathbf{q}}. \tag{5.9}$$

Recognizing that $\bar{J}$ is a right inverse, Equation 5.9 reduces to,

$$\Delta KE = \dot{\mathbf{q}}^T D\Delta\dot{\mathbf{q}} + \frac{1}{2}\dot{\mathbf{q}}^T D\bar{J}J\dot{\mathbf{q}}. \tag{5.10}$$

Substituting from Equation 5.7 and simplifying yields,

$$\Delta KE = \frac{1}{2}\dot{\mathbf{q}}^T D\Delta\dot{\mathbf{q}}, \tag{5.11}$$

Finally, after some algebra, the loss of kinetic energy is given by,

$$\Delta KE = -\frac{1}{2}\Delta\dot{\mathbf{q}}^T D \Delta\dot{\mathbf{q}}. \tag{5.12}$$

Note that this quantity is always negative or zero and not specific to legged robots. It is valid for all perfectly plastic collisions of a robot with a stationary environment assuming point contact and no deformation.

As written, however, Equation 5.12 is rather inconvenient because the changes in joint velocities after an impact are not generally known. The joint velocities immediately prior to impact, though, can be easily predicted for legged systems. If, for example, the leg of a monopod is moved to its desired position prior to touchdown, then the velocity of the robot trunk accounts for the only non-zero terms in the joint velocity vector. Therefore, the most useful form results from substituting Equation 5.7 into Equation 5.12 to yield,

$$\Delta KE = -\frac{1}{2}\dot{\mathbf{q}}^T (\bar{J}J)^T D (\bar{J}J)\dot{\mathbf{q}}. \tag{5.13}$$

For non-redundant robots, $\bar{J}$ is the simple inverse in Equation 5.13, and it is easily seen that all of the kinetic energy is lost in a perfectly plastic collision.

Impact analyses using Equation 5.13 and Raibert's [103] mass ratio in Equation 5.1 were compared for a simplified model of his planar monopod. As predicted, the two agree when there is no rotation of the leg either prior to or after impact. This corresponds to vertical hopping of the monopod with the leg in a purely vertical position. When the leg touches down at an angle or the body has forward velocity, though, rotation does occur following the impact, and the mass ratio overestimates the energy loss calculated with the present analysis because it ignores the rotational kinetic energy.

Equation 5.13 formalizes mathematically the argument that larger vertical oscillations of a legged system's mass center result in larger impact losses. Recall that the vector $\dot{\mathbf{q}}$

includes the leg joint velocities and the velocity of the robot trunk. In the simplest case of vertical hopping without any motion of the leg relative to the trunk, the only non-zero quantity in the vector $\dot{\mathbf{q}}$ is the vertical velocity of the trunk at touchdown. Since the body's trajectory during flight is ballistic, the magnitude of this velocity is proportional to the square root of the vertical oscillation. A larger oscillation yields greater losses. If forward motion and relative leg motion prior to touchdown are included, the loss of kinetic energy resulting from the vertical motion of the body is reduced only if the leg moves opposite the trunk in the vertical direction to reduce the change in foot velocity at impact.

This is shown mathematically by substituting Equation 5.2 into Equation 5.12 to express the energy loss as,

$$\Delta KE = -\frac{1}{2}\Delta\dot{\mathbf{x}}^T \bar{J}^T D \bar{J} \Delta\dot{\mathbf{x}}. \tag{5.14}$$

Here, $\Delta\dot{\mathbf{x}}$ is the change in foot velocity, which is equivalent to foot velocity relative to the ground immediately prior to impact. If the foot can be moved relative to the trunk in a direction opposite the motion of the trunk, this quantity could be zero, resulting in no impact loss at all. This idea provides some insight into how animals minimize impact losses in their locomotion. In Figure 5.3, the galloping cheetah begins to move its legs backward relative to its trunk long before the feet contact the terrain, so that at impact, the foot velocity relative to the ground is very small. The problem of implementing a similar control strategy in a legged robot is significant. The system would require a highly accu-

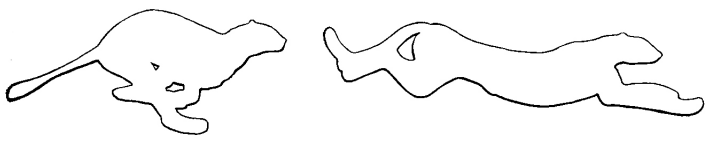

Figure 5.3: Cheetah in a rotary gallop drawing its legs backward prior to touchdown.

rate super-realtime simulation capable of predicting when the next leg touchdown would occur and commanding the appropriate leg motions to minimize the foot velocity change. Some savings could be achieved by simply moving the legs backward prior to touchdown without regard to exactly matching the relative ground velocity. This method, however, would require an accompanying novel control approach to stabilize the gait. The existing control approaches of Raibert [103] and Marhefka [79] depend upon commanding the leg angle at touchdown, and moving the leg backward relative to the trunk without an accurate prediction of the touchdown angle would likely create serious difficulty in implementing either of these approaches. As such, designing legs for minimal impact loss is even more important when implementing one of these existing control approaches.

5.4 Design Comparisons

The equations developed in the preceding section allow the designer of a legged robot to calculate the kinetic energy lost upon impact for any selected configuration of a given leg design. They do not, however, provide any natural intuition into why one design and configuration combination is superior to another. The generalized inertia ellipsoid can help develop this insight.

A quadratic surface associated with Equation 5.14 can be defined by,

$$\mathbf{u}^T \bar{J}^T D \bar{J} \mathbf{u} \leq 1. \tag{5.15}$$

For a non-redundant manipulator, Asada [13] calls this surface the generalized inertia ellipsoid (GIE). The only difference from his formulation is that the dynamically consistent generalized inverse of the Jacobian appears in Equation 5.15 instead of the simple inverse, which actually remedies Hogan's [65] concern that the GIE is undefined when the Jacobian is not invertible. Khatib [72] refers to the matrix $\bar{J}^T D \bar{J}$ as a "pseudo kinetic energy matrix"

in his work with the operational space formulation for redundant manipulators. Extracting the GIE from Equation 5.14, one can see that the change in kinetic energy following an impact can be related to the ellipsoid of gyration because it is the geometric dual of the GIE. Therefore, Walker's [129] attempt to do this was valid, but only for plastic collisions, and not for the elastic collisions he investigated.

Each eigenvector of the matrix $\bar{J}^T D \bar{J}$ defines a principal axis of the GIE, and the reciprocal of the square root of the corresponding eigenvalue defines the length of that axis. Figure 5.4 shows the principal axes of a general ellipsoid. Asada investigated the kinetic energy of a manipulator rather than the change in kinetic energy. Therefore, his interpretation of the GIE is that for constant kinetic energy, motion in the direction of the minor axis allows for the minimum end effector velocity or provides for the maximum generalized moment of inertia. Likewise, motion along the major axis allows for the maximum end effector velocity or provides for the minimum generalized moment of inertia.

For the purposes of this work, Asada's interpretation is inverted. For a given change in end effector velocity, $\Delta\dot{\mathbf{x}}$, the loss of kinetic energy is maximum if the direction of that

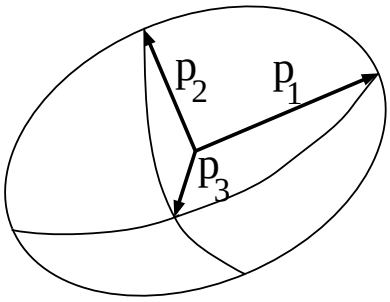

Figure 5.4: Principal axes of a generalized inertia ellipsoid.

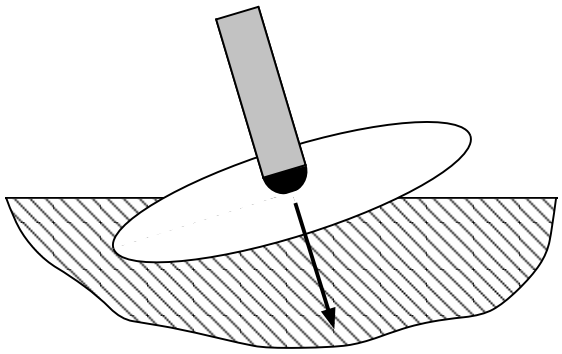

Figure 5.5: Touchdown scenario with maximum energy loss.

velocity change is along the minor axis of the GIE, as shown in Figure 5.5. Similarly, energy loss is minimum if the direction of the velocity change coincides with the major axis, as in Figure 5.6. The goal, then, is to design a leg and select its touchdown configuration such that the major axis of its GIE is aligned with the velocity of the foot immediately before impact with the terrain. If that is not possible, maximizing the length of the minor axis of the GIE for a given configuration will minimize the worst case kinetic energy loss. Asada focused on designing manipulators with nearly isotropic ellipsoids throughout their workspaces. To minimize kinetic energy losses in legged robots, though, ellipsoid

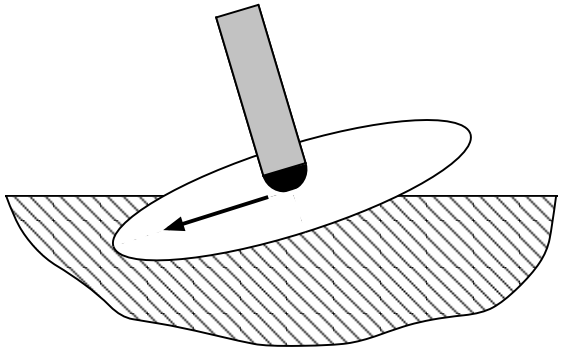

Figure 5.6: Touchdown scenario with minimum energy loss.

anisotropy should be exploited.

5.5 Example

This section presents the impact analysis of an articulated leg that was originally designed to be part of a quadruped robot. Since the dynamics of the still somewhat undefined quadruped were not well known, a simplified planar monopod model was used for the initial evaluation of leg designs. This simplified analysis is a useful preliminary design tool, and the dynamics of the full quadruped model can be incorporated should more accurate analysis be required.

As shown in Figure 5.7, the planar monopod model consists of a candidate leg attached at the hip joint to a point mass (shown as a circle) that represents one fourth of the trunk mass. The angular velocity of the robot trunk is neglected. The vertical distance from the point mass to the foot for the shown configuration is about 0.5 m, and the total mass of

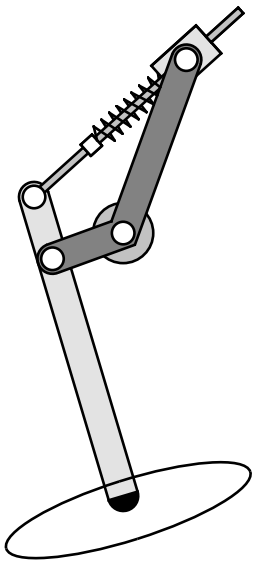

Figure 5.7: Schematic of a planar monopod model.

the system is about 16 kg. For a fixed configuration of the leg relative to the point mass, the non-zero elements of the joint velocity vector consist only of the forward velocity of the point mass and its vertical velocity, which can be related to the running height, as for a Raibert-type controller [103].

Figure 5.8 shows three different touchdown scenarios for a single configuration of the leg design. The velocity vector drawn at the point mass is equivalent to the change in foot velocity at impact because the position of the foot is held constant relative to the point mass. The generalized inertia ellipsoid, degenerating to an ellipse in this planar example, is indicated at the foot. In Figure 5.8(a), velocity is downward at $2.25\frac{m}{s}$, which is equivalent to dropping the point mass from a height of $0.75m$. The kinetic energy loss for this scenario

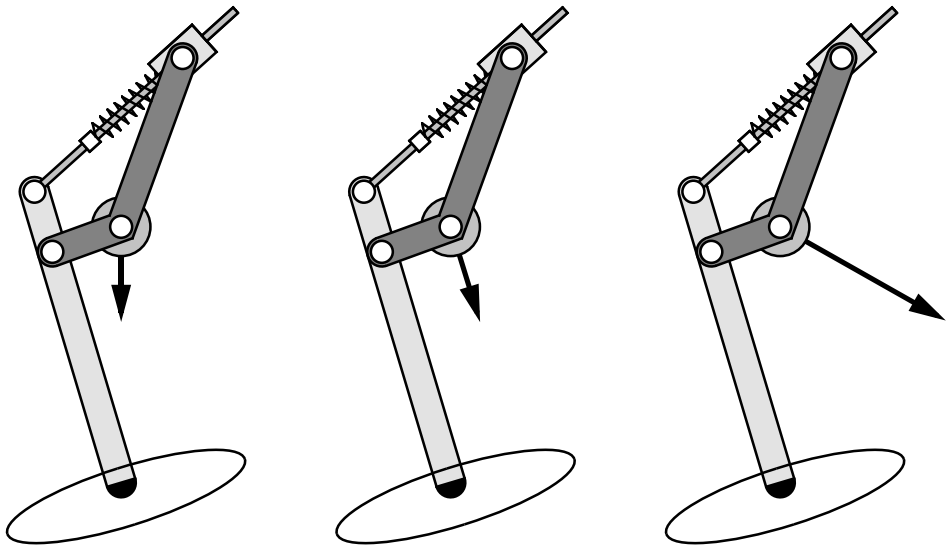

Figure 5.8: Three touchdown scenarios for an articulated leg design. The vector in each sketch indicates the velocity at touchdown of the point mass from which it originates. Since the leg is held fixed relative to the point mass, the vector also indicates the change in velocity of the foot at impact. The GIE is drawn at each foot. The percentage kinetic energy losses are a) 23.1%, b) 25.2%, and c) 14.0%.

is 23.1%. In Figure 5.8(b), the downward velocity is the same, but a horizontal velocity of $0.7\frac{m}{s}$ is introduced. Note that velocity magnitudes do not affect the percentage kinetic energy loss, but the velocity directions do. For the scenario in Figure 5.8(b), the energy loss is 25.2% and maximal because the change in velocity is directly along the minor axis of the GIE. In Figure 5.8(c), the downward velocity is again the same, but the horizontal velocity is increased to $4\frac{m}{s}$. The energy loss here is only 14.0%, as the change in velocity is approaching the direction of the major axis. These results suggest that the chosen configuration of the design is most suitable for high speed locomotion, but not ideal for any of the touchdown scenarios. In fact for the same downward velocity, the energy loss would be minimal (less than 2%) if the horizontal velocity was $7.23\frac{m}{s}$ in the opposite direction.

More insight can be gained from examining various configurations of the same leg under similar touchdown scenarios. The designer must remember, though, that because the GIE is dependent upon the Jacobian and the inertia matrix, not only do the directions of the principal axes change from one configuration to the next, but the lengths of those axes also change. The two cannot be separated in analysis of the kinetic energy loss.

5.6 Leg Return

In Figure 5.8, the minor axis of the GIE appears to be aligned with what would be the most common direction of foot velocity change for normal locomotion. In other words, the design seems to yield nearly maximal energy losses every time the leg touches down. This orientation of the GIE is actually common to most functional leg designs for reasons that have nothing to do with impact.

Recall that the GIE of the model in Figure 5.8 is computed based on the degrees of freedom of both the trunk and the leg relative to the trunk. The shape of the GIE, however,

is determined entirely by the leg degrees of freedom relative to the trunk. The GIE of the trunk alone would be a sphere since its inertia properties are direction-independent for translation. Considering the GIE of only the leg motion relative to the trunk and returning to Asada's [13] interpretation, the major axis indicates the direction of motion for which kinetic energy is minimum. Since a legged system can expend a large amount of energy in returning a leg to its proper position for the next touchdown, it is optimal for the major axis to be aligned with the direction of leg return motion. Returning to Figure 5.8 with this in mind, one can see that the major axis of the GIE does in fact nearly align with the direction of leg return.

In light of this viewpoint, it is not efficient to simply design a leg in order to minimize kinetic energy loss at impact. Rather, a designer must look at the trade-offs between minimizing impact losses and energy required to return the legs which mirror the trade-offs between the vertical oscillations of the mass center and the stride frequency. The generalized inertia ellipsoid provides a convenient visualization tool for this comparative analysis.

5.7 Summary

The kinetic energy lost in a perfectly plastic collision of a robot with a stationary environment can be expressed in terms of the change in velocity of the end effector, the dynamically consistent generalized inverse of the Jacobian, and the inertia matrix. The general development is particularly useful for analyzing the leg designs of dynamically stable mobile robots where energy loss at a foot impact with the ground is an important design consideration. Unlike previous work, the model presented here is applicable to all types of legs. The generalized inertia ellipsoid provides a visualization tool for evaluating why some leg designs provide for less energy loss than others. Use of the ellipsoid also

indicates that an optimal leg design must balance the relative merits of minimizing impact losses and minimizing the energy required to return the leg.

CHAPTER 6

LEG STIFFNESS AND ARTICULATED LEGS

6.1 Introduction

The preceding chapter provides a means of comparing the impact losses associated with different leg designs to be used for dynamic locomotion. It does not, however, offer any techniques for generating functional leg designs because minimizing impact losses is only one of many considerations in the design process. Leg stiffness is an example of a parameter that is probably even more critical. Alexander [4] has investigated the various compliant structures in the legs of animals that aid in dynamic locomotion, and all legged robots capable of dynamic locomotion have been constructed with some compliance in their legs. The value of leg stiffness ultimately affects the control and stability of the robot. Nanua and Waldron [91] showed through simulation that stable galloping can only be accomplished over a finite range of leg stiffnesses and that chaotic behavior results for stiffnesses outside this range.

This chapter presents a means of selecting the stiffness for a leg design based upon biological data. Furthermore, it presents a simple, kinetostatic analysis of the effective stiffness of articulated legs to aid in the geometric layout of a leg design.

6.2 Background

The telescoping legs of Raibert's [103] monopods, biped, and quadruped all included air springs as their compliant structure. This was a convenient design because the stiffness of the legs could be changed by simply altering the air pressure. Raibert lists the air pressure and corresponding stiffness implemented in each of the robots, but he does not address how these values were selected. This information would be more important in designing a leg with mechanical springs as the compliant structure because the stiffness could not be so easily changed.

Buehler and his colleagues also used telescoping legs in their monopod [101] and quadruped [95] robots, although these designs did feature mechanical springs. For the monopod, the spring stiffness was selected to optimize the amount of energy that could be stored in the spring during the stance phase with an electric motor drive system. The stiffness of the quadruped's legs is not listed in the literature.

Top-level, geometric design of telescoping legs is relatively straightforward. The only significant geometric design parameters are the free length of the leg and its maximum telescoping travel, which is determined in large part by the stiffness. In an articulated leg with several rigid links, though, the length and proportion of each are fundamental geometric parameters, so there are a greater number of design variables. Therefore, more attention must be paid to laying out the leg geometry even without regard to dynamics or detail design.

Lilly [74] employed a scaled version of the pantograph leg mechanism from the Adaptive Suspension Vehicle [118] for his quadruped. This articulated leg was designed to minimize back-drive work in straight, level walking [117] [127] and to maximize the walking envelope [119] for statically stable locomotion. It is not clear that the same design

principles apply equally well for dynamic locomotion. Lilly computed an equivalent stiffness of his leg that included the effects of a shock absorbing spring and compliance in the aluminum links. This stiffness value, however, was not predetermined as a desired design parameter.

Furusho et al. [45] also included compliance in the articulated legs of their quadruped without actually selecting a target value. The compliance in this case was in the belts of the drive system, and the geometric design of the legs was not addressed in the literature. Kimura et al. [73] also failed to discuss the geometric design of their quadruped's articulated legs or to list the stiffnesses of the springs acting across its ankle joints. Similarly, Mennitto and Buehler [86] and De Man et al. [32] [31] neglected to address the geometric designs and stiffnesses of their respective articulated monopods. Even for the simplest of legs, the leaf spring of Brown and Zeglin's bow-legged hopper [22] [136], the design stiffness value is not listed in the literature.

There is surprisingly little detail in the existing literature about how to select an appropriate leg stiffness for a robot capable of dynamic locomotion. Additionally, while a number a robots have successfully implemented articulated leg designs, the corresponding literature does not address the design principles employed to develop even the geometry of these legs. As a result, this chapter turns to biological data to select desired leg stiffness and presents a simple method for designing an articulated leg.

6.3 Biological Data

As referred to in Chapter 4, Farley et al. [34] measured the ground reaction forces of trotting and hopping animals while filming their motion. They modeled each leg or leg-pair of the animals as a single linear spring directly connecting a point mass at the mass center

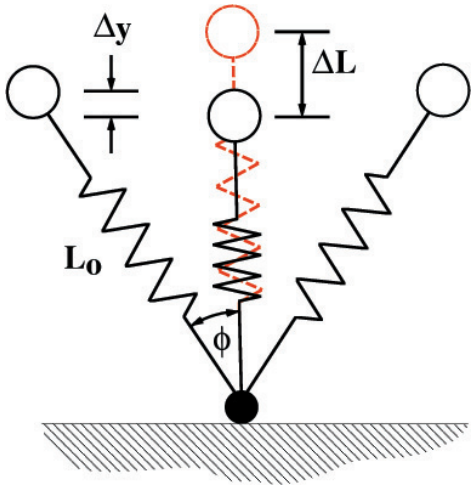

Figure 6.1: Spring-mass model of hopping and trotting, recreated from Farley et al. [34].

to the foot or midpoint between the feet, as shown in Figure 6.1. They defined the stiffness of a "virtual leg" spring, k_{leg}, to be the maximum vertical ground force, F, divided by the compression of the leg spring, ΔL, when it was vertically oriented.

$$k_{leg} = \frac{F}{\Delta L}. \tag{6.1}$$

For the compression calculation, the "free length" of the leg spring, L_o, was defined to be its length at the time of touchdown. For the trotting animals, it was the average of the front and hind leg lengths at touchdown.

Recalling that the legs are employed in diagonal pairs in the trot, the k_{leg} calculated for trotting quadrupeds is actually the effective stiffness of two individual legs acting in parallel. The results of the study indicate that a quadruped's virtual leg stiffness remains essentially constant over a range of speeds and that the stiffness can be predicted by an exponential function of body mass,

$$k_{leg} = 0.715m^{0.67}, \tag{6.2}$$

where m is the mass in kg, and k_{leg} has units of $\frac{kN}{m}$. Equation 6.2 is the result of substituting into Equation 6.1 the following functions relating peak leg force in N and peak leg spring compression in m to body mass in kg.

$$F = 30.1m^{0.97}, \tag{6.3}$$

$$\Delta L = 0.0428m^{0.3}. \tag{6.4}$$

Equation 6.3 suggests that the peak force in the leg-pair is almost directly proportional to body mass and is slightly less than three times the body weight. As discussed in Chapter 2, the front legs generally exert larger forces in the vertical direction than the hind legs do. Therefore, the peak individual leg force is not simply one half of the measured peak leg-pair force because the distribution of load between the legs is unequal. Similarly, the individual leg stiffness may not be one half of k_{leg} for a number of reasons. First, it is possible that the front and hind legs have different stiffnesses. Secondly, the front and hind legs likely rotate through different angles during the stance phase, so their respective changes in length are likely unequal. Finally, the peak ground reaction force occurs when the body reaches its minimum elevation, which does not necessary correspond to the maximum compression of either or both legs.

Taking these factors into account, the magnitudes of individual leg forces are examined to calculate an approximate individual leg stiffness. Jayes and Alexander [69] estimated the peak individual leg forces of galloping greyhounds to average 2.25 times the body weight. Bryant et al. [23] later actually measured the peak individual leg forces of three galloping dogs and found the average peak individual leg force for several runs of all three dogs to be 2.13 times the body weight. Admittedly, this data was recorded for galloping, a gait that

is in many ways unlike trotting, for which Farley et al. [34] recorded their data. The leg forces generated in each gait, though, have been shown to be similar.

Rubin and Lanyon [107] measured the peak bone strains in the legs of dogs and horses to be nearly the same at the highest trotting and galloping speeds. Biewener and Taylor [17] measured similar behavior in goats, and Taylor [125] went on to propose that animals develop similar muscle stresses at their preferred speeds within each gait. These studies indicate that peak individual leg forces may be the same at equivalent speeds within the trot and gallop.

Taking the peak individual leg force to be 2.1 times the body weight and the peak paired leg force to be 3 times the body weight, a reasonable approximation for the individual leg stiffness, k, is,

$$k = \frac{2.1}{3} k_{leg}, \tag{6.5}$$

or substituting from Equation 6.2 to achieve a single expression in terms of body mass,

$$k = 0.5 m^{0.67}, \tag{6.6}$$

where again, k has units of $\frac{kN}{m}$, and m has units of kg.

6.4 Stiffness for Mechanical Legs

A logical starting point for selecting the leg stiffness of a robotic quadruped is the leg stiffness of a biological quadruped having the same mass. Given the projected mass of the robot, Equation 6.6 offers a design value of leg stiffness that should lead to good performance. At the very least, it provides a meaningful initial parameter that can be evaluated through simulation or experimental testing.

Knowing the desired stiffness of a telescoping leg, the detail design can be directly pursued since it mimics the virtual leg spring model from which the stiffness was calculated. For an articulated leg, though, more is involved in laying out the geometry of the design.

6.4.1 Articulated Leg Design

As discussed in Chapter 3, Alexander's [3] force plate studies of animals showed that the line of action of the leg force passes nearly through the shoulder/hip joint of the leg. For a telescoping leg, the force passes directly through the corresponding shoulder/hip. To achieve similar results with an articulated leg, it is attached to the body at a single shoulder/hip revolute joint, as shown in Figure 6.2. Ignoring dynamic effects and assuming that the actuators exert no torque about the shoulder/hip during stance, a static moment balance about the joint requires that the ground reaction force passes directly from the foot through the joint because it is the only external load acting on the system. With this simplified analysis, the direction of the ground reaction force is known for all positions of

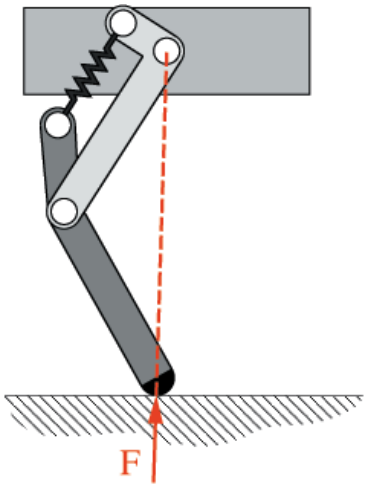

Figure 6.2: The ground reaction force passes through the shoulder/hip joint when the leg is attached to the body by a single revolute joint.

the leg.

With the force passing through the shoulder/hip joint, the articulated leg can be replaced with a virtual leg spring as in the model of Farley et al. [34]. This is shown in Figure 6.3. The virtual leg spring has a non-linear stiffness such that it exerts the same force on the body that the articulated leg does for each virtual leg compression corresponding to an equivalent flexing of the knee joint. Determining the equivalent motion of the articulated leg is more difficult if an ankle joint is also present. Since the leg developed in this work does not include an ankle joint, that case is not considered. With the virtual leg spring acting across the knee joint, it is relatively straightforward to design an articulated leg with an effective stiffness equal to the desired value calculated from Equation 6.6.

As discussed in Section 6.3, the maximum individual leg force is assumed to be 2.1 times the weight of the robot. For the desired effective leg stiffness calculated in Equation 6.6, the maximum expected compression of the virtual leg spring in m, ΔL_{max}, can then be calculated,

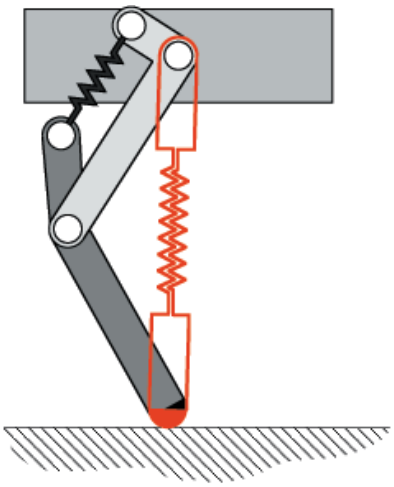

Figure 6.3: An articulated leg can be replaced with a virtual leg spring having a non-linear stiffness.

$$\Delta L_{max} = \frac{F_{max}}{k} = 0.041 m^{0.33}. \tag{6.7}$$

Without an ankle joint, the primary compliant structure in the leg is typically placed across the knee joint in order to store elastic energy during stance. A static moment balance about the knee joint at its maximum expected flexion expresses the force or torque of the compliant structure in terms of the maximum leg force. From here, the required stiffness of the compliant structure can be easily calculated. Independent of the desired effective leg stiffness and expected virtual leg compression, three parameters affect the final design of the compliant structure: the length of the thigh, the length of the shank, and the relative angle between the thigh and shank when the knee is maximally flexed.

The formulation in this section has been developed in rather general terms to highlight that it can be applied to any articulated leg without an ankle joint. The form of the compliance in the leg does not matter provided it acts across the knee joint. The following section details the application of this technique to the design of a leg with mechanical extension springs. Schmiedeler et al. [115] provide another example of the technique as it was employed to develop a preliminary leg design.

6.4.2 Example of Articulated Leg Design

In this work, the projected mass of the galloping machine was 68 kg, roughly that of a large goat, so the desired effective leg stiffness was calculated from Equation 6.6 to be 8.448 $\frac{kN}{m}$. The maximum expected compression of the virtual leg spring was calculated from Equation 6.7 to be 0.165 m. Mechanical extension springs were selected for the compliant structure in the leg to avoid dealing with the buckling of compression springs. Torsional springs were also rejected after analysis showed that they would not produce the desired stiffening behavior of the leg. This is explained in more detail later in this section.

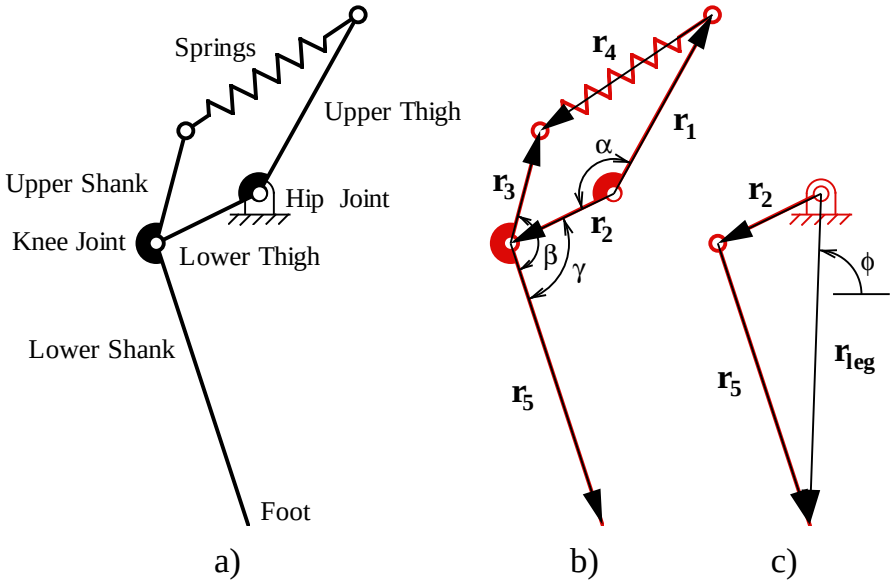

Figure 6.4: Schematic of the leg configuration with vector notation for the actual leg and the virtual leg spring.

In order for the extension springs to act across the knee joint, they must have a connection to both the shank and the thigh. For this purpose, the shank and thigh designs were both considered as bent, rigid links, with the bend in the shank coinciding with the knee joint and the bend in the thigh coinciding with the hip joint. Figure 6.4 is a schematic of the leg configuration labeled with the six parameters that define the geometry of these two links: the lengths of the upper thigh, lower thigh, upper shank, and lower shank and the internal angles of the thigh and shank. It shows the thigh's connection to the body as a grounded revolute joint because only the motion of the leg relative to the body is of interest. Including the relative angle between the thigh and shank when the knee is maximally flexed, the leg has seven design parameters. They are listed in Table 6.1.

Because the required calculations were relatively few and simple, no elegant search techniques were employed to arrive at the final design. Rather, a somewhat exhaustive

Design Parameter	Kinematic Quantity	Minimum	Maximum	Units
Upper Thigh Length	r_1	0.0	0.25	m
Lower Thigh Length	r_2	0.2	0.5	m
Upper Shank Length	r_3	0.05	0.16	m
Lower Shank Length	r_5	0.2	0.5	m
Internal Thigh Angle	α	50	100	$deg.$
Internal Shank Angle	β	150	180	$deg.$
Minimum Thigh-Shank Angle	γ	50	100	$deg.$

Table 6.1: Geometric design parameters of the leg.

search of the practical design space spanned by these seven parameters was conducted through parallel processing with a number of computers. The ranges of values for the design parameters given in Table 6.1 were established largely by intuition. The upper thigh and shank were limited to shorter lengths to minimize the mass of the final design since these segments serve only as connections to the springs. The ranges for the lower thigh and shank were selected to achieve a leg length close to 0.66 m, the hind leg length of the goat studied by Pandy et al. [94]. The internal thigh and shank angle ranges were relatively small because preliminary analysis indicated that good designs could not be found outside them. The fact that the final design values do not fall on the boundaries of these ranges confirms that the ranges were acceptably large. Finally, the relative angle between the thigh and shank at maximum knee flexion was constrained to be large enough that the leg would not be folded over on top of itself. The increment for the linear parameters was 0.010 m, and the increment for the angular parameter was 10 degrees.

Referring to Figure 6.4(b), the closed loop kinematic equation for the leg mechanism is,

$$\mathbf{r}_1 + \mathbf{r}_4 = \mathbf{r}_2 + \mathbf{r}_3. \tag{6.8}$$

Each bold face $\mathbf{r}_i$ represents a vector of magnitude r_i at an angle of θ_i. For the evaluation of each potential design, θ_1 can be chosen arbitrarily because rotation of the entire leg mechanism about the hip joint does not affect the subsequent analysis. θ_2 is then defined by α and θ_1. Similarly, θ_5 is defined by γ and θ_2 in order to place the leg in a configuration with the knee maximally flexed, and θ_3 is defined by θ_5 and β. r_1, r_2, r_3, and r_5 are all unique to each design. Finally, r_4 and θ_4 are found by solving the kinematic loop equations as detailed by Waldron and Kinzel [128].

$$r_4 = \sqrt{A^2 + B^2 + r_1^2 - 2Ar_1\cos\theta_1 - 2Br_1\sin\theta_1}, \tag{6.9}$$

$$\theta_4 = \tan^{-1}\left[\frac{B - r_1\sin\theta_1}{A - r_1\cos\theta_1}\right], \tag{6.10}$$

where,

$$A = r_2\cos\theta_2 + r_3\cos\theta_3, \tag{6.11}$$

and

$$B = r_2\sin\theta_2 + r_3\sin\theta_3. \tag{6.12}$$

Referring to Figure 6.4(c), the length and angle of the virtual leg spring can be calculated through simple trigonometry,

$$r_{leg} = \sqrt{r_2^2 + r_5^2 + 2r_2r_5\cos(\theta_2 - \theta_5)}, \tag{6.13}$$

$$\phi = \tan^{-1}\left[\frac{-r_2\sin\theta_2 - r_5\sin\theta_5}{-r_2\cos\theta_2 - r_5\cos\theta_5}\right]. \tag{6.14}$$

The negative signs are intentionally retained in Equation 6.14 to eliminate the quadrant ambiguity of the $\tan^{-1}$ function by considering the signs of the numerator and denominator

individually. The maximum ground force, F_{ground}, is to be 2.1 times the body weight and is parallel to the $\mathbf{r}_{leg}$ vector. Recognizing that its direction is parallel to the $\mathbf{r}_4$ vector, the required force in the spring, F_{spring}, can be calculated through a static moment balance on the shank about the knee joint,

$$F_{spring} = \frac{F_{ground} r_5 \sin(\theta_5 - \phi)}{r_3 \sin(\theta_3 - \theta_4)}. \tag{6.15}$$

In order to calculate the stiffness of the springs, k_{spring}, necessary to generate this spring force, the length r_4 when the leg is at rest, referred to as r_{4i}, must be calculated. At the beginning of this section, the maximum compression of the virtual leg spring was determined to be 0.165 m. The rest length of the virtual leg spring, r_{rest}, is given by,

$$r_{rest} = r_{leg} + 0.165. \tag{6.16}$$

Knowing this value, the relative angle between the thigh and shank when the leg is at rest can be computed with the law of cosines,

$$\gamma_{rest} = \cos^{-1}\left[\frac{r_2^2 + r_5^2 - r_{rest}^2}{2 r_2 r_5}\right]. \tag{6.17}$$

Since only the shank moves when the knee flexes, θ_2 does not change, and the rest value of θ_5 can be found once γ_{rest} is known. From there, the corresponding value of θ_3 can be calculated, and finally, r_{4i} can be computed by substituting the newly calculated values into Equation 6.9. Ultimately, this leads to the required spring stiffness,

$$k_{spring} = \frac{F_{spring}}{r_4 - r_{4i}}. \tag{6.18}$$

After the calculations were made for each combination of the design parameters, the resulting design was evaluated according to a number of criteria to determine its viability. First, all designs in which r_{rest} was less than 0.55 m were rejected because the change in

length of the virtual leg spring was too large a percentage of its free length. Blickhan and Full [20] found that in the biological world, the compression of the virtual leg spring rarely exceeds 30% of the spring's free length. Secondly, all designs in which the transmission angle between any two links in the leg mechanism was less than 10 degrees were rejected. Finally, designs requiring unrealistic spring characteristics were rejected.

It was quickly discovered that a single steel extension spring would not be able to meet all of the design requirements for any reasonably sized leg. The spring requirements were four-fold. First, the peak force of the spring had to be larger than the maximum calculated spring force. Secondly, the maximum extension of the spring had to be greater than the calculated extension. Thirdly, the spring constant had to be larger that the calculated spring constant. Finally, and possibly most limiting, the solid length of the spring had to be less than the minimum calculated length of r_4. In order to meet these four criteria, the leg was designed to include four steel extension springs operating in parallel. All designs that required spring performance beyond the strength of steel extension springs 0.030 m in diameter were rejected to prevent the leg from becoming excessively wide.

Once all of the viable leg designs within the design space were found, they were compared based upon the combined total of their link lengths. The designs having smaller length sums were preferred as they would likely weigh less. The designs were also qualitatively compared by examining how the stiffness of the virtual leg spring changed as it compressed. This consideration is discussed in more detail in the following section.

The final design parameters selected for the quadruped are listed in Table 6.2. The corresponding extension spring has a spring constant of 6.455 $\frac{kN}{m}$. To achieve a virtual leg compression of 0.165 m, this design requires a ground force of 2.12 times the body weight, so the effective virtual leg stiffness is actually 8.563 $\frac{kN}{m}$, slightly higher than the design

Design Parameter	Kinematic Quantity	Value	Units
Upper Thigh Length	r_1	0.09	m
Lower Thigh Length	r_2	0.35	m
Upper Shank Length	r_3	0.16	m
Lower Shank Length	r_5	0.35	m
Internal Thigh Angle	α	90	$deg.$
Internal Shank Angle	β	155	$deg.$
Minimum Thigh-Shank Angle	γ	90	$deg.$

Table 6.2: Geometric parameters of the final leg design.

value. The leg is capable of withstanding larger ground reaction forces because the springs are not fully extended when the virtual leg compression is 0.165 m. Therefore, the leg has been designed with a factor of safety so that the performance limit is not reached even at the predicted peak loading.

6.4.3 Stiffening Legs

The tendons of biological quadrupeds are stiffening structures [4]. As load and deflection increase, the corresponding stiffness also increases. This behavior is also desirable for the stiffness of the quadruped's virtual leg spring. The spring should be fairly soft when the foot touches down to limit the impact, but it should stiffen with increased deflection to generate significant force before the leg is folded over on itself. The viable designs generated as described in the previous section were examined to determine their stiffness characteristics. Again, the stiffness was calculated by a static force analysis of the leg throughout its range of motion. Almost all of the designs yielded virtual leg springs that stiffened initially with deflection, but many of them reached a maximum stiffness value and then showed a

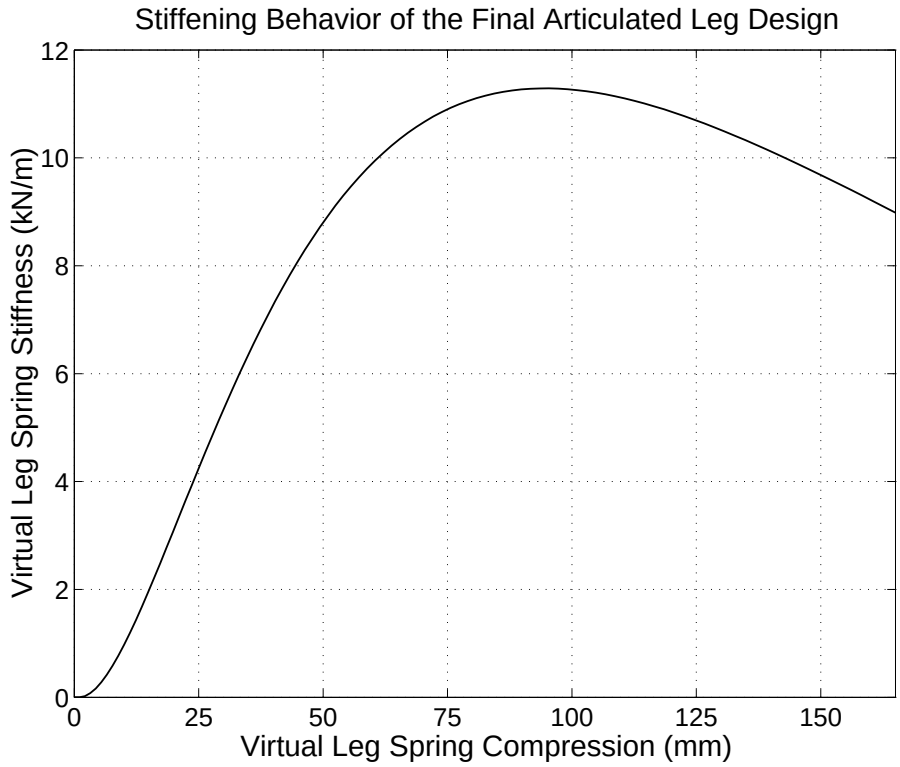

Figure 6.5: Stiffness curve for the final leg design.

marked drop in stiffness. These designs were rejected to avoid softening of the leg when its force is maximum.

The stiffness of the final design is shown in Figure 6.5. This graph shows the stiffness over the design range of motion for the leg, although greater compression of the virtual leg spring is possible. The shape of the graph very clearly indicates the desired stiffening of the virtual leg spring. The stiffness is nearly zero when the leg touches down at zero compression, so the stiffness has only a small effect on the impact losses. Following touchdown, the stiffness increases sharply as the leg spring compresses and the leg force increases. The slight drop in stiffness following its peak is not large enough to be of concern. In fact, after

about 62 millimeters of leg compression, the stiffness remains relatively constant, fluctuating by only +/- 11%. This behavior is desirable in light of Farley et al.'s [34] result that leg stiffness in biological quadrupeds remains relatively constant over a range of speed. With the current leg design, larger forces would be generated at higher speeds by compressing the leg more, but the stiffness would remain nearly constant provided the compression was greater than 62 millimeters.

6.5 Summary

Since the descriptions of legged robots in the literature offer little insight in selecting leg compliance, a reasonable design compliance is one that matches that of biological quadrupeds having the same mass as the robot. The geometric design of telescoping legs having the desired compliance is relatively straightforward, and some articulated legs can be designed with a desired compliance through simple, kinetostatic analysis. This method was employed to geometrically design the prototype leg described in detail in the following chapter. Marhefka's [79] simulation results for a model of the prototype leg and the experimental results presented in Chapter 8 indicate that the methods described in this chapter are suitable for designing a leg with high-speed motion capability.

CHAPTER 7

DETAIL DESIGN OF AN ARTICULATED LEG

7.1 Introduction

In the preceding chapter, the planar geometry of the final leg design was selected to match the desired effective leg stiffness. This chapter details the manifestation of that planar geometry in a prototype leg and the design of a test apparatus for evaluating the leg's performance. The background of the project and the proposed control method are discussed to highlight their respective impacts on the design. The component assemblies of the leg are each described in this chapter, but a full list of mechanical components and a set of assembly instructions are included in Appendix B.

7.2 Background

The prototype leg shown in Figure 7.1 was developed to evaluate its viability as the leg design for a quadruped robot that would be capable of galloping. Schmiedeler and Waldron [112] listed the initial design specifications for the quadruped and some early design concepts for the leg. The intended purpose of the quadruped was to investigate the complex dynamics of galloping without the additional difficulties associated with locomotion over uneven terrain. As such, experiments with the machine were to be confined to a laboratory setting. The size of the quadruped, alluded to in Chapter 6, was to approximate that of

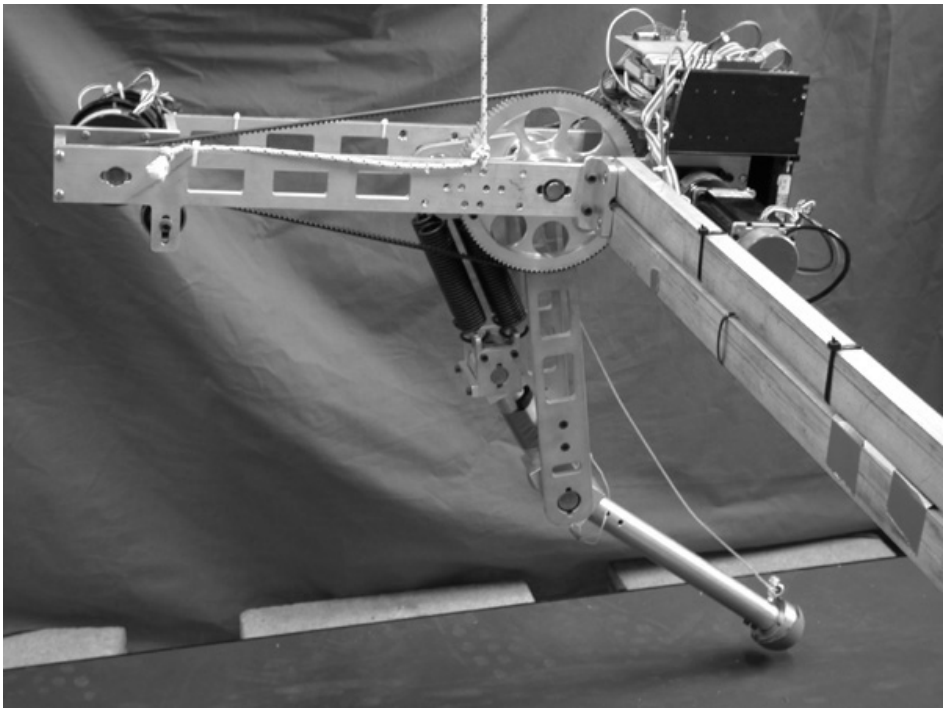

Figure 7.1: Prototype leg attached to the boom.

a large goat since this was the largest size considered reasonable for laboratory use. The choice was also convenient in light of the available research dealing with dynamic locomotion of goats [94]. The machine was to have a mass of about 68 kg, a length of roughly 1.5 m, and a standing shoulder/hip height of approximately 0.7 m. These dimensions were all considered in arriving at the final geometric design dimensions listed in Chapter 6.

Because an umbilical cable providing off-board power would not only limit the range of motion but also disturb the motion in an unpredictable manner, the quadruped was envisioned to carry its own power source on board. Hydraulic and pneumatic actuation systems were not considered practical options within the size and weight restrictions, so electrical actuation with brushless DC servomotors was selected. This actuation scheme led in large part to the choice of an articulated rather than telescoping leg design. Telescoping legs are

convenient with hydraulic actuation, as demonstrated by Raibert's monopods, biped, and quadruped [103]. With electrical actuation, though, the design of a telescoping leg, like Rad et al.'s [101] monopod, can become much more difficult. Furthermore, articulated legs should be able to take advantage of the superior frictional characteristics of revolute joints, particularly when driven by the rotary motion of electric motors.

The quadruped's legs were to have three degrees of freedom: abduction/adduction, shoulder/hip rotation, and knee flexion. The abduction/adduction motion was anticipated as a requirement for stabilizing the roll motions of the body, even for straight-line galloping. Raibert [102] found that bounding could be passively stable in pitch, and since galloping is a similar gait, passive pitch stability may also characterize optimal galloping. As a result, the shoulder/hip actuation was intended to be used only in returning the leg and not during stance to avoid disturbing the body's natural pitch motion. Nonetheless, the design was to be capable of exerting some shoulder/hip torque during stance if necessary. No ankle joint was included because most quadrupeds do not use their ankles to increase leg thrust the way that many bipedal runners do. In fact, a goat's shoulders and hips dominate in walking, while the knees become more important in running [94]. As discussed in Chapter 6, the direction of the leg force was to pass from the foot through the shoulder/hip joint, and the compliant structure in the leg was to act across the knee joint.

The original design concept was to place the compliant structure in series with the knee actuator to mimic the series elastic component of biological muscles [62]. Pratt and Williamson [99] used this configuration successfully to improve shock tolerance, lower reflected inertia, and stabilize force control with electric motors. Rad et al. [101] also implemented the idea in the telescoping leg of their monopod. In each case, an electric motor drove a ballscrew in series with mechanical compression springs. Figure 7.2 is a

Figure 7.2: Solid model of an early quadruped design with legs having mechanical extension springs in series with ballscrews.

solid model of a quadruped with the original articulated leg design using a ballscrew and mechanical extension springs. This design was eventually discarded because the legs were simply too heavy. With the knee actuating motor located inside the leg relatively far from the shoulder/hip joint, the leg's moment of inertia about the joint was very large. As a result, the leg's natural frequency was relatively low, and high torque was required to drive it in the return phase. Marhefka's [79] dynamic simulation work was instrumental in this discovery. To address the problem, a new design inspired by Brown and Zeglin's bow-legged hopper [22] [136] and DeMan et al.'s OLIE [32] [31] was developed. This is the design pictured in Figure 7.1 and shown in the solid model of the quadruped in Figure 7.3.

7.3 Control Overview

All of the potential leg designs for the quadruped galloping machine were developed to operate with a Raibert-type controller [103]. This approach treats the forward speed, hopping height, and body attitude as three separate control problems. It controls forward

Figure 7.3: Solid model of the quadruped design with legs matching the existing prototype leg.

speed with the placement of the foot relative to the shoulder/hip joint and hopping height with energy injected into the system during the stance phase. Body attitude is controlled with shoulder/hip torque exerted during stance, but is not pertinent to the prototype leg control. The boom mechanism for testing the leg constrains the leg frame to remain parallel to the ground.

Marhefka [79] discussed the implementation of a Raibert-type controller in more detail and proposed fuzzy control as an alternative. For the purposes of leg design, though, the separation of the forward speed and hopping height control has the greatest significance. In order to place the foot for speed control, the shoulder/hip joint is servoed to a prescribed angle prior to touchdown. Typically, the desired joint velocity is zero at touchdown, although the advantage of retracting the legs is addressed in Chapter 5. During stance, the shoulder/hip joint is unactuated since body attitude need not be controlled.

Raibert injected energy into his robots to control hopping height by increasing the pressure in the air-cylinder of a leg while the foot was on the ground. Rad et al. [101] achieved the same effect with their monopod by driving a ballscrew to compress a spring during

stance. For the articulated prototype leg, energy is stored in the leg springs during the return phase and then released during stance, as it was in the bow-legged hopper [22] [136]. In return, the knee is flexed to extend the leg springs. During stance, the ground force on the leg causes even more knee flexion, the actuator is released, and the stored elastic energy is injected as the springs compress to their rest length. This method reduces the power requirement of the knee actuator. First, the duration of the return phase is longer than that of the stance phase, so more time is allowed for storing the energy in the springs. Secondly, the leg is unloaded in the return phase, so the spring force is lower than during stance.

Raibert-type control is certainly not the only method applicable to the prototype leg. It is, however, the method that inspired the design. The shoulder/hip joint actuator was selected and sized to move the leg to a fixed position prior to touchdown, and the knee actuator was selected and sized to store elastic energy in the springs for release during stance. The structure of the leg was developed to be consistent with this actuation scheme.

7.4 Structural Overview

The prototype leg shown in Figure 7.1 is composed of four primary assemblies: thigh, shank, springs, and frame. The thigh is the upper leg, the shank is the lower leg, and the springs connect the two to form a closed-loop kinematic chain. As stated in the previous chapter, the springs act across the most distal joint of the leg, the knee, so that elastic energy is stored in them with each foot impact on the ground. The thigh is connected to the frame by the revolute shoulder/hip joint. The frame houses the two electric motors for actuation and connects the leg to the boom mechanism. The motor at the rear of the frame actuates the shoulder/hip joint through a timing belt drive. The shoulder/hip joint is located closer to the front of the frame to allow clearance for the springs as the leg rotates backwards

through the frame during stance. The placement of the motor at the rear of the frame takes advantage of the longer distance to achieve greater belt wrap on the pulleys.

The motor at the front of the frame actuates the knee joint through a cable drive, with the cable shown slack in Figure 7.1. The remote actuation of the knee removes the motor from the rotating portion of the leg to reduce the leg's moment of inertia and thus, the torque required to return it. Ultimately, this reduces the power requirement of the shoulder/hip joint motor. The cable is fixed at one end to the shank near the foot and at the other end to a pulley driven by the knee joint motor. In between, the cable passes over an idler pulley on the shoulder/hip axis so that the knee flexion is decoupled from the shoulder/hip rotation as much as possible.

Ideally, the shoulder/hip rotation and knee flexion should be completely decoupled, but this is not possible because the idler pulley must have a non-zero diameter. Still, the placement of the knee actuator at the front of the frame uses what little coupling there is to an advantage. As the leg rotates forward in preparation for the next touchdown, the cable wraps farther around the idler pulley. The additional cable wrap causes some knee flexion, so energy is stored in the springs. In this way, driving the shoulder/hip motor actually helps to add energy to the system. When the leg rotates backwards freely during stance, the cable wrap on the idler pulley is reduced, and the additional slack allows the springs to compress again to their rest length.

The four primary assemblies are described in the following sections. Wherever applicable, dimensions are given in English units because all of the machined parts were made using English units. Unless otherwise stated, all of the machined parts are aluminum with the exception of the shafts, which are all steel. The component parts of and the instructions for each assembly are listed separately in Appendix B.

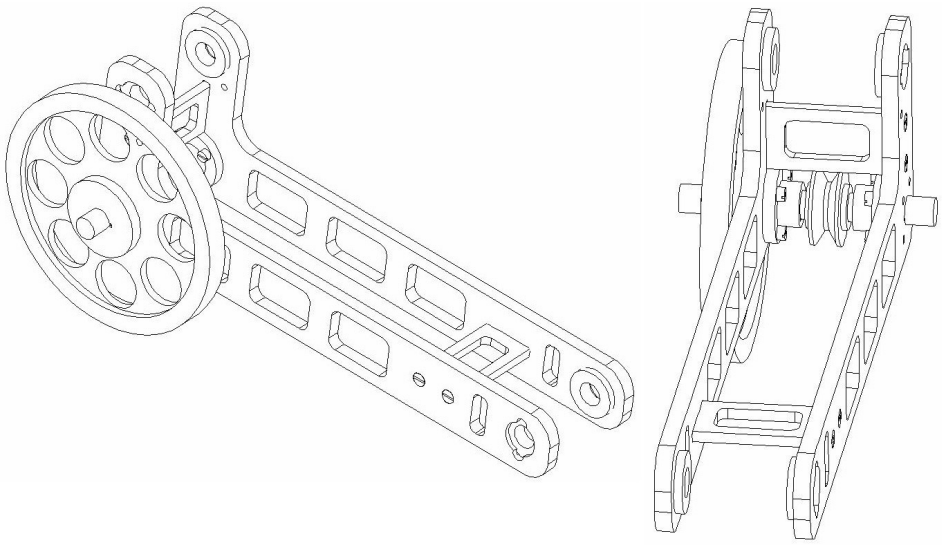

Figure 7.4: Two views of the solid model of the thigh assembly.

7.4.1 Thigh

The thigh assembly shown in Figure 7.4 contains two L-shaped structural members that match the thigh dimensions chosen in Chapter 6 and that are connected by two cross braces, one in each arm of the L. The structural members are .375 inches thick so that ball bearings can be pressed directly into them. The cross braces are .25 inches thick because they are tapped for #10 screws. All of these components have holes machined in them to reduce weight, so it is clear that the thicknesses are not the minimum required to support the predicted loads. Future work with finite element analysis could likely help identify areas for additional material removal that would further reduce weight without weakening the assembly.

The thigh is divided into the two structural members so that the shank and spring assemblies can be sandwiched between the two. The shank assembly is attached between the ball bearings pressed into the long arm of the thigh assembly, or the lower thigh. This is

the location of the knee joint. One end of the spring assembly is attached between the ball bearings pressed into the shorter arm, or the upper thigh. The shaft at the intersection of the two arms of the L forms the shoulder/hip axis and is connected to the frame assembly. The shaft is keyed to the structural members, and the round flanges bolted to the interior side of each serve only to increase the effective key length. The large timing belt pulley is both keyed to the same shaft and bolted to one of the structural members because it carries the torque that swings the entire leg about the shoulder/hip joint.

Between the two flanges, the shoulder/hip shaft is not keyed, and the idler pulley is free to rotate on bronze bushings relative to it. The diameter of the idler pulley is 1 inch and was minimized in order to minimize the coupling of the shoulder/hip rotation and knee flexion caused by the variable wrap of the cable around the idler. The diameter could not be significantly smaller because the shoulder/hip shaft is .625 inches in diameter itself. This shaft is heavily loaded because it transfers all of the leg force from the thigh to the frame during stance and supports the full cable force during the return phase.

7.4.2 Shank

The shank assembly shown in Figure 7.5 contains two round aluminum tubes pressed into a central brace angled at 155^o. The other end of the shorter tube is pressed into the shank cap to form the upper shank, and the longer tube connects to the foot subassembly to form the lower shank. The corresponding lengths match the shank dimensions chosen in Chapter 6. The central brace and shank cap both have shafts pressed through them for bearing seats. The shaft of the central brace is seated within the bearings of the thigh assembly to form the knee joint, and the shaft in the shank cap provides the connection to the spring assembly.

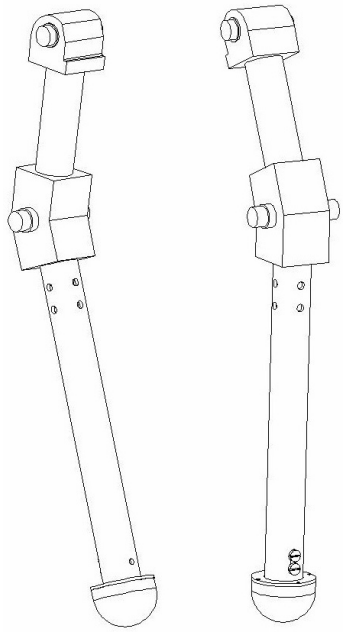

Figure 7.5: Two views of the solid model of the shank assembly.

The shank is loaded primarily in bending, which is why tubing was selected to form its principle structure. The tubing is round because this allowed for easier machining of the bores in the central brace and shank cap than would rectangular or square tubing. It has an outside diameter of 1.25 inches and a wall thickness of .125 inches. Smaller diameter tube of equivalent bending strength weighs more per unit length, while larger diameter tube would have increased the width of the leg, which would have increased weight elsewhere.

In Figure 7.1, a rubber pad is taped to the tube of the upper shank to cushion the impact between the shank and thigh assemblies when the springs reach their rest length. This pad is not shown in Figure 7.5. The cross brace in the lower thigh contacts the pad at the motion limit to prevent the spring assembly from rotating through in the opposite direction and to prevent the impact from snapping the cable. Just above the foot in the solid model on the left side of Figure 7.5 is a hole for an eyebolt to which the cable is tied. The hole is located

as close to the foot as possible because the static force analysis in Chapter 6 indicated that the mechanical advantage of the knee actuating motor is better with the cable connection at the end of the lower shank.

Foot Subassembly

The foot subassembly shown in Figure 7.6 serves two functions in the leg. First, it bears the leg to the ground with a relatively large coefficient of friction such that it does not slip during the stance phase. The aluminum hemispherical foot shown in Figure 7.6 is covered with a racquetball for this purpose, as seen in Figure 7.1. Any similar rubber-like covering could be used, but a racquetball is convenient because its inner diameter is roughly equal to the foot diameter. In this way, the racquetball forms an air-tight seal around the foot which

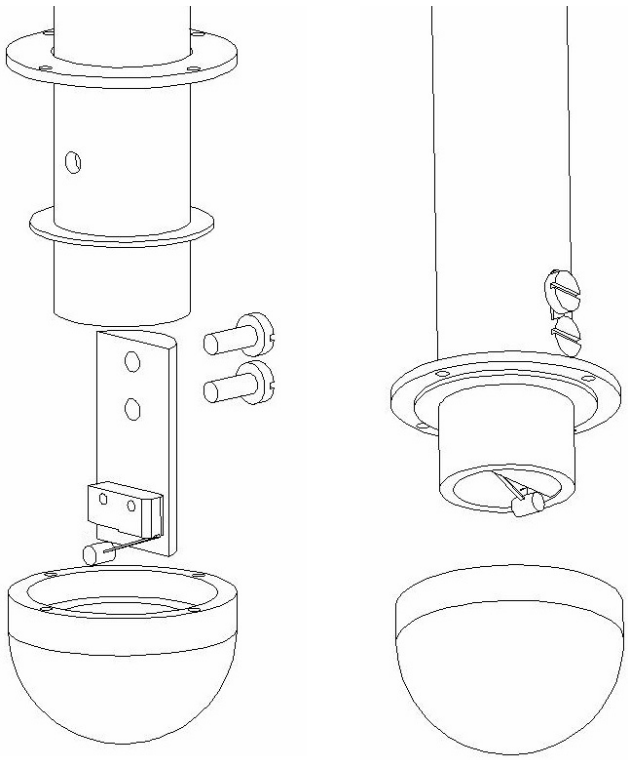

Figure 7.6: Two exploded views of the solid model of the foot subassembly.

holds it in place without any adhesive. Furthermore, racquetballs are easy to find and can be replaced inexpensively.

The second purpose of the foot is to sense when the leg is in contact with the ground. As shown in Figure 7.6, this is accomplished with a microswitch that is triggered when the foot touches down. The microswitch is bolted to the round tube of the lower shank by means of a hemi-cylindrical insert. The bolts pass through a slot in the tube that allows for adjustment of the microswitch's position and thus, the sensitivity of contact detection. For all positions, the body of the switch is completely inside the tube such that during touchdown, the base of the bore in the hemispherical foot bears on the end of the tube and not on the switch itself. A plastic bushing pressed into the hemispherical foot is the bearing for the translation needed to trigger the switch.

A wave spring acting between the hemispherical foot and a retaining ring fixed in the lower shank ensures that the switch is not triggered when the foot is not in contact with the ground. The hemispherical foot is bolted to a ring-like cap that prevents it from falling off the shank. The wires of the microswitch are fed up the tube of the lower shank and out the holes near the central brace that are shown in Figure 7.5. This is a rather simple design for detecting ground contact, but its simplicity may be the explanation for its reliability. In all of the experiments to date with the prototype leg, the microswitch has never failed to detect ground contact.

7.4.3 Springs

The spring assembly shown in Figure 7.7 contains four steel extension springs with components for the connections to the shank and thigh assemblies on either end of them. The spring constant of each spring is 6.455 $\frac{kN}{m}$, and the pertinent dimensions are given in

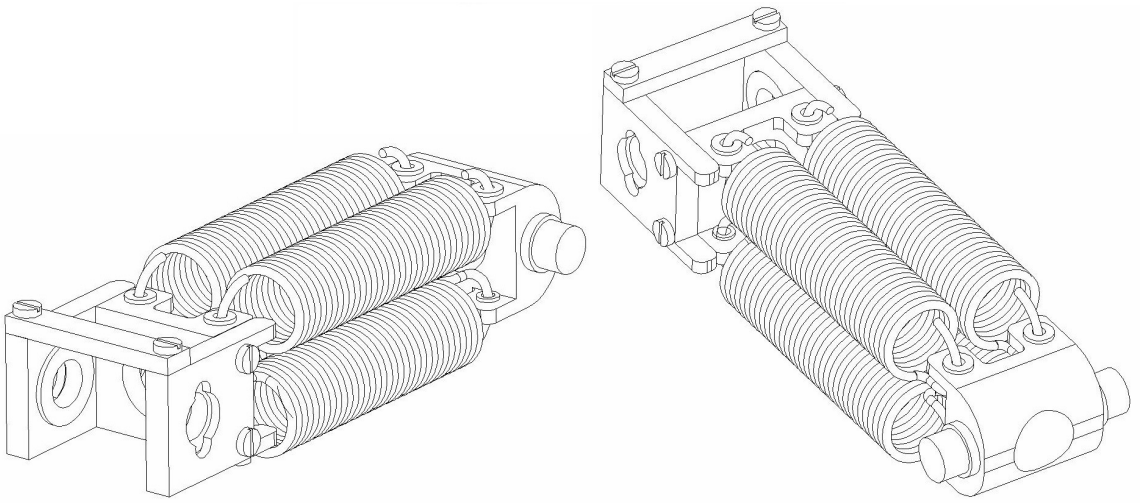

Figure 7.7: Two views of the solid model of the spring assembly.

Appendix B. The connection to the shank is a bolted framework of four aluminum pieces with two ball bearings that seat the assembly on the shaft in the shank cap. The hooks of the extension springs pass through holes in this framework that are lined with bronze bushings to prevent the steel from deforming the aluminum. The same bushings are used in the connection to the thigh assembly, but this connection is simply an aluminum body with a steel shaft pressed through. This shaft is seated in ball bearings within the thigh assembly.

7.4.4 Frame

The frame assembly shown in Figure 7.8 contains the leg frame itself and the actuation systems for both the shoulder/hip and knee joints. The leg frame is composed of six pieces of .375 inch thick aluminum that are bolted together. As in the structural members of the thigh assembly, the thickness allows ball bearings to be directly pressed into the frame plates, and several of them have material removed for weight reduction. Again, further

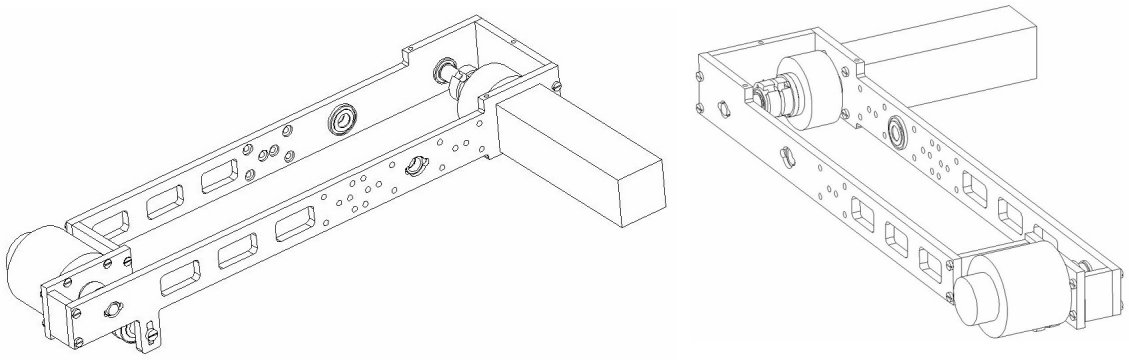

Figure 7.8: Two views of the solid model of the frame assembly.

weight savings could be achieved with the aid of finite element analysis. The bearings for the shoulder/hip shaft are located closer to the front of the frame because the leg rotates back through the frame during stance.

The square motor at the front of the frame assembly is the knee actuator. It drives, by way of an electric clutch, a pulley around which the cable is wrapped to flex the knee and extend the springs. The round motor at the rear of the frame assembly is the shoulder/hip actuator. It drives, by way of a small timing belt pulley and timing belt, the large timing belt pulley in the thigh assembly. These two actuators are discussed in greater detail in the following section.

The most fundamental purpose of the frame assembly is to hold the leg together. Beyond this, though, it also houses the control board and amplifiers for both motors, which are shown in Figure 7.1, but not in Figure 7.8. The boom mechanism is connected to the frame assembly for all experiments. In order to prevent unnecessary torque on the boom, the connection to the frame should coincide with the longitudinal position of the leg's mass center. The connection to the boom was originally designed to be immediately behind the

shoulder/hip shaft because the mass of the amplifiers was not considered in locating the leg's mass center. During the initial experiments, the location of the boom connection far from the actual mass center resulted in undesirable pitching of the leg frame. The problem was corrected by moving the connection to be immediately in front of the shoulder/hip shaft, as is shown in Figure 7.1. The change explains the additional holes that appear in the leg frame in both Figures 7.1 and 7.8.

While the abduction/adduction of the leg is not pertinent to the experiments with the prototype leg, it is pertinent to the design of the leg frame. In the quadruped robot, the leg will be jointed to the body through the frame assembly. The entire frame must rotate relative to the body to achieve the abduction/adduction. The current frame was designed specifically for the one-leg experiments, but it would require only minor modifications to be used in the quadruped.

7.5 Actuator Selection

All of the actuators considered for the prototype leg were brushless DC servomotors with 24 volt windings. The peak current was assumed to be 15 amps for design purposes so that the actuators could be driven with reasonably sized amplifiers and power supplies.

7.5.1 Shoulder/Hip Joint

Marhefka's [79] simulation work indicated that for the prototype leg design to travel at a constant velocity of 5 $\frac{m}{s}$ with a hopping height of .8 m, the shoulder/hip joint actuator must be capable of generating 15 $N \cdot m$ of torque. The peak design torque was taken to be 30 $N \cdot m$ to allow for performance enhancements like running at lower hopping heights and rapid acceleration and to account for potentially greater torque requirements of the quadruped. Within the voltage and current limits, no brushless DC motor was found to meet

the maximum desired torque, so various drive train options were considered. Ultimately, a timing belt drive was selected because it could be backdriven more easily than a gear train during the stance phase of the leg when the joint would be unactuated. Deman et al. [32] [31] employed timing belts to drive both joints of their articulated monopod OLIE.

The final design of the belt drive contains pulleys with 21 and 112 teeth, so the effective gear reduction is 5.33:1. Since motor speed is much greater than what is needed to return the leg, a larger reduction would have allowed for a smaller and lighter motor. The timing belt manufacturer, though, recommended that single-stage drives be limited to a 5:1 reduction. Minimizing the size of the two pulleys is also desirable in order to minimize weight. The 21-tooth pulley was the smallest having a bore large enough for the corresponding motor, and the 112-tooth pulley was machined to reduce its weight. The Hathaway Emoteq HT3003 motor selected as the shoulder/hip actuator has a maximum continuous stall torque of 1.63 $N \cdot m$ and a peak torque of 5.68 $N \cdot m$, so the drive system is capable of generating greater than 8 $N \cdot m$ of torque continuously and greater than 30 $N \cdot m$ for short periods of time.

Ahmadi and Buehler [2] designed their monopod with springs acting across the shoulder/hip joint in order to reduce the energy required to return the leg. Their work was motivated by Gregorio et al.'s [50] finding that their monopod expended half of its total energy just in leg return. Springs acting across the shoulder/hip joint were not included in the prototype articulated leg for simplicity and because a drive system of reasonable size was found. The use of springs across the joint, though, is a subject of future work with the leg.

7.5.2 Knee Joint

The actuation of the knee joint to store energy in the leg springs during return and release it during stance was inspired by the bow-legged hopper [22] [136]. That machine, however, was able to store only a fixed amount of energy in its leg spring for each step. For galloping at various speeds, a quadruped's leg must be able to vary the amount of energy injected into the system from step to step. The drive system for the knee joint was designed to actively control the knee flexion during the return phase by wrapping the cable around a motor-driven pulley.

Marhefka's [79] simulations used a simplified model of the leg that neglected actuator dynamics and the effects of the cable's idler pulley. His work indicated that a cable force of about 900 N would draw the cable in 75 mm to allow the leg to travel at 5 $\frac{m}{s}$ with a hopping height of .8 m. Planar kinetostatic analysis like that described in Chapter 6 yielded very similar results. A cable force of 910 N was found to draw the cable in 72.5 mm, which corresponded to 22.4 J of elastic energy stored in the leg springs. After Marhefka's work was complete, a few dimensions of the leg design were changed, so the kinetostatic analysis was repeated with the altered design to compute the cable force required to store the same amount of energy in the springs. With the new design, 750 N of cable force drew the cable in 74 mm to store 23 J of energy, and this became the target design value.

The pulley around which the cable is wrapped has a 1 inch diameter, so one full revolution corresponds to slightly less than an 80 mm change in cable length. With a smaller diameter pulley, the cable would have wrapped over on top of itself to meet the target design value. A larger pulley diameter would have increased the torque requirement of the driving motor. It would have reduced the speed requirement, but again, motor torque was far more limiting than motor speed. For a cable force of 750 N and a pulley radius of 12.7

mm, the peak torque requirement for the motor was 9.525 $N \cdot m$. Within the voltage and current limitations, no torque motor was found to be capable of such high continuous stall torque. As a result, a more conventional motor with a 10:1 planetary gearbox was selected. The Hathaway Emoteq QB2302 has a maximum continuous stall torque of .98 $N \cdot m$, so with the gear reduction, it surpasses the peak torque design value.

In order to release the energy in the springs during stance, the pulley must be driven in the opposite direction to reach the position of zero cable wrap. Because the duration of stance is so brief, the motor speed is not fast enough to unwrap the cable completely before the knee extends far enough to load the cable again. The result is that the cable bears the spring load and some of the energy stored in the springs is dissipated in backdriving the motor. The analysis of a simple model in Appendix C shows that backdriving the motor absorbs enough of the stored spring energy to significantly reduce the hopping height.

Based on this analysis, an electric clutch was included in the design between the motor and the pulley. When the foot lifts off the ground, the clutch engages, and the motor drives the pulley to draw in the cable. The triggering of the microswitch in the foot at touchdown disengages the clutch so that once the cable is loaded again when the knee extends, the pulley can rotate freely relative to the motor shaft without the large energy losses. The maximum holding torque of the selected clutch is 90 $in \cdot lb$ or 10.169 $N \cdot m$, so it surpasses the designed peak torque. As an alternative to the pulley and clutch combination, a cam design somewhat similar to that of the bow-legged hopper [22] was considered. It offered a number of advantages, but was ultimately rejected because it would have required a motor weighing more than the chosen clutch and motor combined.

Braided, tubular kevlar cord was chosen for the cable because it is flexible and strong. With both the idler and driving pulley having diameters of only 1 inch, flexibility in the

cable is very important. The .125 inch wide cord was tested in a uniaxial tension test machine prior to its use in the prototype leg. In each of two trials, the cord supported more than 270 pounds before breaking at the knots that were tied to attach the cord to the machine. With a pulley radius of .5 inches and a maximum clutch holding torque of 90 $in \cdot lb$, the force on the cord should never exceed 180 lb. During experiments with the leg, the cord did break on a number of occasions, but almost always after many tests and at the pin where it is connected to the driving pulley. This location is a stress concentration because the cord is bent around the pin when not wrapped around the pulley.

7.6 Testing Apparatus

The testing apparatus for the prototype leg is composed of the boom mechanism and the wall mount. The boom mechanism shown in both Figures 7.1 and 7.9 is a parallelogram linkage made of two rectangular aluminum tubes that are 8 feet in length. The mechanism allows the leg to move roughly up and down while its orientation remains constant. The wall mount pictured in Figure 7.9 allows the boom mechanism to rotate about a vertical axis so that the leg can move roughly forward and backward. In this way, the leg's motion is constrained to the surface of a sphere-like primitive while its orientation does not change. The surface is not exactly a sphere because the two axes of rotation are offset rather than intersecting as they would be in a true universal joint. Optical encoders are used to measure the angle of rotation about each axis.

The original boom mechanism design was made of 10 foot lengths of .75 inch square aluminum tubing with a wall thickness of .062 inches. Visual analysis of preliminary experiments indicated that this tube was not strong enough to support the bending loads on

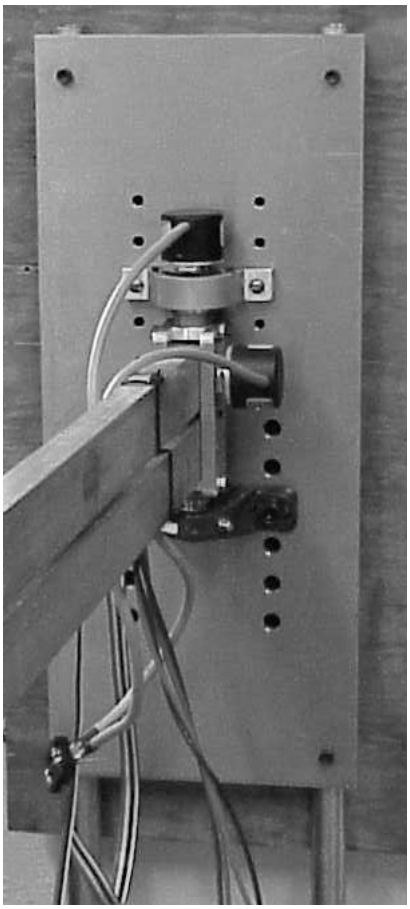

Figure 7.9: Wall mount for the leg with the boom attached.

the boom. The hopping motion caused the tubing to flex about an axis parallel to the longitudinal direction of the leg. The wall thickness of the tubing was increased to .125 inches in the second boom design, and the bending motion was reduced. Because the hopping height of the leg was calculated from the encoder angle of the boom, though, the boom flexibility was still unacceptable. The oscillations of the boom while the leg was in a flight phase made it impossible to accurately determine the hopping height.

The final boom design contains 1.5 x .75 inch rectangular aluminum tube with .125 inch wall thickness and is 8 feet in length. This larger tube's moment of inertia is more than six

times that of the square tube, so if each tube in the boom is modeled as a simply supported beam, the angular displacement at the wall mount should be reduced by the same factor. Similarly, just shortening the boom by two feet should yield an angular displacement less than two thirds that of the longer boom. Combining these two, the new boom was predicted to reduce the angular displacements by a factor of more than 9.5. Experimental data from the encoder showed that oscillation of the boom during the leg's flight phases was negligible with the new boom. The rectangular tubing also strengthened the boom in torsion, as its polar moment of inertia is four times that of the square tubing.

The wall mount is bolted to two steel channels in the wall of the laboratory to ensure a rigid connection. The two vertical tubes in the mount rest on the floor of the laboratory to prevent the steel channels from pulling out of the wall under unexpected loadings. The flat plate of the wall mount has a series of holes to allow the leg to be raised or lowered relative to the ground. The central position corresponds to a horizontal orientation for the boom in the middle of the normal hopping range.

7.7 Leg Orientation

The kinetostatic analysis in Chapter 6 that was used to select the leg geometry is independent of knee flexion direction. It applies equally well for knees that flex forward, as in humans, and backward, as in the hind legs of goats and most other quadrupeds. With the practical implementation of the design, though, the design is much better suited to backward flexion of the knee. Darren Krasny analyzed the kinematics of the leg with the actuation scheme that flexes the knee during return to inject energy into the system. He found that the asymmetry in the knee angle at touchdown and liftoff creates a preference

for running with backward knee flexion because it reduces the rotation of the entire leg about the shoulder/hip.

More simply, Figure 7.1 indicates that the dynamics of the leg also favor motion with backward knee flexion. In the picture, the shoulder/hip actuator is inactive, so the leg is hanging freely as a pendulum. The leg's rest position clearly places the foot far forward if the motion is from left to right. Since the shoulder/hip is only driven in the return phase and the return motion is always to move the foot forward, the leg's rest position is near the desired position for foot placement. The natural dynamics of the pendular leg help the shoulder/hip actuator return it only if the forward motion is such that the knee flexes backward.

This represents another unique feature of this articulated leg design. Most of the leg designs of previous robots have had symmetric mass distributions so that at rest, they are vertically oriented like a simple pendulum. When the desired leg orientation for touchdown is forward of the vertical, as it normally is, the asymmetrical mass distribution of the prototype leg is superior for reducing to torque required of the shoulder/hip actuator.

7.8 Body

Since only a single prototype leg was constructed, the quadruped body shown in Figure 7.3 was not designed in great detail. Rather, reasonable geometric and inertial properties were generated for Marhefka's [79] simulations. For the construction of the full quadruped, the body will require a significant amount of additional design work. Berkemeier [16] showed that a quadruped's pitch motion is passively stable in bounding when its dimensionless body inertia is less than unity. The quadruped's body should be designed accordingly in order to investigate if galloping can also be accomplished with passive pitch

stability. Another important general consideration for the body design is the location of the mass center. Most animals have more of their weight at the front of their bodies while most robots built to date have had symmetrical bodies. It is not clear what the best mass distribution would be for a galloping machine.

7.9 Summary

This chapter describes the detail design of an electrically actuated, articulated leg to be used in a quadruped robot capable of galloping. One key design feature is that energy is injected into the system by storing elastic energy in mechanical springs during the return phase of the legs and then releasing that energy during the stance phase. This reduces the power requirements of the actuator. Another feature is that the asymmetric mass distribution within the leg benefits motion with backward knee flexion.

CHAPTER 8

EXPERIMENTAL RESULTS

8.1 Introduction

The prototype leg described in the previous chapter was designed for use in a quadruped robot and was tested as a monopod only to verify its performance capabilities. Validating the actuation scheme was of primary concern, but the experiments also tested the structural integrity of the leg and the sensing of ground contact with the microswitch. The only components that failed throughout the experiments were the kevlar cord of the cable drive, which broke periodically, and the racquetball covering the foot, which slowly deteriorated. This chapter describes some early experiments with the leg using open loop control, presents data suggesting that the clutch may not be needed in the cable drive system, and reviews the leg's performance in stable, stationary hopping.

8.2 Background

In all of the initial experiments, the prototype leg was intended to hop in place without any forward motion. The leg hopped on a treadmill having zero tread velocity because the wall mount of the testing apparatus was set at a height designed for experiments in hopping at speed. With the leg's controller being tuned throughout the experiments, the foot placement resulted in some forward and backward motion of the leg along the treadmill.

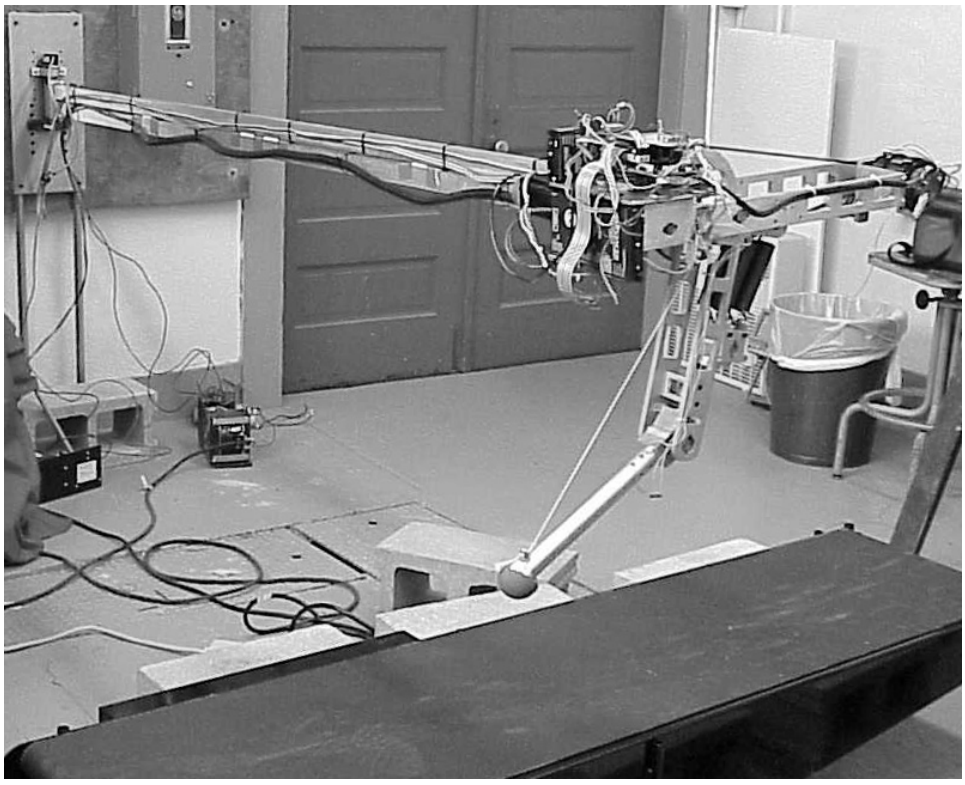

Figure 8.1: Experimental setup for the prototype leg.

A safety line tied to the leg and passing over a pulley fixed to the laboratory ceiling was used to raise the leg up into the air once it moved beyond either end of the treadmill. The leg was also drawn up with the safety line following any unusual or potentially damaging behaviors. Figure 8.1 is a photograph of the experimental setup in the laboratory.

The experiments ranged from single hop tests to stable hopping with as many as 67 steps, but the experimental procedure was basically the same for all. First, the safety line was used to raise the leg up in the air to the height from which it would drop onto the treadmill. A reasonable height was determined by intuition and experience as the experiments progressed. Once in place above the treadmill, the shoulder/hip and knee joints were positioned with the two motors, and any resulting motion of the boom was stabilized by

the experimenter. The safety line was then released quickly, allowing the leg to drop onto the treadmill and begin hopping. At the conclusion of each experiment, the leg was again raised into the air with the safety line.

In all of the experiments with closed-loop control, this procedure was preceded by an initialization of the optical encoders measuring the two boom angles and the shoulder/hip motor angle. The encoder of the cable drive motor did not require initialization in most of the experiments because it was torque-controlled. For the initialization, the upper thigh was placed parallel to the leg frame, the leg was lowered with the safety line until the foot just contacted the treadmill, and the boom was positioned perpendicular to the treadmill. In all of these experiments, the leg was dropped from roughly the same height based on the boom mechanism encoder output.

8.3 Experiments

The following sections describe the key experiments conducted with the prototype leg.

8.3.1 Open-Loop Control

Before the control board was functioning, a number of single-hop experiments were conducted with open-loop control. A constant voltage was applied to each motor to position the leg for touchdown, and then the leg was dropped. During the contact phase, no voltage was applied to either motor, and the clutch was disengaged in some of the experiments. This control method was satisfactory for the cable drive motor since a constant voltage maintained a relatively constant knee flexion prior to ground contact. It was inadequate, though, for controlling the shoulder/hip motor. The same constant voltage that held the leg in place when it was at rest above the treadmill caused the leg to rotate once it was dropped. Therefore, the position of the shoulder/hip joint could not be controlled accurately enough

to consistently achieve meaningful, single hops. The foot typically touched down too far behind the shoulder/hip joint causing the leg to fall over or to move forward without moving upwards much at all. On several occasions, though, reasonable hops were achieved.

While closed-loop control was implemented in all of the subsequent experiments, these preliminary tests did offer some qualitative results. First, the pitching of the leg revealed that the boom was connected to the leg frame too far behind the leg's center of mass. Similarly, the stiffness of the original boom in bending was found to be inadequate. Both of these problems were corrected based upon observations from the open-loop experiments. Also, the leg clearly hopped higher when the clutch was disengaged during stance. This confirmed that the clutch minimally provided some of the advantages for which it was included in the design.

8.3.2 Clutch Evaluation

The first experiments involving the clutch were conducted with the leg supported on a test stand. A voltage was applied to the cable drive motor to determine how much knee flexion could be generated before reaching the holding torque limit of the clutch. The results showed that the clutch began to slip only after the cable was wrapped around the drive pulley more than one full revolution. This was in good agreement with the static force analysis from Chapter 6 that was used to size the motor and clutch in Chapter 7. Since the cable drive was designed not to exceed one full pulley revolution, the holding torque of the clutch was acceptable. Additionally, this test proved that motor torque was not the limiting factor in the cable drive system.

Figure 8.2 plots the vertical position of the shoulder/hip joint for four different single hop experiments conducted to evaluate the role of the clutch in the cable drive system.

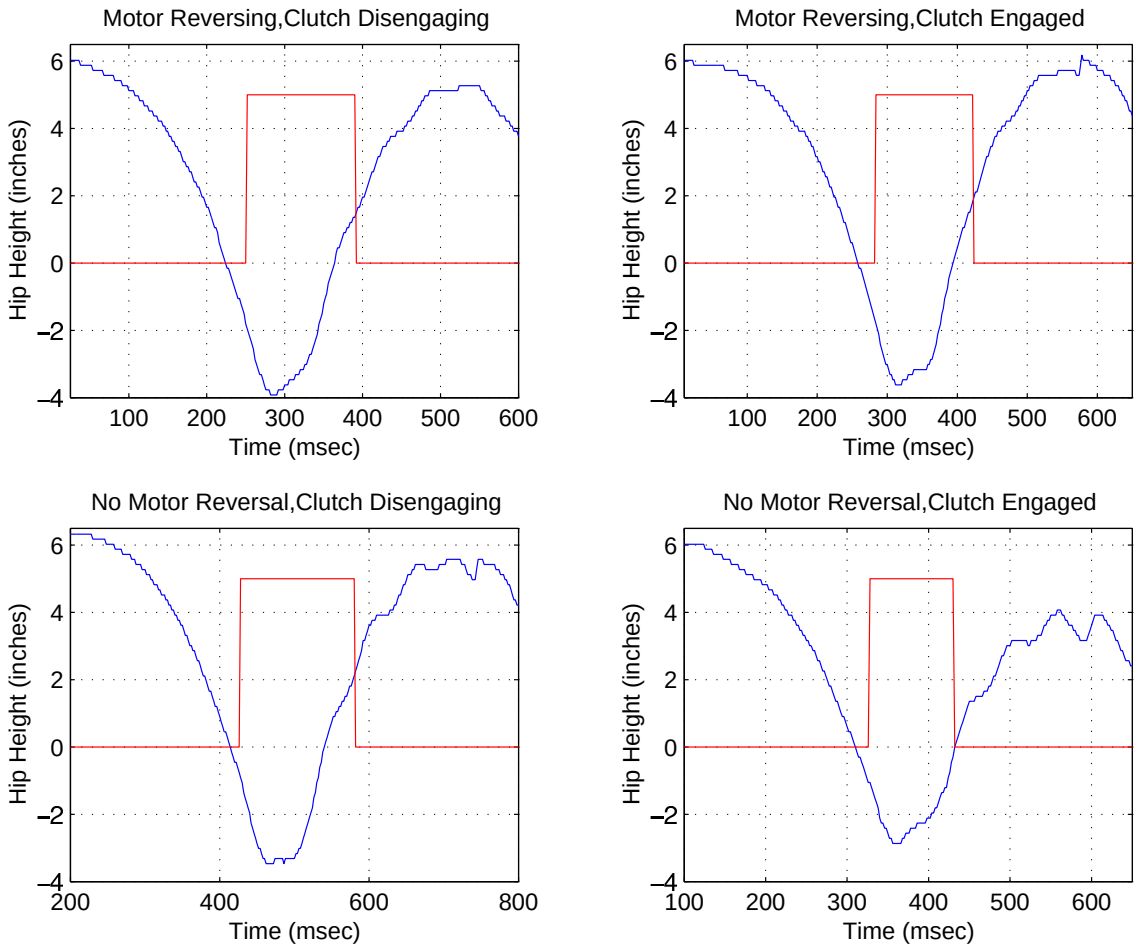

Figure 8.2: Vertical height of the shoulder/hip joint in four single hop experiments to evaluate the clutch in the cable drive system.

The rectangular curve on each plot indicates when the support phase begins and ends. In the first experiment, the voltage to the clutch was set to zero and the direction of motor rotation was reversed immediately upon foot contact with the ground. With zero volts applied to the clutch, there is a delay before it actually disengages. The motor was reversed to release as much of the cable as possible to prevent it from becoming taunt again before the clutch had disengaged. In the second experiment, the motor was reversed, but the clutch

remained engaged throughout. In the third experiment, the motor voltage was set to zero during stance rather than being reversed, and the clutch was disengaged. Finally, the clutch remained engaged and the motor was not reversed in the fourth experiment.

The heights plotted in Figure 8.2 indicate how well the energy stored in the springs during flight is returned to the leg as thrust during stance. In the fourth experiment, the hopping height is much lower than in the others because energy is lost in backdriving the motor. The duration of ground contact is also shorter because the leg lifts off from the ground while some of the energy is still stored in the springs. The best performance was anticipated with the first experiment since it made use of both clutch disengagement and motor reversal to release the cable. Figure 8.2, though, shows that the leg actually hopped higher when the motor was reversed without disengaging the clutch. Although the leg was released from a slightly greater height in the third experiment, comparison with the first experiment indicates that reversing the motor is insignificant when the clutch is disengaged. This suggests that the delay in clutch disengagement is too short to have an impact on the cable drive during stance.

Because the results shown in Figure 8.2 were unexpected, the first two experiments were repeated for multiple hops to further evaluate the role of the clutch. Figure 8.3 plots the vertical position of the shoulder/hip joint for 13 steps in each of these two experiments. Again, the rectangular wave plot indicates when ground contact occurred. The plots clearly show that the leg hops higher when the clutch remains engaged, and this larger vertical oscillation also leads to a longer single hop stride period. That average stride period is .508 s, compared to .468 s in the case of clutch disengagement. The .04 s difference in the stride periods is due entirely to the longer flight time because the average contact times of .131 s and .132 s are nearly equal.

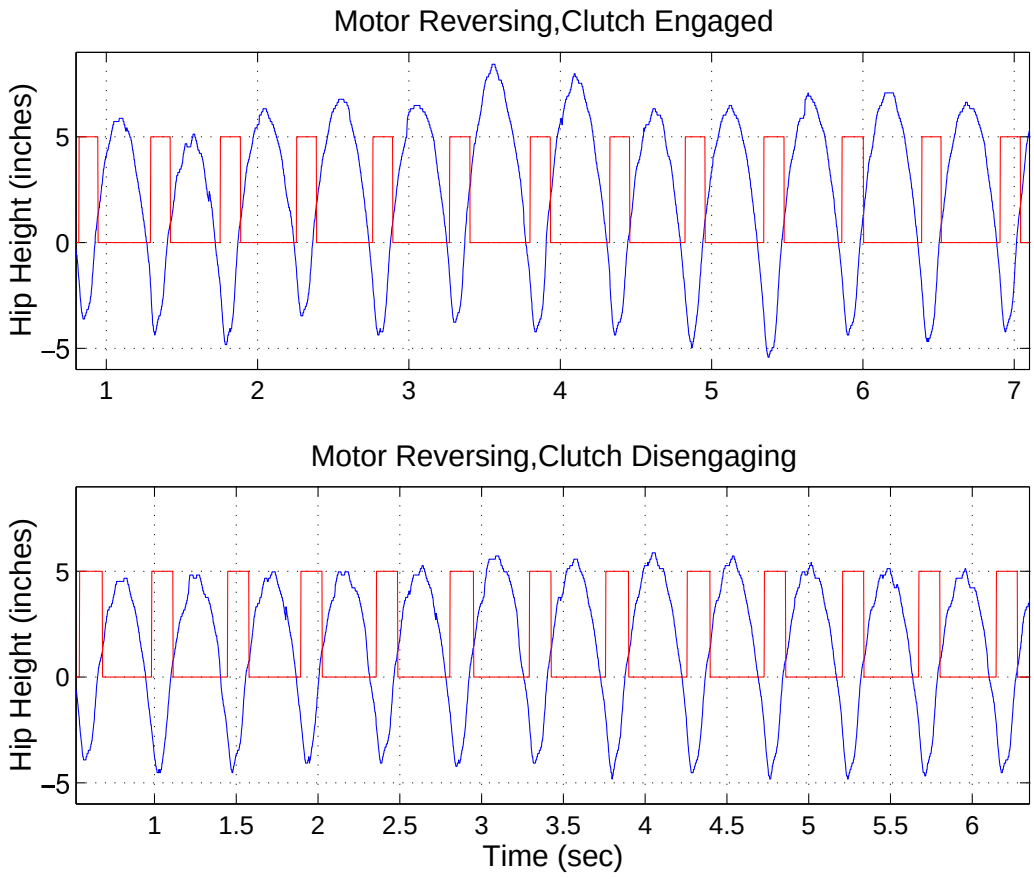

Figure 8.3: Vertical height of the shoulder/hip joint in two 13-hop experiments to evaluate the clutch in the cable drive system.

One possible explanation for the superior performance without using the clutch is that the time delay plays a role not when the clutch must disengage, but rather, when it must re-engage to draw in the cable for the following step. If the clutch does not engage quickly enough, the cable drive may not have enough time to fully draw in the cable before the next contact phase. This would not, however, explain the single hop behavior in Figure 8.2. If this is indeed the problem, the effect could be reduced by initiating clutch engagement prior to foot lift-off such that less of the flight phase duration would be consumed by engaging the clutch and more cable wrap could be achieved. Nonetheless, the current results clearly

indicate that for hopping in place, the leg's performance is better without the use of the clutch.

This does not necessarily suggest that the same would be true for running at speed, though. The results for hopping in place suggest that any energy lost by backdriving the cable drive motor when the clutch is engaged is less than the amount of energy that the system would fail to store in the springs if the clutch disengaged during stance. As speed increases, the duration of contact decreases and despite the idealized decoupling with Raibert-type control, the amount of thrust required increases. The result is that the cable drive system has both less time to release the cable during stance and more cable to release, so energy losses associated with backdriving the motor increase. At some point, these losses will likely dominate, and disengaging the clutch will be favorable. Marhefka's [79] simulations bear this out. His model of the prototype leg hops at 5 $\frac{m}{s}$ with a stride period of .475 s and a stance duration of .085 s. Comparing these values with those from the first experiment shown in Figure 8.3, the duration of flight is actually longer and the duration of stance is 35% shorter. This would allow slightly more time to draw in the cable and significantly less time to release it, suggesting that disengaging the clutch might lead to superior performance.

The same conclusion can be reached in considering the use of the leg in a galloping quadruped. Heglund and Taylor [52] predict that the stride period of a 68 kg animal will only change from about .45 s to about .42 s over the full range of galloping speeds. Again, the duration of ground contact for each foot decreases with speed, but the duration of return is nearly constant in galloping. Since this also indicates that the clutch may be advantageous, it would be premature to remove it from the leg design without first conducting experiments at speed.

8.3.3 Stable Hopping

The results in this section are from experiments in which the cable drive motor was reversed and the clutch was disengaged during ground contact. Early tests conducted with the motors improperly connected to the amplifiers showed that this was the best actuation method, so it was employed for all of the experiments prior to those presented in Figures 8.2 and 8.3.

Experiments in which the leg's position on the treadmill was stabilized by the control algorithm verified its capability for sustained operation. Figure 8.4 plots the rotation of the boom mechanism about a vertical axis for 67 steps, and the small, rectangular wave

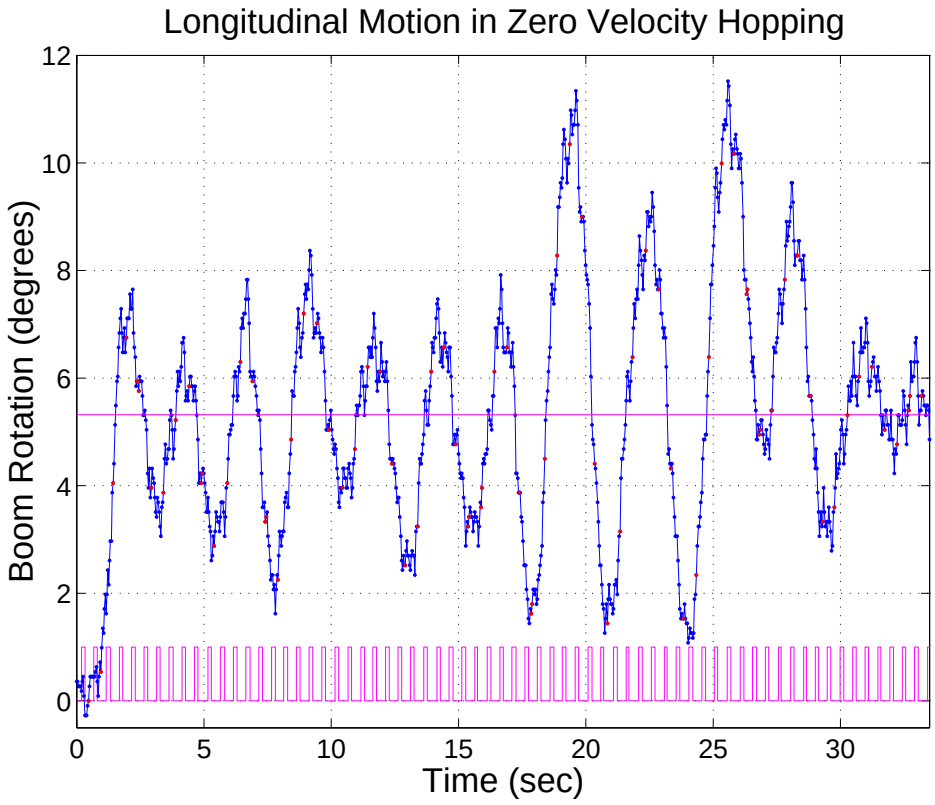

Figure 8.4: Rotation of the boom mechanism about the vertical axis for 67 steps of stable hopping. This rotation corresponds to the leg's translation along the treadmill.

plotted near the bottom of the figure indicates ground contact. The rotation of the boom corresponds to the movement of the leg forward and backward on the treadmill. The plot indicates that the leg undergoes a stable oscillation about a mean value of 5.3^o, although the desired behavior was a smaller oscillation centered about 0^o. The non-zero mean likely results from one or both of two control algorithm features. First, the control algorithm commands a desired hip joint angle at touchdown that should produce purely vertical hopping. If this value is slightly off, however, the leg would move backward or forward, as in this case, instead of vertically, as predicted. Such an error could result in a stable oscillation about a point forward of the treadmill center. Secondly, the hip drive system may not have been able to place the hip in the desired position prior to each touchdown. If the hip was placed consistently behind its desired position, this would also account for the forward position on the treadmill. Inadequate matching of the desired angle at touchdown might also explain the relatively large magnitude of oscillation.

The maximum rotation in Figure 8.4 corresponds to a translation of about 20 inches from the zero position, so the leg never reached the end of the treadmill. This experiment ended after 67 steps because the stable motion was satisfactorily achieved. The leg likely could have taken an indefinite number of steps barring any unforeseen disturbances. The average single hop stride frequency was .496 s, and the average duration of contact was .104 s.

Since the leg was designed for high speed locomotion, it is important to note that stable hopping in place was achieved without approaching the performance limits of the actuators. The commanded torque for the cable drive motor was only about two thirds of that which generated one full revolution of the pulley. Because of the non-linearity in the mechanism, the leg is capable of storing much more elastic energy in the springs with increased motor

torque, so it is also capable of generating much greater thrust during stance. Even with the limited thrust in these experiments, though, the leg hops higher than the height from which it was originally dropped. This is shown in Figure 8.5, which plots the vertical position of the shoulder/hip joint for the first 10 steps of the same experiment shown in Figure 8.4. After only the first step, the leg gains some elevation during its flight phase, and by the eighth step, the maximum height is more than 2 inches above the original drop height. The height variation from step to step in Figure 8.5 can be explained by the forward and backward motion of the leg along the treadmill.

The shoulder/hip joint motor has a peak current of 13.8 amps, and it is driven by an amplifier that can provide only 7.5 amps continuously and 15 amps for short periods of

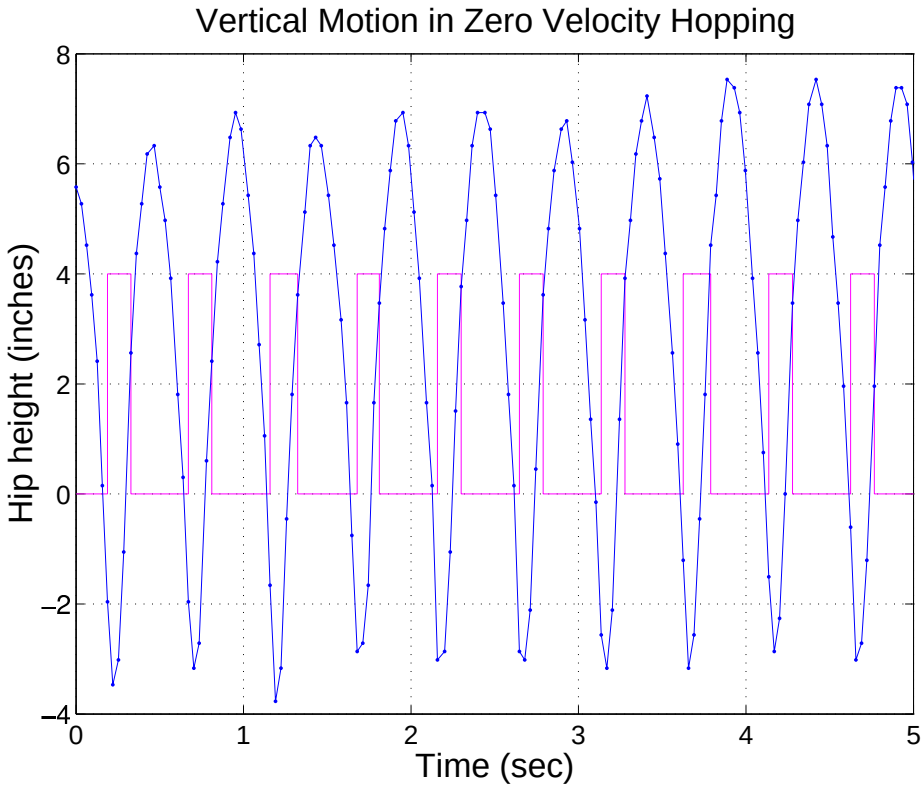

Figure 8.5: Vertical displacement of the hip joint.

time. For the stable hopping experiments, the peak current of the amplifier was limited to 13 amps, and the commanded duration of this peak was never long enough to cause a transition to the lower continuous current value. If greater torque were needed, however, a larger amplifier could be used to maximize the performance of the motor.

Figure 8.6 plots the angular velocity of shoulder/hip joint for 6 steps in the middle of the stable hopping experiment. The desired velocity of the joint is zero at each foot contact with the ground. The velocity data points immediately before each rise in the rectangular wave plot give an indication of how well the motor is positioning the joint prior to touchdown. In each case, the joint velocity is decreasing and very nearly zero, so the motor is able to position the leg within the duration of the flight phase. A non-zero joint velocity at

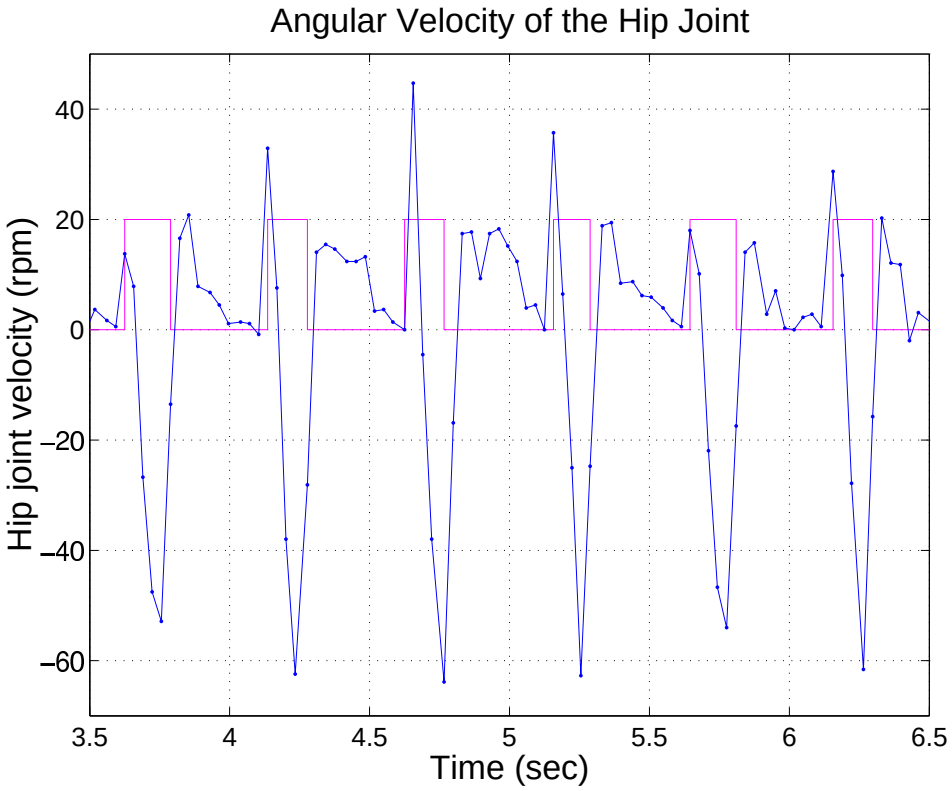

Figure 8.6: Angular velocity of the hip joint.

touchdown would suggest that larger torque is needed to return the leg. Again, a larger amplifier could be used to generate such torque if necessary for future experiments.

8.4 Design Improvements

Based upon experience with the prototype leg, a number of design changes should be considered and evaluated to potentially improve the leg for use in the quadruped robot. One simple change would be the use of a stronger kevlar cord for the cable drive to prevent the periodic failure that occurred during the experiments. Also, the connection of the cord to the shank could be altered to achieve more consistent tension in the cord. With the cord tied to an eyebolt fixed in the shank, its tension while the leg was at rest typically decreased up to a point as the experiments progressed. This did not pose a problem with the cable drive system operating under torque control, but it could be an issue if position control was implemented instead.

A lighter leg would likely be able to travel at higher speeds since both the impact losses and the load on the shoulder/hip actuator would be lower. As mentioned in Chapter 7, the mass of the leg could be reduced without compromising strength by removing additional material in non-critical areas. Finite element analysis is one method that could help in identifying these areas. Alternatively, different materials could be used for some of the components. For example, the round aluminum tubing in the shank might be replaced with carbon-fiber tubing. The leg frame itself might even be reduced in size if it can be shown that the rotating leg does not require all of the clearance provided at the back of the frame. The frame length would still need to be selected with the consideration of available timing belts, but it likely could be shortened.

The position of the cable drive motor extending out from the leg frame may be rather inconvenient for use in the quadruped. As such, the cable drive system could be redesigned to position the motor underneath the leg frame with its shaft parallel to the axis of the drive pulley rather than collinear with it. An alternative gearing arrangement might be advantageous for this design change.

Regardless of the possible changes described above, the following two changes should be pursued enthusiastically in order improve the leg's performance. First, it would be quite advantageous to locate a different clutch having at least the same holding torque, but shorter time delays for engaging and disengaging. The use of this clutch would reduce the energy losses associated with backdriving the motor and alleviate the control difficulties resulting from the delay times in the current clutch. Until experiments at speed can definitively show that the clutch is not needed in the leg, with this eventuality being unlikely, it would be unwise to eliminate the clutch from the design. The second change is to reduce the diameter of the idler pulley in the cable drive system in order to reduce the coupling between the two drives. The minimum diameter of that idler is limited by the diameter of the shoulder/hip joint shaft, but it should be made as small as possible.

8.5 Summary

The prototype leg's design has been validated through a number of monopod hopping experiments. Preliminary tests with open-loop control provided some key insights, but closed loop control was required for more advanced testing. Contrary to expectations, the inclusion of a clutch in the cable drive system was found to be detrimental to the leg's performance for hopping in place. Stable hopping verified that the leg can operate continuously without approaching the actuator limits, and this is the key experimental result,

since the high speeds for which the leg was designed will likely require greater actuator performance.

CHAPTER 9

SUMMARY AND FUTURE WORK

9.1 Summary

Legged vehicles have the potential to traverse rough terrain with greater speed, efficiency, and mobility than can conventional wheeled and tracked vehicles. The dynamically stable quadrupeds built to date, however, have bounded at speeds below those at which that gait becomes energetically efficient. This dissertation proposes that the efficiency of the gallop at high speeds can be explained by the vertical oscillations of the mass center and the stride frequency of the gait. Furthermore, it details the design of articulated legs for a quadruped galloping machine.

A simple, non-invasive method of measuring an animal's geometric and inertial properties is proposed to aid in developing a mathematical model of the animal. Angular momentum analysis indicates that in order to accurately capture the dynamics of quadrupedal running gaits, leg mass much be included in this model and a robot model of similar size. Leg mass is most critical for modeling galloping and bounding, and less critical for trotting and pacing.

An impulsive model applied to all dynamic quadrupedal gaits indicates that at equal stride frequencies, galloping requires smaller vertical oscillations of the mass center than

trotting does, regardless of speed. This model specifically addresses high-speed locomotion, though, because the duration of leg support is taken to be infinitesimal.

Spring-mass models of trotting and galloping are introduced and compared for motion with the same vertical oscillations and stride frequencies. At typical trotting speeds, the galloping model requires legs of lower stiffness than the trotting model, and at typical galloping speeds, the trotting model requires the legs to rotate through extremely large angles. Therefore, trotting is accomplished with smaller vertical oscillations and/or lower stride frequencies at lower speeds. In combination, the spring-mass and impulsive models account for the trot-to-gallop transition in terms of vertical oscillations and stride frequencies.

The kinetic energy lost in a plastic collision of a robot with a stationary environment is calculated and applied to the design of legs for dynamically stable mobile robots. The generalized inertia ellipsoid is introduced as a visualization tool for selecting an optimal leg design that balances the relative merits of minimizing impact losses and minimizing the energy required to return the leg.

The desired leg compliance for a quadruped robot is proposed to match that of biological quadrupeds having the same mass as the robot and is calculated as an exponential function of the mass. A kinetostatic analysis of an articulated leg's effective stiffness is introduced to aid in the geometric layout of a leg design. The method is applied to develop the geometry of a prototype leg for a galloping quadruped.

The final prototype leg design is composed of a thigh and a shank with mechanical extension springs acting across the knee joint that joins the two. The leg is designed to store energy in the springs during the return phase and then release that energy as thrust during

the stance phase. A unique characteristic of the leg design is that the mass distribution is asymmetrical, so its rest position is near its forward placement for rapid locomotion.

Experimental testing of prototype leg indicates that it is capable of continuous hopping in place without approaching the performance limits of the actuators. This suggests that the leg should also be able to hop at the higher speeds for which it was designed. One unexpected result was that the cable drive system that actuates the knee joint performs better without the use of the clutch to release the cable.

9.2 Extensions of Present Work

This dissertation addresses the mechanics of quadrupedal galloping and the design of a leg for a galloping robot. The work suggests a number of immediate extensions in both the modeling of dynamic legged locomotion and the construction of the first quadruped robot capable of true galloping.

9.2.1 Modeling

The accuracy of the measurement techniques and the resulting biological quadruped model proposed in Chapter 2 could be verified by sacrificing an animal once the measurements are complete. The masses and moments of inertia of all body segments could then be definitively measured for comparison. With good agreement, the validity of the model would be confirmed, and it could be used without additional loss of animal life for verification. The sling for measuring the moments of inertia could also be redesigned to hold the animal more securely and prevent the problems experienced with the existing sling. Sedating the animal during this measurement is another possibility.

The effect of leg mass on the dynamics of various gaits could be further investigated through dynamic simulation. Comparing the motion of quadruped models both including

and neglecting leg mass in simulation would provide another means of quantifying the significance of leg mass in accurately modeling each gait. Ideally, simulation results would be verified through experiments with quadruped robots and/or animals.

The results of the impulsive models in Chapter 3 could be compared with high-speed video and force plate measurements of animals running with the various gaits. The phasings of the legs, angular displacements of the trunk, vertical oscillations of the mass center, and ground reaction impulses could all be compared with the experimental data. Additionally, video of animals running over a range of speeds could be used to evaluate the assumption that the legs operate at an optimal working length.

As mentioned in Chapter 4, the spring-mass model for galloping would more accurately model biological quadrupeds if the body was asymmetric. Similarly, the resulting motion would be more general and more consistent with animal behavior with the elimination of its symmetry constraints. Additional work is needed to develop such a model for which the equations of motion can still be solved. The model would also benefit from data collected for galloping animals in the same way that Farley et al. [34] collected data for trotting animals.

Finally, it would be worthwhile to pursue non-dimensional forms of all of the models presented. This would likely not be too difficult for either of the spring-mass models, but it could lead to additional complexity in the impulsive models. In non-dimensional form, the models would be independent of body size and thus, might provide more general insight into dynamic quadrupedal locomotion.

9.2.2 Experimental Work

The most immediate extension of the experimental work with the prototype leg is to test it hopping at various speeds. Certainly, it is logical to begin at relatively slow speeds and to then proceed with experiments of increasing speed to eventually determine the maximum speed at which stable hopping can be maintained. Marhefka's [79] simulations indicate that the leg should be capable of traveling at least as fast as 5 $\frac{m}{s}$. The predicted trot-to-gallop transition speed of a 68 kg animal is 3.8 $\frac{m}{s}$, so for use in a quadrupedal galloping machine of this size, the leg should minimally be able to attain this speed.

The benefits of driving the shoulder/hip actuator during stance could also be investigated to further improve leg performance. In all experiments to date, no shoulder/hip torque was exerted during stance. If the pitch motion of the quadruped body is not passively stable in the gallop, shoulder/hip torque during stance will be needed to stabilize it. A thorough understanding of how that torque affects the motion of the single leg would be helpful in the implementation with the full quadruped.

Once the performance of the prototype leg has been verified at an adequate speed, the quadruped's body must be designed. The leg frame design will need to be modified in conjunction with the body design to allow for the leg's abduction/adduction motion. The body design should account for carrying the hardware to sense its angular position and velocity, coordinate the motion of the four legs, and possibly power the machine once stable galloping has been achieved with off-board power. The distribution of mass within the body is an important consideration. Beyond achieving a dimensionless inertia of less than unity [16], the optimal distribution of mass remains an open question.

The first experiments with the constructed quadruped robot should probably involve pronking in place so that with all four legs operating simultaneously, the body's orientation

does not change. These experiments could be followed by bounding in place with the body pitching back and forth. From there, forward bounding at speed could be achieved, eventually leading to galloping by introducing a phase shift between the legs. This sequence is not an ideal method of reaching a gallop, as animals never exhibit behavior even remotely similar to it. The method is, however, reasonable for preliminary experiments. Animals may move from rest into a walk, then a trot, and finally a gallop, or they may leap directly from rest into a gallop. The prototype leg developed in this work is poorly designed for trotting because flexing the knee for ground clearance requires a large amount of energy from the cable drive system. Leaping into a gallop is a challenging task and the subject of future work, as described in the following section.

9.3 Extensions Beyond Present Work

Additional areas of research in modeling dynamic locomotion and constructing legged machines stem from this work, but are beyond its immediate scope.

9.3.1 Modeling

Heglund and Taylor [52] showed that the stride frequencies of animals of vastly different sizes increase almost linearly with speed both in trotting and galloping. The predicted stride frequency of each gait at zero velocity can be extrapolated from the data, even though neither gait is used for bouncing in place. The trotting data predicts nearly the same zero velocity stride frequency for animals of all sizes, while the predicted galloping frequencies vary widely. An explanation for this phenomenon would improve the understanding of how animals move in each gait. Does the symmetry of the trot and the asymmetry of the gallop account for the difference? Does the variable phasing of the legs or the pitch motion of the body in the gallop explain the variation in predicted zero velocity stride frequency?

This same work shows that in trotting, speed is increased predominantly by increasing stride frequency, whereas in galloping, speed is increased predominantly by increasing stride length. Again, is the explanation for this behavior simply that the phasing of the gallop is asymmetrical such that the legs operate more nearly in phase as speed increases? Can simple spring-mass models of trotting and galloping account for this phenomenon? Can they be used to predict the optimal stride frequency for a given speed within each gait?

In Chapter 1, the animals that display preferences for the transverse and rotary gallops are listed along with some possible explanations for those preferences. Still, there is no definitive account of the relative advantages of these two gaits. A model of galloping that could offer such insight would be significant.

Additional research is also needed to fully understand the role of back flexion in asymmetrical gaits like the bound and gallop. Modeling back flexion in animals could better account for the advantages of galloping and aid in the design of quadruped robots with flexible bodies. Even beyond this flexibility, an understanding of coordinated neck and head movements would also improve knowledge of animal locomotion.

9.3.2 Experimental Work

The prototype leg designed in this work could be improved through a number of enhancements. As alluded to in Chapter 7, springs acting across the shoulder/hip joints could help to return the leg and reduce the power requirements of the shoulder/hip actuators. How to select an appropriate stiffness for these springs remains an open question, and a simple method like the one proposed in Chapter 6 for selecting leg stiffness would be very

useful. The advantages of adding an ankle joint to the leg should also be thoroughly investigated. An ankle might help increase ground clearance and modulate effective leg stiffness on compliant surfaces.

At present, the prototype leg is to be used for both the front and hind legs of the quadruped. The advantage of having different designs or different stiffnesses for the front and hind legs remains an open question and likely depends upon the distribution of mass within the body. The design of different articulated legs is also of interest. How do different actuation schemes affect the preferred direction of knee flexion in other articulated legs? How can one design a leg that folds enough in the return phase to significantly reduce its moment of inertia? What are the key advantages of an articulated leg compared to a telescoping leg beyond those discussed in this work, and how does one design a leg to capture them? While all of these ideas would be implemented in experimental hardware, modeling and simulation would certainly aid in that process.

Future work with the quadruped galloping machine should investigate rapid starting, stopping, and directional changes. Since trotting is undesirable with the prototype leg design, leaping into a gallop is the most favorable means of reaching the gait. Mimicking animals, rapid starts would likely involve the paired use of the hind legs to generate most of the forward thrust. Similarly, rapid stopping would likely involve the paired use of the front legs to absorb as much of the translational kinetic energy as possible. Directional changes could be achieved by performing a rapid start in a new direction immediately after a rapid stop, but there are likely more efficient methods to be investigated.

Ideally, transitions between gaits should also be studied since the gallop is exclusively a high-speed gait. The difficulty of trotting with the prototype leg design is problematic, but pacing might be an alternative intermediate speed gait since the roll motion of the

body can provide greater ground clearance. Even preliminary walking experiments with the quadruped would help develop insight for designing legs that function well in both statically and dynamically stable locomotion.

Ultimately, experiments with legged robots like the quadruped galloping machine need to be conducted on uneven terrain to verify that they possess the locomotory advantages for which they have been constructed.

9.4 Conclusion

This dissertation proposes that galloping is energetically advantageous at high speeds because it allows for motion with smaller vertical oscillations and/or lower stride frequencies than trotting. In contrast, trotting is superior at lower speeds for the same reason. The design of legs for a quadruped robot that can capture the advantages of galloping should balance the minimization of impact losses and the energy required to return the legs. The selection of leg stiffness is also critical as it largely determines stride frequency. The experimental results with the prototype leg described in this work indicate that it has the potential to be the foundation of the first quadruped robot capable of galloping.

APPENDIX A

COMPOUND PENDULUM

Figure A.1 shows a compound gravitational pendulum of mass m and moment of inertia I. The distance from the axis of rotation to the mass center is l, and the angular displacement is ϕ. If the pendulum is driven at a frequency ω with a torque of magnitude τ, summing moments about the axis of rotation yields,

$$I\ddot{\phi} = \tau \sin \omega t - mgl \sin \phi, \tag{A.1}$$

where g is the acceleration of gravity and t is time. Making the small angle approximation,

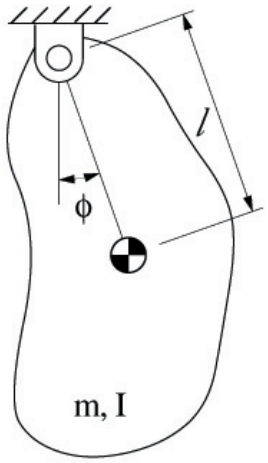

Figure A.1: Compound gravitational pendulum.

Equation A.1 simplifies to,

$$\ddot{\phi} + \frac{mgl}{I}\phi = \frac{\tau}{I}\sin\omega t. \tag{A.2}$$

The transient component of the solution to this non-homogeneous, linear, second order differential equation can be ignored, leaving,

$$\phi = \frac{\tau \sin\omega t}{I(\omega_n^2 - \omega^2)}, \tag{A.3}$$

where ω_n is the natural frequency of oscillation given by,

$$\omega_n = \sqrt{\frac{mgl}{I}}. \tag{A.4}$$

The work, W, required to drive the pendulum at the frequency ω is the integral of the product of the torque and the differential change in ϕ, so the work over one quarter cycle of oscillation is,

$$W = \int_0^{\frac{\pi}{2\omega}} \frac{\tau^2 \omega \sin\omega t \cos\omega t}{I(\omega_n^2 - \omega^2)} dt. \tag{A.5}$$

Evaluating the integral,

$$W = \frac{\tau^2}{2I(\omega_n^2 - \omega^2)}. \tag{A.6}$$

Viewing a leg as a compound gravitational pendulum, the return phase comprises one half cycle of oscillation, so the work required to return a leg is twice that given in Equation A.6. Recognizing from Equation A.3 that the amplitude of the angle of rotation, Φ, is,

$$\Phi = \frac{\tau}{I(\omega_n^2 - \omega^2)}, \tag{A.7}$$

the work to return a leg can be expressed as,

$$W_{leg} = I\Phi^2(\omega_n^2 - \omega^2). \tag{A.8}$$

The average power associated with returning a leg is the work divided by the duration of the return phase, $\frac{\pi}{\omega}$.

$$P = \frac{I\Phi^2\omega(\omega_n^2 - \omega^2)}{\pi}. \tag{A.9}$$

Since the average power is a function of the difference of the squares of the driven frequency and the natural frequency, it increases rapidly as the difference between the two frequencies increases. As it is also a function of the square of the angle through which the leg is driven, the average power also increases rapidly as the leg rotates through larger angles.

APPENDIX B

LEG COMPONENTS AND ASSEMBLY INSTRUCTIONS

Only the mechanical components of the leg and none of the control hardware or power supplies are listed in this appendix. Similarly, the assembly instructions do not address the electronic control system.

B.1 Machined Components

In this and all subsequent sections, the names of the Pro/Engineer drawing files are included in parentheses following the descriptions of the components where applicable.

2 Brackets, .25 thick aluminum (bracket.prt)

3 Cardboard Washers, 1.3 bore, 1.625 OD

1 Clutch Spacer, aluminum (spaceclutch.prt)

1 Electronics Mounting Plate, .125 thick aluminum (topplate.prt)

1 Foot, aluminum (footround.prt)

1 Foot Cap, .1 thick aluminum (footcap.prt)

1 Frame-1, .375 thick aluminum (frame1.prt)

1 Frame-2, .375 thick aluminum (frame2.prt)

1 Frame-3, .375 thick aluminum (frame3.prt)

1 Frame-4, .375 thick aluminum (frame4.prt)

1 Frame-5, .375 thick aluminum (frame5.prt)

1 Frame-6, .375 thick aluminum (frame6.prt)

1 Idler Pulley, aluminum (pullbush.prt)

1 Insert, aluminum (insert.prt)

1 Large Boom shaft with Extension (for encoder mount), steel (boomshaft2.prt)

1 Left Thigh, .375 thick aluminum (thigh.prt)

2 Leg Boom Brackets, aluminum (parallel5.prt)

1 Lower Shank, 1.25 diameter round aluminum tube, .125 wall (lowshankround.prt)

1 Mid Shank, aluminum with steel shaft pressed through (midshank.prt)

1 Motor Shaft Extension, .5 diameter, steel (incorporated in motor.prt)

1 Pillowblock-like Cap, aluminum (pillowcap.prt)

1 Plastic Bushing, 1.25 bore (footbushing.prt)

1 Pulley, with .125 steel pin pressed into it, aluminum (pulley.prt)

2 Rectangular Aluminum Tubes, 1.5 x .75 x 8 feet, .125 wall (squaretube.prt)

1 Right Thigh, .375 thick aluminum (thigh2.prt)

2 Round Tubes, 1.0 OD, ground supports size and shape could be anything (vertube.prt)

1 Shank Cap, aluminum with steel shaft pressed through (topshank.prt)

2 Shank Flanges, .375 thick aluminum (shankbear.prt)

1 Shank Spring Hook Piece, aluminum (shankhooks.prt)

1 Sleeve, aluminum (sleeve.prt)

3 Small Boom Shafts, steel (boomshaft.prt)

1 Small Boom Shaft with Extension (for encoder mount), steel (boomshaft3.prt)

1 Strap, .25 thick aluminum (strap.prt)

2 Thigh Flanges, aluminum (flangethigh.prt)

1 Thigh Shaft, .625 diameter, steel (shaftpulley.prt)

1 Thigh Spring Hook Piece, aluminum with steel shaft pressed through (hookthigh.prt)

1 Upper Shank, 1.25 diameter round aluminum tube, .125 wall (upshankround.prt)

2 Wall Boom Brackets, aluminum (parallel6.prt)

1 Wall Plate, .25 thick aluminum (wallplate.prt)

B.2 Purchased Components

The manufacturer or distributor's name and part number are listed where applicable.

2 Ball Bearings, 17 mm bore, 30 mm OD, NTN part #6903 (bearing30.prt)

4 Ball Bearings, 17 mm bore, 35 mm OD, NTN part #6003 (bearing35.prt)

5 Ball Bearings, .5 bore, NTN part #R8ZZ/5C (bearhalfbore.prt)

3 Ball Bearings, .625 bore, NTN part #R10ZZC3/5C (bear625bore.prt)

1 Ball Bearing, .75 bore, NTN part #R12ZZC3/5C (idler.prt)

8 Bearings, .3125 bore, extended inner race, McMaster Carr part #57155K71 (bear3125bore.prt)

1 Braided Cable, tubular kevlar, Pratt Hobbies Small Size TKS-20, 1/8 wide

2 Bronze Bushings, flanged, .625 bore (bigbushing.prt)

8 Bronze Bushings, flanged, .188 bore (bushing.prt)

1 Clutch, Electroid part #BEC-30C-8-8-28V-L-P CL (clutch.prt)

1 Hathaway Emoteq 2302 Motor, with 10:1 gearhead (motor.prt)

1 Hathaway Emoteq 3003 Motor (hath3003.prt)

1 Large Timing Belt Pulley, aluminum, Gates part #5MR-112S-09 ALUM, machined after purchase (disk.prt)

1 Optical Encoder, .25 hollow shaft bore, 1000 line, McMaster Carr part #6207K13, Accu-Coder 755A (encoder.prt)

1 Optical Encoder, .375 hollow shaft bore, 1000 line, McMaster Carr part #6207K14, Accu-Coder 755A (encoder.prt)

1 Pillowblock, .625 bore, Fafnir part #RAK5/8 (pillowblock.prt)

1 Racquetball

1 Rubber Pad, approximately .25 thick

1 Small Timing Belt Pulley, Gates part #5MR-21S-09 ALUM (disksmall.prt)

4 Springs, .157 wire diameter, 27.5 coils, 1.142 OD, 5.866 free length inside hooks, 3.898 travel, aligned hooks, music wire (sweep2.prt)

1 Subminiature Microswitch, Cherry part #DA3C-D1RB (switch.prt)

1 Tachometer, Baldor 5PY Series part #PTG1024LD

1 Tachometer Adapter Kit, Lesson part #175193

1 Timing Belt, Gates PowerGrip GT part #5MR-1150-09

1 Treadmill, Jog-A-Dog D.C. #6 with 1.0 H.P. motor, speed adjustment to 12mph

1 Wave Spring, Smalley Steel Ring Company part #SSR-0162

B.3 Fasteners and Hardware

1 Eye Bolt, #10-24x.75

2 Machine Screws, #2-56x.5

4 Machine Screws #4-40x.25

4 Machine Screws, #4-40x.375

3 Machine Screws, #8-32x.375

8 Machine Screws, #10-24x.25

5 Machine Screws, #10-24x.5

10 Machine Screws, #10-24x.625

16 Machine Screws, #10-24x.75

6 Machine Screws, #10-24x1.0

2 Machine Screws #10-24x1.25

2 Machine Screws #10-24x1.75

4 Machine Screws, #10-32x.5

2 Machine Screws #12-24x1.0

6 Machine Screws 1/4-20x.875

1 Machine Screw, 1/4-20x2.5

2 Machine Screws 3/8-16x1.0

10 Nuts, #10-24

2 Nuts, #12-24

3 Nuts, 1/4-20

2 Nuts, 3/8-16

1 Retaining Ring, .75 bore (retainingringbig.prt)

1 Retaining Ring, 1.25 bore (retainingring.prt)

5 Shim Spacers, .5 bore, .047 thick, steel, McMaster Carr part #98126A694 (spacerhalf.prt)

2 Shim Spacers, .625 bore, .047 thick, steel, McMaster Carr part #98126A697 (spacer625.prt)

2 Washers, 1/4

B.4 Shank Assembly

B.4.1 Parts List

1 Foot, aluminum (footround.prt)

1 Racquetball

1 Rubber Pad, approximately .25 thick

1 Plastic Bushing, 1.25 bore (footbushing.prt)

1 Foot Cap, .1 thick aluminum (footcap.prt)

1 Insert, aluminum (insert.prt)

1 Lower Shank, 1.25 diameter round aluminum tube, .125 wall (lowshankround.prt)

1 Mid Shank, aluminum with steel shaft pressed through (midshank.prt)

1 Retaining Ring, 1.25 bore (retainingring.prt)

1 Subminiature Microswitch, Cherry part #DA3C-D1RB (switch.prt)

1 Shank Cap, aluminum with steel shaft pressed through (topshank.prt)

1 Upper Shank, 1.25 diameter round aluminum tube, .125 wall (upshankround.prt)

1 Wave Spring, Smalley Steel Ring Company part #SSR-0162

1 Eye Bolt, #10-24x.75

2 Nuts, #10-24

2 Washers, #10-24

3 Cardboard Washers, 1.3 bore, 1.625 OD

2 Machine Screws, #2-56x.5

2 Machine Screws, #10-24x.5

4 Machine Screws, #4-40x.375

B.4.2 Assembly Instructions

1. Press and glue upper shank into shank cap.

2. Press and glue upper shank assembly into mid shank such that the two steel shafts are parallel.

3. Press and glue lower shank into mid/upper shank assembly such that the single hole for the eye bolt in the lower shank points in a direction perpendicular to the steel shafts and faces the acute angle of the assembled shank.

4. Thread one #10-24 nut onto eye bolt to end of threads at eye. Slip one #10-24 washer over eye bolt.

5. Mount eye bolt to lower shank through single hole in lower shank with additional #10-24 washer and nut such that the eye is parallel to the long axis of the lower shank.

6. Duck tape rubber pad to upper shank such that it faces the acute angle of the shank and covers the region at least from .25 inches above the mid shank to 1.25 inches above the mid shank.

(The following may best be completed once all other assemblies are complete.)

7. Slide foot cap onto lower shank.

8. Place retaining ring on lower shank.

9. Feed wires for microswitch through holes at the top of lower shank and tie off for stress relief.

10. Solder wires to microswitch.

11. Bolt microswitch to insert with two #2-56x.5 machine screws such that plunger faces downward.

12. Bolt insert to lower shank through slot with two #10-24x.5 machine screws such that plunger extends below lower shank, but none of the insert does. Adjustment can be made

here to achieve the desired sensitivity to ground contact.

13. Slip cardboard washers over lower shank.

14. Slip wave spring over lower shank.

15. Press plastic bushing into foot.

16. Bolt foot to foot cap with four #4-40x.375 machine screws.

17. Cut a hole in the racquetball that is slightly smaller than one hemisphere.

18. Press the racquetball over the foot. Glue may be added first if necessary.

B.5 Leg Assembly

B.5.1 Parts List

Shank Assembly

2 Ball Bearings, 17 mm bore, 30 mm OD, NTN part #6903 (bearing30.prt)

4 Ball Bearings, 17 mm bore, 35 mm OD, NTN part #6003 (bearing35.prt)

2 Bronze Bushings, flanged, .625 bore (bigbushing.prt)

2 Brackets, .25 thick aluminum (bracket.prt)

8 Bronze Bushings, flanged, .188 bore (bushing.prt)

1 Large Timing Belt Pulley, aluminum, Gates part #5MR-112S-09 ALUM (disk.prt)

2 Thigh Flanges, aluminum (flangethigh.prt)

1 Thigh Spring Hook Piece, aluminum with steel shaft pressed through (hookthigh.prt)

1 Idler Pulley, aluminum (pullbush.prt)

2 Shank Flanges, .375 thick aluminum (shankbear.prt)

1 Shank Spring Hook Piece, aluminum (shankhooks.prt)

1 Strap, .25 thick aluminum (strap.prt)

4 Springs, .157 wire diameter, 27.5 coils, 1.142 OD, 5.866 free length inside hooks, 3.898

travel, aligned hooks, music wire (sweep2.prt)

1 Left Thigh, .375 thick aluminum (thigh.prt)

1 Right Thigh, .375 thick aluminum (thigh2.prt)

1 Braided Cable, tubular kevlar, Pratt Hobbies Small Size TKS-20, 1/8 wide

1 Thigh Shaft, .625 diameter, steel (shaftpulley.prt)

10 Machine Screws, #10-24x.625

8 Machine Screws, #10-24x.25

1 Machine Screws, #10-24x1.0

4 Machine Screws, #10-24x.75

B.5.2 Assembly Instructions

1. Press two ball bearings (35 mm OD) into left thigh.

2. Press two ball bearings (35 mm OD) into right thigh.

3. Bolt thigh flange to left thigh with four #10-24x.625 machine screws such that keyways align.

4. Bolt thigh flange to right thigh with four #10-24x.625 machine screws such that keyways align.

5. Press two bronze bushings (.625 bore) into idler pulley.

6. Slip idler pulley assembly over thigh shaft.

7. Press keys into thigh shaft.

8. Locate thigh shaft, thigh spring hook piece, and shank assembly between left thigh and right thigh.

9. Connect thigh pieces together by bolting the two brackets in between them using eight #10-24x.25 machine screws.

10. Bolt large timing belt pulley to thigh with #10-24x1.0 machine screw.

11. Tighten large timing belt pulley set screws on thigh shaft.

12. Press ball bearing (30 mm OD) into left shank flange.

13. Press ball bearing (30 mm OD) into right shank flange.

14. Locate shank flange bearings on shaft in top shank and bolt to shank spring hook piece with four #10-24x.75 machine screws.

15. Bolt strap to shank flange assembly with two #10-24x.625 machine screws.

16. Press four bronze bushings (.188 bore) into thigh spring hook piece with flanges facing outside the part.

17. Press four bronze bushings (.188 bore) into shank spring hook piece with flanges facing outside the part.

18. Place hook ends of four springs into bronze bushings in thigh spring hook piece and shank spring hook piece.

B.5.3 Frame Assembly

B.5.4 Parts List

Leg Assembly 2 Ball Bearings, .625 bore, NTN part #R10ZZC3/5C (bear625bore.prt)

5 Ball Bearings, .5 bore, NTN part #R8ZZ/5C (bearhalfbore.prt)

1 Timing Belt, Gates PowerGrip GT part #5MR-1150-09

1 Clutch, Electroid part #BEC-30C-8-8-28V-L-P CL (clutch.prt)

1 Small Timing Belt Pulley, Gates part #5MR-21S-09 ALUM (disksmall.prt)

1 Frame-1, .375 thick aluminum (frame1.prt)

1 Frame-2, .375 thick aluminum (frame2.prt)

1 Frame-3, .375 thick aluminum (frame3.prt)

1 Frame-4, .375 thick aluminum (frame4.prt)

1 Frame-5, .375 thick aluminum (frame5.prt)

1 Frame-6, .375 thick aluminum (frame6.prt)

1 Hathaway Emoteq 3003 Motor (hath3003.prt)

1 Ball Bearing, .75 bore, NTN part #R12ZZC3/5C (idler.prt)

1 Hathaway Emoteq 2302 Motor, with 10:1 gearhead (motor.prt)

1 Motor Shaft Extension, .5 diameter, steel (incorporated in motor.prt)

1 Pulley, with .125 steel pin pressed into it, aluminum (pulley.prt)

1 Retaining Ring, .75 bore (retainingringbig.prt)

1 Sleeve, aluminum (sleeve.prt)

1 Clutch Spacer, aluminum (spaceclutch.prt)

5 Shim Spacers, .5 bore, .047 thick, steel, McMaster Carr part #98126A694 (spacerhalf.prt)

2 Shim Spacers, .625 bore, .047 thick, steel, McMaster Carr part #98126A697 (spacer625.prt)

1 Electronics Mounting Plate, .125 thick aluminum (topplate.prt)

12 Machine Screws, #10-24x.75

5 Machine Screws, #10-24x1.0

3 Machine Screws, #10-24x.5

4 Machine Screws, #10-32x.5

3 Machine Screws, #8-32x.375

1 Machine Screw, 1/4-20x2.5

4 Nuts, #10-24

1 Nut, 1/4-20

2 Washers, 1/4

B.5.5 Assembly Instructions

1. Press three ball bearings (one .625 bore and two .5 bore) into frame-1.

2. Thread #10-24x1.0 machine screw through individual hole in frame-1.

3. Bolt Hathaway Emoteq 2302 motor to frame-1 with four #10-24x1.0 machine screws and four #10-24 nuts. This is the cable drive motor.

4. Slip shim spacer (.5 bore) over cable drive motor shaft.

5. Press key (1.25 in length) into cable drive motor shaft.

6. Slip stationary half of clutch over cable drive motor with eyelet slipped over machine screw fixed in frame-1.

7. Tighten clutch set screws onto cable drive motor shaft.

8. Insert motor shaft extension into open side of clutch.

9. Slip plastic bushing from clutch over shaft extension.

10. Press .125 pin into pulley.

11. Press ball bearing (.5 bore) into pulley.

12. Bolt pulley to unmounted half of clutch with three #8-32x.375 machine screws, but leave loose.

13. Slip unmounted half of clutch over shaft extension.

14. Tighten bolts connecting pulley to clutch while verifying free rotation of the assembly.

15. Slip shim spacer (.5 bore) over cable drive motor shaft extension.

16. Slip clutch spacer over cable drive motor shaft extension.

17. Slip shim spacer (.5 bore) over cable drive motor shaft extension.

18. Slip shim spacers (.625 bore) over either end of thigh shaft.

19. Loop timing belt over large timing belt pulley.

20. Place leg assembly in bearing of frame-1.

21. Bolt frame-2 to frame-1 with two #10-24x.75 machine screws.

22. Press two ball bearings (one .625 bore and one .5 bore) into frame-3.

23. Bolt frame-3 to frame-2 with two #10-24x.75 machine screws.

24. Bolt frame-4 to frame-5 with two #10-24x.75 machine screws.

25. Bolt frame-6 to frame-5 with two #10-24x.75 machine screws.

26. Press ball bearing (.5 bore) into frame-5.

27. Bolt Hathaway Emoteq 3003 motor to frame-5 with four #10-32x.5 machine screws. This is the hip drive motor.

28. Slip shim spacer (.5 bore) over hip drive motor shaft.

29. Press key (.9 in length) into hip drive motor shaft.

30. Slip small timing belt pulley over hip drive motor shaft.

31. Slip shim spacer (.5 bore) over hip drive motor shaft.

32. Loop timing belt over small timing belt pulley.

33. Bolt frame-6 to frame1 with two #10-24x.75 machine screws.

34. Bolt frame-3 to frame-4 with two #10-24x.75 machine screws.

35. Press ball bearing (.75 bore) onto sleeve.

36. Place retaining ring (.75 bore) on sleeve.

37. Slide sleeve into place between frame-1 and frame-5, bolt with 1/4-20x2.5 machine screw, two 1/4 washers, and one 1/4-20 nut. Adjustment can be made here to achieve the desired timing belt tension.

38. Bolt electronics mounting plate to frame-1, frame-2, and frame-3 with three #10-24x.5 machine screws.

39. Slip cable under pin in pulley. Tie terminal knot in cable and secure in pulley groove.

40. Swing leg as far back as possible and tie cable to eye bolt to achieve as tight a connection as possible. (When leg swings forward, cable with tighten more.) It seems to work well to loop the cable around the bottom of the eye bolt, loop the cable back around itself and underneath the eye bolt again in the opposite direction, loop the cable back one more time around itself, thread the cable through the eye bolt, and tie a knot that will not slip through the eye. A plastic insert in the eye bolt can reduce the size of the required knot.

B.6 Boom Assembly

B.6.1 Parts List

Frame assembly

8 Bearings, .3125 bore, extended inner race, McMaster Carr part #57155K71 (bear3125bore.prt)

3 Small Boom Shafts, steel (boomshaft.prt)

1 Small Boom Shaft with Extension (for encoder mount), steel (boomshaft3.prt)

1 Large Boom shaft with Extension (for encoder mount), steel (boomshaft2.prt)

1 Optical Encoder, .25 hollow shaft bore, 1000 line, McMaster Carr part #6207K13, Accu-Coder 755A (encoder.prt)

1 Optical Encoder, .375 hollow shaft bore, 1000 line, McMaster Carr part #6207K14, Accu-Coder 755A (encoder.prt)

2 Leg Boom Brackets, aluminum (parallel5.prt)

2 Wall Boom Brackets, aluminum (parallel6.prt)

1 Pillowblock, .625 bore, Fafnir part #RAK5/8 (pillowblock.prt)

1 Pillowblock-like Cap, aluminum (pillowcap.prt)

2 Rectangular Aluminum Tubes, 1.5 x .75 x 8 feet, .125 wall (squaretube.prt)

2 Round Tubes, 1.0 OD, ground supports size and shape could be anything (vertube.prt)

1 Wall Plate, .25 thick aluminum (wallplate.prt)

1 Ball bearing, .625 bore, NTN part #R10ZZC3/5C (bear625bore.prt)

2 Machine Screws 3/8-16x1.0

2 Machine Screws #12-24x1.0

2 Machine Screws #10-24x1.75

2 Machine Screws #10-24x1.25

4 Machine Screws #4-40x.25

6 Machine Screws 1/4-20x.875

2 Nuts, 3/8-16

2 Nuts, #12-24

4 Nuts, #10-24

2 Nuts, 1/4-20

B.6.2 Assembly Instructions

1. Bolt pillowblock to wall plate with two 3/8-16x1.0 machine screws and two 3/8-16 nuts.

2. Place large boom shaft with extension in pillowblock such that extension is at the free end.

3. Slip pillowblock-like cap over large boom shaft such that the tapped holes for the encoder mount face the outside.

4. Bolt the pillowblock-like cap to the wall plate with two #12-24x1.0 machine screws and two #12-24 nuts.

5. Press four bearings (.3125 bore) into the two wall boom brackets.

6. Press one wall boom bracket around large boom shaft.

7. Press small boom shaft with extension into bearing in bore of wall boom bracket that

has tapped holes for encoder mount around it.

8. Press small boom shaft into other bearing in same wall boom bracket.

9. Slip two rectangular aluminum tubes over the assembled small boom shafts.

10. Press other wall boom bracket around large boom shaft such that two small boom shafts are pressed into the bores in the wall boom bracket and the rectangular aluminum tubes are captured between the brackets.

11. Bolt two wall boom brackets together with two #10-24x1.75 machine screws, two #10-24x1.25 machine screws, and four #10-24 nuts.

12. Slip encoder with .25 bore over extension of small boom shaft with extension and bolt to the wall boom bracket with two #4-40x.25 machine screws.

13. Slip encoder with .375 bore over extension of large boom shaft and bolt to pillowblock-like cap with two #4-40x.25 machine screws.

14. Press four bearings (.3125 bore) into the two leg boom brackets.

15. Bolt one leg boom brackets to frame-1 of frame assembly with three 1/4-20x.875 machine screws and three 1/4-20 nuts.

16. Press two small boom shafts into two bearings in the leg boom bracket bolted to frame assembly.

17. Slip the two assembled small boom shafts through the two rectangular aluminum tubes such that the leg boom bracket is nearly flush with the rectangular aluminum tubes.

18. Press the other leg boom bracket onto the two assembled small boom shafts such that the shafts are pressed into the bearings and the rectangular aluminum tubes are captured between the brackets.

19. Bolt the free leg boom bracket to frame-1 of frame assembly with three 1/4-20x.875 machine screws and three 1/4-20 nuts.

B.7 Treadmill Assembly

B.7.1 Parts List

1 Treadmill, Jog-A-Dog D.C. #6 with 1.0 H.P. motor, speed adjustment to 12mph

1 Tachometer Adapter Kit, Lesson part #175193

1 Tachometer, Baldor 5PY Series part #PTG1024LD

B.7.2 Assembly Instructions

1. Bolt tachometer to tachometer adapter.

2. Separate plastic universal joint.

3. Connect one half of universal joint to tachometer shaft with set screws.

4. Connect other half of universal joint to motor shaft with set screws.

5. Assemble tachometer adapter to back of motor such that the plastic universal joint presses back together.

6. Bolt tachometer adapter to motor.

APPENDIX C

MONOPOD WITH MOTOR MODEL

Figure C.1 is a schematic of the simplified monopod model used to evaluate how back-driving the knee actuation motor would affect the motion of the prototype articulated leg. The monopod consists of a rigid body of mass m and a massless leg with a compression spring of stiffness k. Within the body, a brushless DC servomotor drives a pulley of radius r around which is wrapped the cable connected to the foot. This drive system compresses

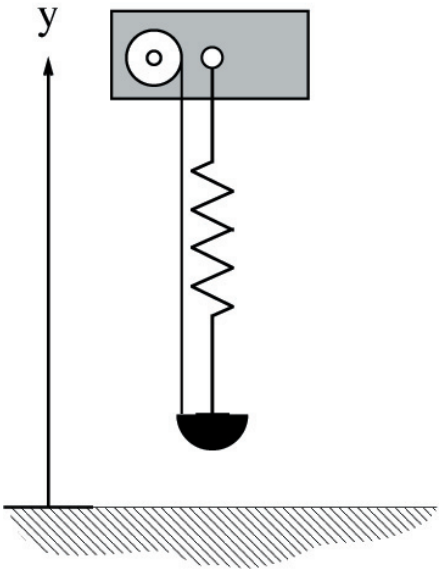

Figure C.1: Simplified monopod with cable drive system.

the leg spring during flight to store elastic energy, some of which is then recovered during stance. The model was designed to determine how much the energy lost in backdriving the motor reduces the hopping height.

The motion of the body is limited to translation in the vertical direction, and the position of the shoulder/hip joint relative to the ground is y. The length of the leg when the cable drive has compressed the spring is L_c, and the free length of the leg is L_o. There are four different cases governing the monopod's motion. When $y \geq L_c$ and $\dot{y} < 0$, the leg has been compressed, but the foot has not yet contacted the ground. Therefore, the body falls with the acceleration of gravity, g,

$$\ddot{y} = -g. \tag{C.1}$$

When $y < L_c$, the foot is on the ground, and spring is compressed more so than during flight.

$$\ddot{y} = \frac{k}{m}(L_o - y) - g. \tag{C.2}$$

Equation C.2 reflects the fact that the cable goes slack during stance, so the full spring force acts on the body.

When $y \geq L_c$ and $\dot{y} > 0$, the cable is no longer slack, and the foot may or may not be in contact with the ground. If it is on the ground, then,

$$\ddot{y} = \frac{k}{m}(L_o - y) - g - \frac{F_c}{m}, \tag{C.3}$$

where F_c is the cable force. The cable force is a function of the motor dynamics, and the body's motion is affected accordingly. For this simplified analysis, the motor position is assumed constant during stance until the cable goes taunt, at which time the motor voltage is reversed to help release the cable. Under ideal conditions, the cable voltage would be

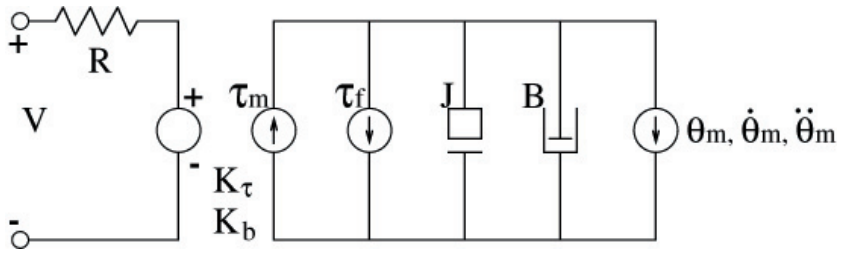

Figure C.2: Motor model for cable drive system.

reversed immediately upon foot touchdown in order unwrap as much of the cable from the pulley as possible.

The motor model for the cable drive system is shown in Figure C.2, and all of the parameters in the model are listed in Table C.1. With the cable taunt, the motor equation is,

$$F_c r + \tau_m = J\ddot{\theta}_m + B\dot{\theta}_m + \tau_f. \tag{C.4}$$

Substituting with the following equation for τ_m,

$$\tau_m = \frac{K_\tau V}{R} - \frac{K_b K_\tau}{R}\dot{\theta}_m, \tag{C.5}$$

and solving for F_c,

$$F_c = \frac{J}{r}\ddot{\theta}_m + \frac{B + \frac{K_b K_\tau}{R}}{r}\dot{\theta}_m + \frac{\tau_f}{r} - \frac{K_\tau V}{rR}. \tag{C.6}$$

With the foot on the ground, the angular velocity and acceleration of the motor are related to the body's velocity and acceleration as follows: $\dot{\theta}_m = \frac{\dot{y}}{r}$ and $\ddot{\theta}_m = \frac{\ddot{y}}{r}$. Making these substitutions,

$$F_c = \frac{J}{r^2}\ddot{y} + \frac{B + \frac{K_b K_\tau}{R}}{r^2}\dot{y} + \frac{\tau_f}{r} - \frac{K_\tau V}{rR}. \tag{C.7}$$

Equation C.3 can then be written,

$$\ddot{y} = \left(-\frac{B + \frac{K_b K_\tau}{R}}{mr^2 + J}\right)\dot{y} + \left(-\frac{kr^2}{mr^2 + J}\right)y + \frac{kL_o r^2 - r\tau_f - r^2 mg + \frac{rK_\tau V}{R}}{mr^2 + J}, \tag{C.8}$$

Parameter	Description	Value	Units
y	body position	varies	m
L_c	compressed leg length	.485	m
L_o	free leg length	.55	m
g	gravity	9.81	$\frac{m}{s^2}$
k	spring constant	16.0	$\frac{kN}{m}$
m	body mass	17	kg
r	pulley radius	.013	m
θ_m	motor angular position	varies	rad
B	viscous damping coefficient	1.05e-3	$\frac{Nm}{rad/s}$
K_b	back EMF constant	.21	$\frac{V}{rad/s}$
K_τ	torque sensitivity	.21	$\frac{Nm}{Amp}$
R	resistance	1.57	Ω
J	motor inertia	3.9e-5	$kg \cdot m^2$
τ_f	static friction torque	.12	$N \cdot m$

Table C.1: Parameters of the monopod model.

which is valid when $y \geq L_c$ and $\dot{y} > 0$, if the foot is on the ground and F_c is positive. A negative value for F_c would indicate that the motor was turning fast enough to produce slack in the cable, and Equation C.2 would apply.

The foot leaves the ground when the cable force is equal to the spring force or, if the cable force has gone to zero, when $y > L_f$. In this case, only the acceleration of gravity acts on the body, so Equation C.1 again applies.

A dynamic simulation using Matlab Simulink was developed to compute the monopod's motion through the four cases represented by Equations C.1, C.2, and C.8. The simulation used fourth order Runge-Kutta integration with a fixed time step of 0.00001 s. The motor parameters listed in Table C.1 correspond to those of a Hathaway Emoteq HT2503 motor with the viscous damping coefficient and static friction torque values increased to account

for the effects of a 3:1 gear reduction. This is not the same motor found in the prototype leg. It was chosen for this model because it has a higher peak torque, and thus, requires a smaller gear reduction to meet the design specification. The gear reduction was minimized in an effort to minimize the energy lost in backdriving the motor.

Figure C.3 plots the motion of the monopod for slightly more than one hopping cycle. The plot with the higher peak is the trajectory followed without the motor model included, so it represents the zero loss case. The other plot is the trajectory for the full model. Both of the plots show the monopod rise above the .9 m height from which it was initially dropped because the leg spring energy has been injected into the system. The two plots also coincide up to the point where the cable becomes taunt because the presence of the

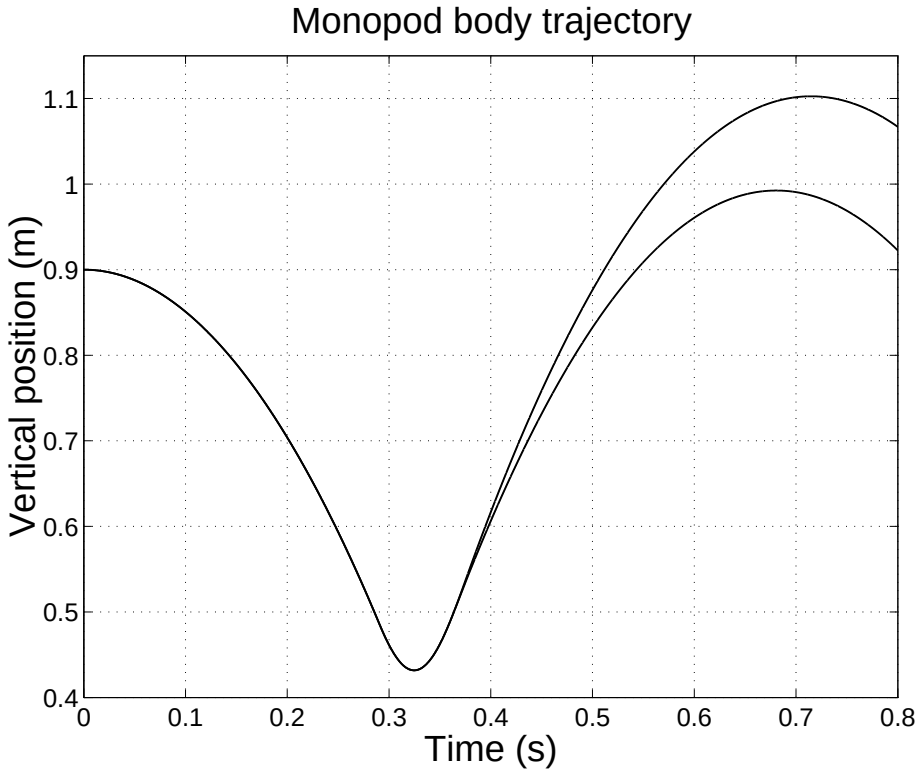

Figure C.3: Trajectory of the monopod's body with and without the motor model.

motor has no impact beforehand. The energy loss from backdriving the motor is clearly seen in the lower height achieved by the full model. The increase in height from the initial hop is actually reduced by more than 50 % in the full model compared to the lossless case. A corresponding effect is that the hopping frequency of the full model is higher.

The relatively large reduction in hopping height observed in Figure C.3 for this simple model prompted the use of a clutch to decouple the motor from the cable drive during the stance phase. The simulation was run for initial drop heights of .8, .7, and .6 m as well, and the corresponding percentage reductions were 44 %, 33 %, and 20 %. The motor has a less significant effect on the hopping height for lower drop heights because the foot remains in contact with the ground for a shorter period of time. These losses are still unacceptably large, and a drop of .6 m is unreasonably low for consistent hopping of the monopod model.

BIBLIOGRAPHY

[1] S. K. Agrawal and K. J. Waldron. Impulsive model for a quadruped running machine. In *Proceedings of the Winter Annual Meeting of the ASME*, volume 11, pages 139–148, New York, 1989. ASME.

[2] M. Ahmadi and M. Buehler. Preliminary experiments with an actively tuned passive dynamic running robot. In *Proceedings of the International Symposium on Experimental Robotics*, pages 249–260, Barcelona, 1997.

[3] R. M. Alexander. Mechanics and scaling of terrestrial locomotion. In T. J. Pedley, editor, *Scale Effects in Animal Locomotion*, chapter 6, pages 93–110. Academic Press, London, 1977.

[4] R. M. Alexander. *Elastic Mechanisms in Animal Movement*. Cambridge University Press, Cambridge, 1988.

[5] R. M. Alexander. Why mammals gallop. *American Zoologist*, 28:237–245, 1988.

[6] R. M. Alexander. Optimization and gaits in the locomotion of vertebrates. *Physiological Reviews*, 69:1199–1227, 1989.

[7] R. M. Alexander. Three uses for springs in legged locomotion. *International Journal of Robotics Research*, 9:53–61, 1990.

[8] R. M. Alexander. A model of bipedal locomotion on compliant legs. *Philosophical Transactions of the Royal Society of London, B*, 338:189–198, 1992.

[9] R. M. Alexander, N. J. Dimery, and R. F. Ker. Elastic structures in the back and their roll in galloping in some mammals. *Journal of Zoology, London*, 207:467–482, 1985.

[10] R. M. Alexander and A. S. Jayes. A dynamic similarity hypothesis for the gaits of quadrupedal mammals. *Journal of Zoology, London*, 201:135–152, 1983.

[11] R. M. Alexander, A. S. Jayes, and R. F. Ker. Estimates of energy cost for quadrupedal running gaits. *Journal of Zoology, London*, 190:155–192, 1980.

[12] R. M. Alexander and A. Vernon. The mechanics of hopping by kangaroos. *Journal of Zoology, London*, 177:265–303, 1975.

[13] H. Asada. A geometrical representation of manipulator dynamics and its application to arm design. *ASME Journal of Dynamic Systems, Measurement, and Control*, 105:751–756, 1983.

[14] O. R. Barclay. Some aspects of the mechanics of mammalian locomotion. *Journal of Experimental Biology*, 30:116–120, 1953.

[15] J. E. Bares and D. S. Wettergreen. Dante II: Technical description, results, and lessons learned. *International Journal of Robotics Research*, 18(7):621–649, 1999.

[16] M. Berkemeier. Modeling the dynamics of quadrupedal running. *International Journal of Robotics Research*, 17(9):971–985, 1998.

[17] A. A. Biewener and C. R. Taylor. Bone strain: A determinant of gait and speed? *Journal of Experimental Biology*, 123:383–400, 1986.

[18] R. Blickhan. The spring-mass model for running and hopping. *Journal of Biomechanics*, 22:1217–1227, 1989.

[19] R. Blickhan and R. J. Full. Locomotion energetics of the ghost crab II. Mechanics of the centre of mass during walking and running. *Journal of Experimental Biology*, 130:15–174, 1987.

[20] R. Blickhan and R. J. Full. Similarity in multilegged locomotion: Bouncing like a monopode. *Journal of Comparative Physiology A*, 173:509–517, 1993.

[21] C. M. Brown. *Dog Locomotion and Gait Analysis*. Hoflin Publishing, Wheat Ridge, Colorado, 1986.

[22] H. B. Brown, Jr. and G. Zeglin. The bow leg hopping robot. In *Proceedings of the IEEE International Conference on Robotics and Automation*, pages 781–786, Piscataway, New Jersey, 1998. IEEE.

[23] J. D. Bryant, M. B. Bennett, J. Brust, and R. M. Alexander. Forces exerted on the ground by galloping dogs. *Journal of Zoology, London*, 213:193–203, 1987.

[24] G. A. Cavagna, N. C. Heglund, and C. R. Taylor. Mechanical work in terrestrial locomotion: Two basic mechanisms for minimizing energy expenditure. *American Journal of Physiology*, 233:243–261, 1977.

[25] G. A. Cavagna, F. P. Saibene, and R. Margaria. External work in walking. *Journal of Applied Physiology*, 18:1–9, 1963.

[26] G. A. Cavagna, F. P. Saibene, and R. Margaria. Mechanical work in running. *Journal of Applied Physiology*, 19:249–256, 1964.

[27] G. A. Cavagna, H. Thys, and A. Zamboni. The sources of external work in level walking and running. *Journal of Physiology*, 262:639–657, 1976.

[28] P. M. D. L. Croix. The evolution of locomotion in mammals. *Journal of Mammalogy*, 17:51–54, 1936.

[29] A. I. Dagg. The locomotion of the camel (Camelus dromedarius). *Journal of Zoology, London*, 174:67–78, 1974.

[30] A. I. Dagg and A. De Vos. Fast gaits of pecoran species. *Journal of Zoology, London*, 155:499–506, 1968.

[31] H. DeMan, D. Lefeber, and J. Vermeulen. Design and control of a one-legged robot hopping on irregular terrain. In *Proceedings of the Euromech Colloquium 375 (Biology and Technology of Walking)*, pages 173–180, Munich, 1998.

[32] H. DeMan, D. Lefeber, and J. Vermeulen. Design and control of a robot with one articulated leg for locomotion on irregular terrain. In *Proceedings of the Twelfth CISM-IFToMM Symposium on Theory and Practice of Robots and Manipulators*, pages 417–424, Vienna, 1998. Springer Verlag.

[33] H. Elftman. Forces and energy changes in the leg during walking. *Journal of Physiology*, 125:339–356, 1939.

[34] C. T. Farley, J. Glasheen, and T. A. McMahon. Running springs: Speed and animal size. *Journal of Experimental Biology*, 185:71–86, 1993.

[35] C. T. Farley and C. R. Taylor. A mechanical trigger for the trot-gallop transition in horses. *Science*, 253:306–308, 1991.

[36] M. A. Fedak, N. C. Heglund, and C. R. Taylor. Energetics and mechanics of terrestrial locomotion II. Kinetic energy changes of the limbs and body as a function of speed and body size in birds and mammals. *Journal of Experimental Biology*, 79:23–40, 1982.

[37] W. O. Fenn. Work against gravity and work due to velocity changes in running. *American Journal of Physiology*, 93:433–462, 1930.

[38] A. A. Frank. Automatic control systems for legged locomotion. Technical Report USCEE Report No. 273, University of Southern California, Los Angeles, 1968.

[39] P. S. Freeman and D. E. Orin. Efficient dynamic simulation of a quadruped using a decoupled tree-structure approach. *International Journal of Robotics Research*, 6:619–627, 1991.

[40] M. J. French. *Invention and evolution: Design in nature and engineering*. Cambridge University Press, Cambridge, 1988.

[41] R. J. Full, R. Blickhan, and L. H. Ting. Leg design in hexapedal runners. *Journal of Experimental Biology*, 158:369–390, 1991.

[42] R. J. Full and M. A. R. Koehl. Drag and lift on running insects. *Journal of Experimental Biology*, 176:89–101, 1993.

[43] R. J. Full and M. S. Tu. Mechanics of six-legged runners. *Journal of Experimental Biology*, 148:129–146, 1990.

[44] R. J. Full and M. S. Tu. Mechanics of a rapid running insect: Two-, four- and six-legged locomotion. *Journal of Experimental Biology*, 156:215–231, 1991.

[45] J. Furusho, S. Akihito, S. Masamichi, and K. Eichi. Realization of bounce gait in a quadruped robot with articular-joint-type-legs. In *Proceedings of the IEEE International Conference on Robotics and Automation*, pages 697–702, Piscataway, New Jersey, 1995. IEEE.

[46] P. P. Gambaryan. *How Mammals Run: Anatomical Adaptations*. John Wiley & Sons, New York, 1974.

[47] T. I. Grand. Body weight: Its relation to tissue composition, segment distribution, and motor function. *American Journal of Physical Anthropology*, 47:211–240, 1977.

[48] A. R. Gravagne and I. D. Walker. Towards impulsive manipulation: A general algebraic collision model for spatial robots. In *Proceedings of the IEEE International Conference on Robotics and Automation*, pages 1707–1713, Piscataway, New Jersey, 2000. IEEE.

[49] J. Gray. *Animal Locomotion*. W.W. Norton & Company, Inc., New York, 1968.

[50] P. Gregorio, M. Ahmadi, and M. Buehler. Design, control, and energetics of an electrically actuated legged robot. *IEEE Transactions on Robotics and Automation*, 13:96–104, 1997.

[51] N. C. Heglund, M. A. Fedak, C. R. Taylor, and G. A. Cavagna. Energetics and mechanics of terrestrial locomotion IV. Total work and efficiency as a function of speed and body size in birds and mammals. *Journal of Experimental Biology*, 97:57–66, 1982.

[52] N. C. Heglund and C. R. Taylor. Speed, stride frequency and energy cost per stride: How do they change with body size and gait? *Journal of Experimental Biology*, 138:301–318, 1988.

[53] N. C. Heglund, C. R. Taylor, and T. A. McMahon. Scaling stride frequency and gait to animal size: Mice to horses. *Science*, 186:1112–1113, 1974.

[54] H. Herr and T. A. McMahon. A trotting horse model. *International Journal of Robotics Research*, 19:566–581, 2000.

[55] H. Herr and T. A. McMahon. A galloping horse model. *International Journal of Robotics Research*, 20:26–37, 2001.

[56] M. Hildebrand. Motions of the running cheetah and horse. *Journal of Mammalogy*, 40:481–495, 1959.

[57] M. Hildebrand. Analysis of tetrapod gaits: General considerations and symmetrical gaits. In R. M. Herman, S. Grillner, P. S. G. Stein, and D. G. Stuart, editors, *Neural control of locomotion*, pages 203–236. Plenum Press, New York, 1976.

[58] M. Hildebrand. The adaptive significance of tetrapod gait selection. *American Zoologist*, 20:97–103, 1977.

[59] M. Hildebrand. Analysis of asymmetrical gaits. *Journal of Mammalogy*, 58:131–156, 1977.

[60] M. Hildebrand. Walking and running. In M. Hildebrand, D. M. Bramble, K. F. Liem, and D. B. Wake, editors, *Functional Vertebrate Morphology*, chapter 3, pages 25–65. Belknap Press, Cambridge, 1985.

[61] A. V. Hill. The air-resistance to a runner. *Proceedings of the Royal Society of London, Section B*, 102:380–385, 1927.

[62] A. V. Hill. The series elastic component of muscle. *Proceedings of the Royal Society of London, Series B*, 137:273–280, 1950.

[63] S. Hirose. A study of design and control of a quadruped walking vehicle. *International Journal of Robotics Research*, 3:113–133, 1984.

[64] S. Hirose and K. Kato. Study on quadruped walking robot in Tokyo Institute of Technology: Past, present, and future. In *Proceedings of the IEEE International Conference on Robotics and Automation*, pages 414–419, Piscataway, New Jersey, 2000. IEEE.

[65] N. Hogan. Impedance control: An approach to manipulation. *Journal of Dynamic Systems, Measurements, and Control*, 107:8–16, 1985.

[66] A. B. Howell. *Speed in Animals*. University of Chicago Press, Chicago, 1944.

[67] D. F. Hoyt and C. R. Taylor. Gait and the energetics of locomotion in horses. *Nature*, 292:239–240, 1981.

[68] A. S. Jayes and R. M. Alexander. Mechanics of locomotion in dogs and sheep. *Journal of Zoology, London*, 185:289–308, 1978.

[69] A. S. Jayes and R. M. Alexander. Estimates of mechanical stresses in leg muscles of galloping greyhounds. *Journal of Zoology, London*, 198:315–328, 1982.

[70] T. Kato, A. Takanishi, H. Jishikawa, and I. Kato. The realization of the quasi-dynamic walking by the biped walking machine. In *Proceedings of the Fourth CISM-IFToMM Symposium on Theory and Practice of Robots and Manipulators*, pages 341–351, Warsaw, 1983. Polish Scientific Publishers.

[71] O. Khatib. A unified approach for motion and force control of robot manipulators: The operational space formulation. *IEEE Journal of Robotics and Automation*, 3(1):43–53, 1987.

[72] O. Khatib. Inertial properties in robotic manipulation: An object-level framework. *International Journal of Robotics Research*, 13(1):19–36, 1995.

[73] H. Kimura, S. Akiyama, and K. Sakurama. Realization of dynamic walking and running of the quadruped using neural oscillator. *Autonomous Robots*, 7:247–258, 1999.

[74] B. W. Lilly, Jr. Design and analysis of a mechanically coordinated, dynamically stable, quadruped trotting machine. Master's thesis, The Ohio State University, 1986.

[75] R. A. Liston and R. S. Mosher. A versatile walking truck. In *Proceedings of the Transportation Engineering Conference*, London, 1968. Institution of Civil Engineers.

[76] J. T. Manter. The dynamics of quadrupedal walking. *Journal of Experimental Biology*, 15:522–540, 1938.

[77] E. J. Marey. *Animal mechanism: A treatise on terrestrial and aerial locomotion*. International Science Series. Appleton, 1879.

[78] R. Margaria and G. A. Cavagna. Human locomotion in subgravity. *Aerospace Medicine*, 35:1140–1146, 1964.

[79] D. W. Marhefka. *Fuzzy Control and Dynamic Simulation of a Quadruped Galloping Machine*. Doctoral dissertation, The Ohio State University, 2000.

[80] K. Matsuoka. A model of repetitive hopping movements in man. In *Proceedings of the Fifth World Congress on Theory of Machines and Mechanisms*. International Federation for Information Processing, 1979.

[81] R. B. McGhee. Finite state control of quadruped locomotion. In *Proceedings of the Second International Symposium on External Control of Human Extremities*, Dubrovnik, Yugoslavia, 1966.

[82] R. B. McGhee. Vehicular legged locomotion. In G. N. Saridis, editor, *Advances in Automation and Robotics*. JAI Press, 1983.

[83] T. A. McMahon. *Muscles, Reflexes, and Locomotion*. Princeton University Press, Princeton, 1984.

[84] T. A. McMahon. The role of compliance in mammalian running gaits. *Journal of Experimental Biology*, 115:263–282, 1985.

[85] T. A. McMahon and G. C. Cheng. The mechanics of running: How does stiffness couple with speed? *Journal of Biomechanics*, 23(Supp. 1):65–78, 1990.

[86] G. Mennitto and M. Buehler. CARL: A compliant articulated robotic leg for dynamic locomotion. *Robotics and Autonomous Systems*, 18:337–344, 1996.

[87] A. E. Minetti. The biomechanics of skipping gaits: A third locomotion paradigm? *Proceedings of the Royal Society of London B*, 265:1227–1235, 1998.

[88] A. E. Minetti, L. Ardigo, E. Reinach, and F. Saibene. The relationship between mechanical work and energy expenditure of locomotion in horses. *Journal of Experimental Biology*, 202:2329–2338, 1999.

[89] H. Miura and I. Shimoyama. Dynamic walk of a biped. *International Journal of Robotics Research*, 3:60–74, 1984.

[90] E. Muybridge. *Animals in Motion*. Dover Publications, Inc., New York, 1957.

[91] P. Nanua and K. J. Waldron. Instability and chaos in quadruped gallop. *Journal of Mechanical Design*, 116:1096–1101, 1994.

[92] P. Nanua and K. J. Waldron. Energy comparison between trot, bound, and gallop using a simple model. *ASME Journal of Biomechanical Engineering*, 117:466–473, 1995.

[93] D. E. Okhotsimski, V. S. Gurfinkel, E. A. Devyanin, and A. K. Platonov. Integrated walking robot development. In J. E. Hayes, D. Michie, and L. J. Mikulich, editors, *Machine Intelligence*, volume 9, 1977.

[94] M. G. Pandy, V. Kumar, N. Berme, and K. J. Waldron. The dynamics of quadrupedal locomotion. *ASME Journal of Biomechanical Engineering*, 110:230–237, August 1988.

[95] D. Papadopoulos and M. Buehler. Stable running in a quadruped robot with compliant legs. In *Proceedings of the IEEE International Conference on Robotics and Automation*, page In press, Piscataway, New Jersey, 2000. IEEE.

[96] K. Pearson. The control of walking. *Scientific American*, 235(6):72–86, 1976.

[97] C. J. Pennycuick. On the running of the gnu (connochaetes taurinus) and other animals. *Journal of Experimental Biology*, 63:775–799, 1975.

[98] A. K. Perry, R. Blickhan, A. A. Biewener, N. C. Heglund, and C. R. Taylor. Preferred speeds in terrestrial vertebrates: Are they equivalent? *Journal of Experimental Biology*, 137:207–219, 1988.

[99] G. A. Pratt and M. M. Williamson. Series elastic actuators. In *Proceedings of the IEEE International Conference on Intelligent Robots and Systems*, pages 399–406, Piscataway, New Jersey, 1995. IEEE.

[100] L. G. C. E. Pugh. The influence of wind resistance in running and walking and the mechanical efficiency of work against horizontal or vertical forces. *Journal of Physiology*, 213:255–276, 1971.

[101] H. Rad, P. Gregorio, and M. Buehler. Design, modeling and control of a hopping robot. In *Proceedings of the IEEE/RSJ Conference on Intelligent Systems and Robots*, pages 1778–1785, Piscataway, New Jersey, 1993. IEEE.

[102] M. Raibert. Trotting, pacing and bounding by a quadruped robot. *Journal of Biomechanics*, 23(Supp. 1):79–98, 1990.

[103] M. H. Raibert. *Legged Robots that Balance*. MIT Press, Cambridge, 1986.

[104] M. H. Raibert. Running with symmetry. *International Journal of Robotics Research*, 5(4):3–19, Winter 1986.

[105] M. H. Raibert, H. B. Brown, M. Chepponis, J. Hodgins, J. Koechling, J. Miller, K. N. Murphy, S. S. Murthy, and A. Stentz. Dynamically stable legged locomotion. Technical Report CMU-LL-4-1985, Carnegie-Mellon University, Pittsburgh, 1985.

[106] M. H. Raibert, M. Chepponis, and H. B. Brown. Running on four legs as though they were one. *IEEE Journal of Robotics and Automation*, RA(2):70–82, June 1986.

[107] C. T. Rubin and L. E. Lanyon. Limb mechanics as a function of speed and gait: A study of functional strains in the radius and tibia of horse and dog. *Journal of Experimental Biology*, 101:187–211, 1982.

[108] M. Russell. Odex 1: The first functionoid. *Robotics Age*, 5:12–18, 1983.

[109] J. P. Schmiedeler. The effect of drag on footfall phasing in quadruped galloping. Master's thesis, The Ohio State University, 1998.

[110] J. P. Schmiedeler, D. W. Marhefka, D. E. Orin, and K. J. Waldron. A study of quadruped gallops. In *NSF Design, Service and Manufacturing Grantees and Research Conference*, Tampa, Florida, 2001.

[111] J. P. Schmiedeler and K. J. Waldron. Design of galloping machines. In *Proceedings of the Twelfth CISM-IFToMM Symposium on Theory and Practice of Robots and Manipulators*, pages 353–360, Vienna, 1998. Springer Verlag.

[112] J. P. Schmiedeler and K. J. Waldron. Mechanical design of a quadrupedal galloping machine. In *Proceedings of the Tenth World Congress on the Theory of Machines and Mechanisms*, pages 1985–1990, Oulu, 1999. Oulu University Press.

[113] J. P. Schmiedeler and K. J. Waldron. The mechanics of quadrupedal galloping and the future of legged vehicles. *International Journal of Robotics Research*, 18:1224–1234, 1999.

[114] J. P. Schmiedeler and K. J. Waldron. Impact analysis as a design tool for the legs of mobile robots. In J. Lenarcic and M. M. Stanisic, editors, *Advances in Robot Kinematics*, pages 129–136, Dortrecht, 2000. Kluwer Academic Publishers.

[115] J. P. Schmiedeler, K. J. Waldron, D. W. Marhefka, and D. E. Orin. Design of compliant articulated limbs for a quadrupedal galloping machine. In *Proceedings of the Sixth Applied Mechanisms and Robotics Conference*, pages 006:1–8, Cincinnati, 1999.

[116] R. A. Siston. The biomechanical analysis of a galloping dog. Technical report, The Ohio State University, 2000.

[117] S. M. Song, V. J. Vohnout, K. J. Waldron, and G. L. Kinzel. Computer-aided design of a leg for an energy efficient walking machine. *Mechanism and Machine Theory*, 19:17–24, 1984.

[118] S. M. Song and K. J. Waldron. *Machines that Walk: The Adaptive Suspension Vehicle*. MIT Press, Cambridge, 1988.

[119] S. M. Song, K. J. Waldron, and G. L. Kinzel. Computer-aided geometric design of legs for a walking vehicle. *Mechanism and Machine Theory*, 20:587–596, 1985.

[120] A. Spiessbach, B. M. Gothard, D. G. Morgenthaler, K. J. Waldron, R. S. Price, J. E. Bares, W. H. Chun, F. L. Garrett, and B. Stout. Final report for Mars Rover Sample Return (MRSR) rover mobility and surface rendezvous studies. Technical report, Martin Marietta Space Systems Company, Denver, 1989.

[121] W. B. Stuart and K. J. Waldron. Field trials of a legged vehicle and their implications for the design of forestry machines. In *Proceedings of the Second IARP Workshop on Robotics in Agriculture and the Food Industry*, pages 239–250, Genoa, 1991.

[122] V. B. Sukhanov. *General System of Symmetrical Locomotion of Terrestrial Vertebrates and Some Features of Movement of Lower Tetrapods*. Amerind Publishing, New Delhi, 1974.

[123] I. E. Sutherland. *A Walking Robot*. The Marcian Chronicles, Inc., Pittsburgh, 1983.

[124] C. R. Taylor. Why change gaits? Recruitment of muscles and muscle fibers as a function of speed and gait. *American Zoologist*, 18:153–161, 1978.

[125] C. R. Taylor. Force development during sustained locomotion: A determinant of gait, speed, and metabolic power. *Journal of Experimental Biology*, 115:253–262, 1985.

[126] C. R. Taylor, A. Shkolnik, R. Dmi'El, D. Baharav, and A. Borut. Running in cheetahs, gazelles, and goats: Energy cost and limb configuration. *American Journal of Physiology*, 227(4):848–850, October 1974.

[127] K. J. Waldron and G. L. Kinzel. The relationship between actuator geometry and mechanical efficiency in robots. In *Proceedings of the Fourth CISM-IFToMM Symposium on Theory and Practice of Robots and Manipulators*, pages 305–316, Warsaw, 1981. Polish Scientific Publishing.

[128] K. J. Waldron and G. L. Kinzel. *Kinematics, Dynamics, and Design of Machinery*. John Wiley & Sons, New York, 1999.

[129] I. D. Walker. Impact configurations and measures for kinematically redundant and multiple armed robot systems. *IEEE Transactions on Robotics and Automation*, 10:670–682, 1994.

[130] C. W. Wampler, A. P. Morgan, and A. J. Sommese. Numerical continuation methods for solving polynomial systems arising in kinematics. *Journal of Mechanical Design*, 112:59–68, March 1990.

[131] H. Wong. *Control of a Quadruped Standing Jump and Running Jump Over Irregular Terrain Obstacles*. Doctoral dissertation, The Ohio State University, 1992.

[132] H. C. Wong and D. E. Orin. Control of a quadruped standing jump over irregular terrain obstacles. *Autonomous Robots*, 1:111–129, 1995.

[133] T. Yoshikawa. Analysis and control of robot manipulators with redundancy. In M. Brady and . Paul, editors, *Robotics Research: The First International Symposium*, pages 735–747. MIT Press, Cambridge, 1983.

[134] T. Yoshikawa. Manipulability of robotic mechanisms. In H. Hanafusa and H. Inoue, editors, *Robotics Research: The Second International Symposium*, pages 439–446. MIT Press, Cambridge, 1984.

[135] T. Yoshikawa. Dynamic manipulability of robotic mechanisms. In *Proceedings of the IEEE International Conference on Robotics and Automation*, pages 1033–1038, Piscataway, New Jersey, 1985. IEEE.

[136] G. Zeglin and B. Brown. Control of a bow leg hopping robot. In *Proceedings of the IEEE International Conference on Robotics and Automation*, pages 793–798, Piscataway, New Jersey, 1998. IEEE.

[137] Y. Zheng and H. Hemami. Mathematical modeling of a robot collision with its environment. *Journal of Robotic Systems*, 2(3):289–307, 1985.